ABSTRACT

Title of Dissertation: VOLUMETRIC SOLAR ABSORBING FLUIDS AND THEIR APPLICATIONS IN TWO-PHASE THERMOSYPHON

Jian Zhou
Doctor of Philosophy, 2024

Dissertation Directed by: Dr. Bao Yang, Professor
Department of Mechanical Engineering

A two-phase thermosyphon is a passive system utilizing gravity to transfer working fluids. The working fluids of a two-phase thermosyphon must undergo vaporization and condensation in the same system. Two-phase thermosyphons can also be used as solar collectors. Traditional solar collectors utilize surface absorbers to convert incident solar radiation into thermal energy, but those systems feature a large temperature difference between the surface absorbers and heat transfer fluids, resulting in a reduction in the overall thermal efficiency. Volumetric solar absorbing fluids serve both as solar absorbers and heat transfer fluids, therefore significantly improving the overall efficiency of solar collectors. Comparing to pure fluids, nanofluids possess both enhanced thermal conductivity and solar absorption capacity as volumetric absorbing fluids. Nanofluids, when serving as volumetric solar absorbing fluids, are so far reported to work only at relatively low temperatures and in a single-phase heat transfer regime due to stability issue. This research investigates the possibility of using nanofluids, especially graphene oxide (GO) nanofluids, as volumetric solar absorbing fluids in two-phase thermosyphons. Despite their reputation as both stable and solar absorptive among nanofluids, graphene oxide nanofluids still deteriorate quickly under boiling-condensation processes (~100 °C). The solar transmittance of the GO nanofluids declines from 38 to 4%, during the first 24 h of testing. Further investigation shows that the stability deterioration is caused by

the thermal reduction of GO nanoparticles, which mainly featured with de-carboxylation and de-hydroxylation. A commercial dye named acid black 52, when dissolved in water, exhibits great broadband solar absorption properties and excellent stability. It remains stable for over 199 days in two-phase thermosyphon, and their transmittance in solar spectral region varies less than 9%. The stability of acid black 52 aqueous solution is further confirmed with the 191-day enhanced radiation test, as it shows less than 5% transmittance change in solar spectral region.

VOLUMETRIC SOLAR ABSORBING FLUIDS AND THEIR APPLICATIONS IN TWO-PHASE THERMOSYPHON

By

Jian Zhou

Dissertation submitted to the Faculty of the Graduate School of the
University of Maryland, College Park, in partial fulfillment
of the requirements for the degree of

Doctor of Philosophy

2024

Advisory Committee:

Dr. Bao Yang (Chair/Advisor)

Dr. Amir Riaz

Dr. Peter B. Sunderland

Dr. Yunho Hwang

Dr. Chunsheng Wang (Dean's Representative)

Foreward

UNIVERSITY OF MARYLAND

2181 Glenn L. Martin Hall
College Park, MD 20742-3035 TEL: 301-405-2410
http://www.enme.umd.edu

04/27/2024

Re: Previously Published Materials Appearing in Thesis or Dissertation

Dean of the Graduate School, Jian Zhou has:

☐ NOT INCLUDED any previously published works within their thesis or dissertation.

☒ INCLUDED one or more previously published works within their thesis or dissertation. This letter certifies that the examining committee for the student has determined that the student made a substantial contribution to the previously published work. The inclusion of the previously published work has the approval of the thesis or dissertation advisor and the Graduate Director.

Sincerely,

Peter Sandborn
Director of Graduate Studies
Department of Mechanical Engineering
University of Maryland

Sincerely,

Bao Yang
Advisor for Jian Zhou

Dedication

To my fiancée Jing and my family.

Acknowledgments

I would like to thank my advisor, Dr. Bao Yang, for his full support, guidance, and help during my study at the University of Maryland. I would like to thank Advanced Cooling Technologies, Inc for the help with the long-term two-phase thermosyphon test and enhanced radiation test. I also like to thank Dr. Peter B. Sunderland, Dr. Amir Riaz, Dr. Yunho Hwang, and Dr. Chunsheng Wang for serving as committee members for my dissertation.

I would like to thank Dr. Chaolun Zheng, Mr. Ziyang Sheng, and Mr. Yong Pei for their support, valuable discussions, and suggestions on my research.

This research is financially supported by the Department of Energy, under grant number DE EE0008398.

Table of Contents

List of Tables

List of Figures

Nomenclature

Acronyms and Abbreviations

ΔG	Gibbs free energy
ACT	Advanced Cooling Technologies, Inc.
AM1.5	Air mass of 1.5
ASTM	American Society for Testing and Materials
ATR	Attenuated total reflectance
CB	Conduction band
CHF	Critical heat flux
CI	Cooling water
CNF	Cellulose nanofiber
CNT	Carbon nanotube
CTAB	Cetyltrimethyl ammonium bromide
DVLO	Theory of Derjaguin, Verway, Landau, and Overbeek
DW	Deionized water
FT-IR	Fourier-transform infrared spectroscopy
GO	Graphene oxide
HLB	Hydrophilic/lipophilic balance
EESI	Environmental and Energy Study Institute
EG	Ethylene glycol
EPA	Environmental Protection Agency
FPSC	Flat-plate solar collectors
NASA	National Aeronautics and Space Administration
NIST	National Institute of Standard and Technology
NOx	Nitric oxide and nitrogen dioxide
PT	Pressure transducer
PVP	Polyvinylpyrrolidone
rGO	Reduced graphene oxide
SEM	Scanning electron microscopy
TC	Thermalcouples

TEM	Transmission electron microscopy
UV-Vis	Ultraviolet–visible spectroscopy
XPS	X-ray photoelectron spectroscopy
VB	Valence band

Charpter 1. Introduction

1.1 Solar Thermal Energy

According to the Environmental and Energy Study Institute (EESI), around 80% of total energy demand is fulfilled through fossil fuels nowadays. Including coal, oil, and natural gas, fossil fuels have provided most of our energy for the last 150 years. At current consumption rates, it is estimated that the world's oil reserves could meet demand for around 50 years [1]. Aside from energy depletion, another main concern is environmental pollution caused by the burning of fossil fuels. SO_2 and NO_x produced by the combustion of fossil fuels are considered the main pollutants that lead to smog and acid rain. The burning of fossil fuels also releases large amounts of CO_2, a greenhouse gas, into the air. According to the Environmental Protection Agency (EPA), 65% of CO_2 emissions are caused by the burning of fossil fuels and other industrial processes. Greenhouse gases like CO_2 can trap heat in the earth's atmosphere, eventually leading to global warming, and CO_2 emissions have reportedly increased by more than 10 times since 1900 [2]. At the same time, Colonbo et al. [3] have also reported that the average global temperature has increased by around 0.6°C over the past century. The consequences of global temperature increase now include water scarcity, rising sea levels, flooding, and intense drought, among others. The widespread use of fossil fuels also depletes the ozone layer. It has been reported that the size of the ozone hole over Antarctica increased from 3 million km^2 to 25 million km^2 in just 5 years since 1993 [4], roughly three times the size of Brazil. Ozone in the upper atmosphere can absorb ultraviolet radiation, another type of energy harmful to humans and animals. Ozone layer depletion occurs when volatile

organic compounds and NO_x are released into the atmosphere. Such pollutants are produced whenever fossil fuels are burned.

To meet increasing energy demands, advance society, and ease the environmental challenge posed by fossil fuel consumption, scientists and engineers are focusing on developing renewable energy for the growing needs of humanity. Among all the renewable energy resources, solar thermal energy is considered the most abundant. According to the National Aeronautics and Space Administration (NASA), around 342 watts of solar energy fall upon every square meter of earth averaged per year. This is around 44 quadrillion watts of power. As a comparison, the world's electricity consumption will be around 25 quadrillion watt-hours in 2022. That means around 30 minutes of solar radiation falling on earth is equal to the world's electricity consumption for one year. Solar thermal energy is also considered a clean energy resource, since it poses an extremely low environmental threat [5]. The biggest advantage of solar thermal energy is that it significantly reduces the production of greenhouse gases and pollution.

1.2 Solar Thermal Collectors

Solar thermal collectors are highly practical and effective for harvesting solar thermal energy, and their applications have drawn much attention recently due to the increase in efficiency [6]. Traditional solar thermal collectors usually rely on solar surface absorbers to absorb solar energy and convert it into thermal energy. As shown in Figure 1-1(a), solar energy is first converted into thermal energy by solar selective absorbers, and then the converted energy is transferred through a solid surface via conduction and convection to the working fluid. During the process of energy transfer, a large temperature difference between absorbers and heat transfer fluids manifests,

and much heat is lost to the environment by convection and radiation. This loss reduces overall thermal efficiency [7], [8].

To minimize heat loss to the environment, solar thermal collectors based on volumetric-absorbing fluids have drawn much attention recently. As shown in Figure 1-1(b), volumetric-absorbing fluids can directly convert solar radiation into thermal energy inside the working fluids. Therefore, the temperature of each component inside a volumetric solar thermal collector is lower than that of a surface-based solar thermal collector. Due to the relative low temperature of bulk fluid, heat loss to the environment is also reduced when compared with surface solar absorbers. Figure 1-2 further compares the heat transfer process of a surface-based solar thermal collector and a volumetric-based thermal solar collector in terms of their thermal resistance. According to this model, a volumetric solar system should provide less thermal resistance in converting solar energy into useful thermal energy. It has also been reported that a 5–10% increase in photo-thermal efficiency can be achieved in solar thermal collectors using volumetric absorbing fluids [9], [10], [11], [12].

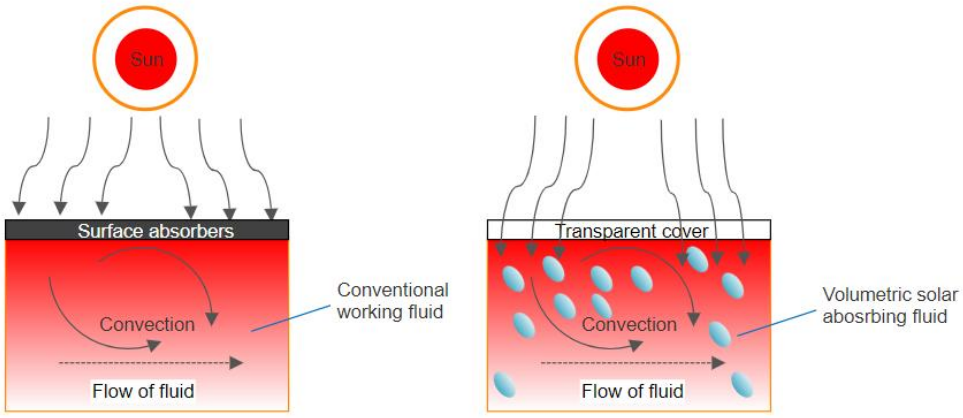

Figure 1-1. Illustration of solar collectors using (a) Surface absorbers and (b) Volumetric absorbers.

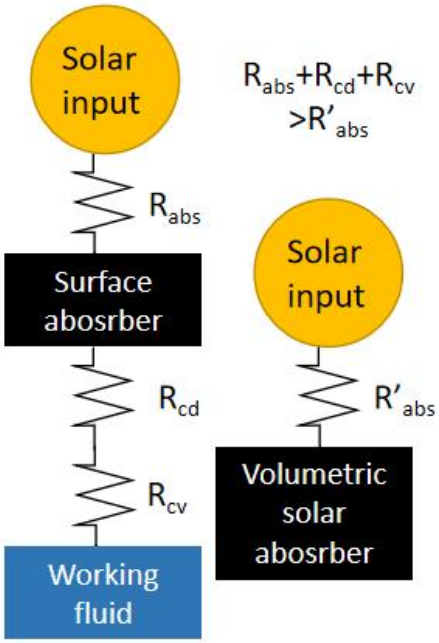

Figure 1-2. Thermal Resistance Comparison Between a Conventional Solar Thermal Collector and a Volumetric Solar Collector. R_{abs}, R_{cd}, Rcv, and R'_{abs} stand for the thermal resistance of solid surface absorption, conduction, convection, and volumetric solar absorption heat transfer steps.

1.3 Nanofluids

Nanofluids are dispersions of nanoparticles in the base fluid. The most commonly used nanoparticles are Cu, Fe, Al, Au, CuO, Fe_2O_3, Al_2O_3, SiO_2, and carbon-related materials. Base fluids are usually water, ethylene glycol, and thermal oils. Nanofluids are prepared by choosing different combinations between nanoparticles and base fluids. Compared to pure base fluids, nanofluids usually present enhanced thermal properties, especially thermal conductivity. The enhanced thermal conductivity is considered the most important advantage of nanofluids. However, nanofluids also present a higher viscosity than that of the respective base fluid. The higher viscosity of nanofluids may lead to higher pumping work demand, further limiting the concentration of prepared nanofluids in their applications. Another

concern with using nanofluids is stability. The performance of nanofluids in various applications highly depends strongly on their own stability. Due to the existence of the Van der Waals attractive force and gravitational force, nanoparticles present in the prepared suspension tend to collide with each other and form clusters. Particle agglomeration will then lead to large cluster formation and sedimentation, eventually deteriorating the stability of nonfluids. Particle agglomeration and sedimentation may also create problems such as microchannel clogging, low zthermal conductivity, corrosion, increased pump costs, and so on. In addition, prepared nanofluids' stability depends on operating conditions such as concentration, working temperature, solar radiation intensity, and so forth. Therefore, comprehensive nanofluids research is necessary to understand their stability.

Nanofluids have been variously applied due to their unique characteristics. Due to the above-noted advantages, nanofluids are widely used in several fields, including cooling and heat dissipation, solar collection, energy storage, oil recovery, and so on [13], [14], [15], [16]. Despite numerous studies on nanofluid properties, most are limited by certain operating parameters, possibly limited to given conditions.

1.4 Two-Phase Thermosyphon

Two-phase thermosyphon refers to a simple and efficient wickless heat pipe in which the condensed liquid moves to the condenser by gravity [17]. A typical two-phase thermosyphon system is shown in Figure 1-3. Different from traditional heat pipes, a two-phase thermosyphon lacks the large flow resistance inside the wick, as the condensate liquid in the system returns to the heated side under the effect of gravity instead of capillary forces in wicked heat pipes [18]. Therefore, a two-phase thermosyphon can be used in much wider temperature ranges than a wicked heat pipe.

During operation, the working fluid is heated and evaporates in the evaporator. Then the vapor travels through the adiabatic section to the condenser. In the condenser, the vapor releases heat and turns back into liquid [19]. Two-phase thermosyphons are widely used in varied applications, from small-scale to large-scale systems. Such technology is used in chemical applications [20], energy storage systems [21], power generators [22], and so forth. It also draws much attention to the area of solar energy systems like solar collectors [23]. The two-phase thermosyphon is also commonly found in solar water heating systems. However, most systems reported are based on traditional solar collectors, which rely on surface absorbers to absorb and convert solar energy into thermal energy. Few papers have discussed the combination of a volumetric solar thermal collector with a two-phase thermosyphon.

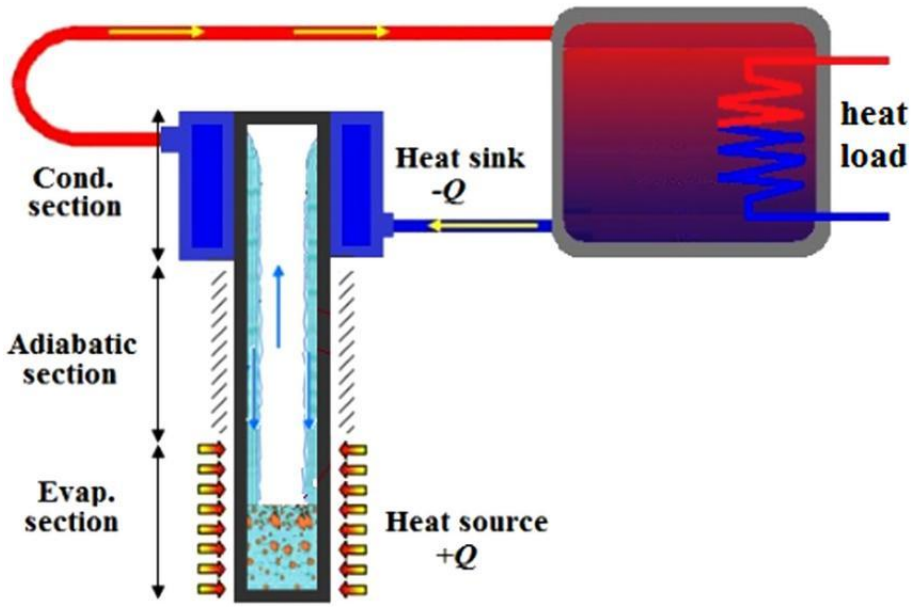

Figure 1-3. Schematic of a typical two-phase thermosyphon system [17].

1.5 Motivations

Recent years have seen increasing interest in renewable energy for several reasons, and being environmentally sustainable is among the most important. As

societal systems shift away from fossil fuels to zero-carbon sources, the world is nearing a renewable-energy future.

1.5.1 Motivation to Improve the Performance of the Solar Collector

Volumetric absorbing fluid present huge potential by significantly decreasing overall thermal resistance between solar radiation and working fluid. However, traditional solar collectors, for example, flat-plate solar collectors, remain the most common solar water system available on the market. The two-phase thermosyphon also appears in solar collectors, but most system performance studies focus on operational parameters such as inclination angle, geometry, filling ratio, working temperature, and tube length. Few papers have discussed the possibility of enhancing system performance by combining a two-phase thermosyphon with a volumetric solar collector. A similar performance study on operational parameters can also be developed based on the new combined system to further increase system efficiency.

1.5.2 Motivation on nanofluids

Nanofluids have drawn much attention recently due to their superior thermal-physical properties over base fluids. They are widely used in thermal applications for heat transfer enhancement, and their performance is significantly influenced by their stability. Nanofluids are also reportedly used as volumetric solar absorbing fluid in solar systems due to their superior optical properties, and many papers have discussed the stability of different types of nanofluids. However, most of the relevant studies have investigated system performance based on only a few cycles. The deterioration of nanofluid stability caused by particle agglomeration can occur even if the nanofluid remains quite stable for a few cycles, and system performance can be heavily influenced over long-term operation. Other papers have discussed nanofluid stability

in long-term storage. However, particle collision and agglomeration are significantly influenced by Brownian motion, which is driven by temperature. Therefore, room-temperature storage may pose much less threat to the stability of nanofluids than thermal cycles.

Nanofluid stability is also reported to be enhanced by multiple methods: for example, pH control, ultrasonication, the use of surfactant, and surface modification. Numerous studies have been carried out in the field of nanofluids. However, the myriad nanofluid types and the variety of applications and operating conditions proposed in the literature complicate the definition of criteria using the available experimental data. Therefore, a systematic stability study, such as this work undertakes, is necessary to draw further conclusions.

1.6 Summary

Overall, the research aims to develop volumetric solar absorbing fluids applicable in a two-phase thermosyphon solar collector. This objective will be approached step by step. Chapter 2 presents a comprehensive literature review identifying candidate fluids with both high optical to thermal efficiency and resistance to deterioration. Chapter 3 presents experimental methods in this work. Chapter 4 investigates the potential of GO nanofluids as volumetric solar absorbing fluids, and possible degradation mechanism of GO nanofluids at low temperature is also discussed in this chapter. Chapter 5 explores possible methods that can be used to enhance the stability of GO nanofluids. Chapter 6 investigates other fluids as volumetric solar absorbing fluids. Chapter 7 introduces aqueous dye solution as volumetric solar absorbing fluids. Chapter 8 investigates the performance of aqueous dye solution in two-phase thermosyphon over long-term operation. Chapter 9

investigates the stability and possible UV degradation of acid black 52 aqueous solution over long-term operation.

Charpter 2. Literature Review

2.1 Introduction

This chapter mainly focus on volumetric solar absorbing fluids that are reporters by other researchers and their use in different solar applications. Strategies reported to enhance fluids stability are also reviewed in this chapter. Aqueous dye solutions as possible working fluids are also introduced. Mechanism and applications of two-phase thermosyphons are also covered in this chapter.

2.2 Surface Solar Absorber

Traditional solar collectors use a surface solar absorber to collect solar thermal energy and transfer the energy to the working fluid running in tubes embedded in them. A surface solar absorber utilizes a metal surface coated with a solar-selective thin film to convert solar energy into thermal energy. Due to the separation of the working fluid from direct contact with the sunlight, the fraction of solar radiation received by the working fluid depends entirely on the surface solar absorber. This solar thermal conversion process is, therefore, limited by the solar–thermal energy conversion efficiency of the surface solar absorber and the energy loss due to the heat transfer from the hot surface to the working fluid. The solar thermal process may look simple for a traditional solar collector, but to optimize the solar-to-thermal efficiency of the surface solar absorber, the corresponding design and fabrication may require much effort. Surface solar absorbers can be categorized into five different types, as shown in Figure 2-1: (a) intrinsic absorbers, (b) semiconductor absorbers, (c) multilayer interference stacks, (d) ceramic absorbers, and (e) textured surfaces [24].

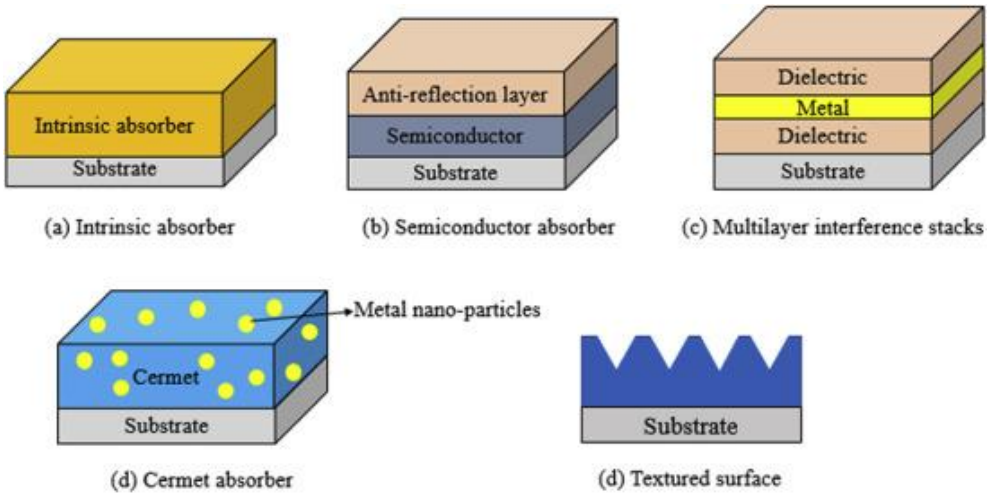

Figure 2-1. Schematic diagram of five typical solar absorbers [24].

Among the above-mentioned examples, multilayer interference stacks and ceramic absorbers are reportedly widely used [25], [26], [27], [28]. Each layer of multilayer interference stacks can be composed of metal, dielectrics, or metal-dielectric composite materials. Such designs possess high solar absorption, low thermal emittance, and are stable at high temperatures (>400ºC) depending on the materials used [29]. Despite the favorable properties mentioned above, multilayer interference stacks have very strict requirements for manufacturing precision. Cermet absorbers consist of one or more cermet layer(s) and a reflective substrate. Generally, a single homogeneous cermet layer does not show high solar absorbance by itself. Therefore, a complex design that contains multiple cermet layers is usually favored [30].

2.3 Volumetric Solar Absorbing Fluids

To date, various materials have been employed in potential applications. Through material selection, several criteria have been identified for the design of volumetric solar absorbing fluids:

1) Effective solar absorption—Volumetric solar absorbing fluids should be able to absorb solar light efficiently.

2) Long-term stability—Volumetric solar absorbing fluids should maintain consistent optical and physical properties over the long term use.

Numerous studies have been done to develop possible materials to prepare volumetric solar absorbing fluids. To meet the above criteria, different materials with efficient photothermal conversion have been developed, such as metallic materials, graphene-based materials, and dyes. As for stability concerns, the use of surfactants and surface modification of graphene-based particles have also been developed.

2.3.1 Nanofluids based on Metallic Materials.

To further increase the solar absorptivity of solar collectors, much attention has been directed to using nanofluids, which are dispersions of nanoparticles in heat transfer fluids, as volumetric absorbing fluids in solar collectors [11], [12]. Tyagi et al. [31] showed that Al nanofluids could improve the performance of a flat-plate volumetric solar collector by 10%. Suraj et al. [32] showed that the thermal efficiency of solar collectors can be enhanced by 1%–15% by volume of Fe_3O_4 nanofluids. Figure 2-2 lists the transmittance spectra of various nanofluids at the same concentration, and an overall transmittance decrease could be spotted for different nanofluids when compared with pure water.

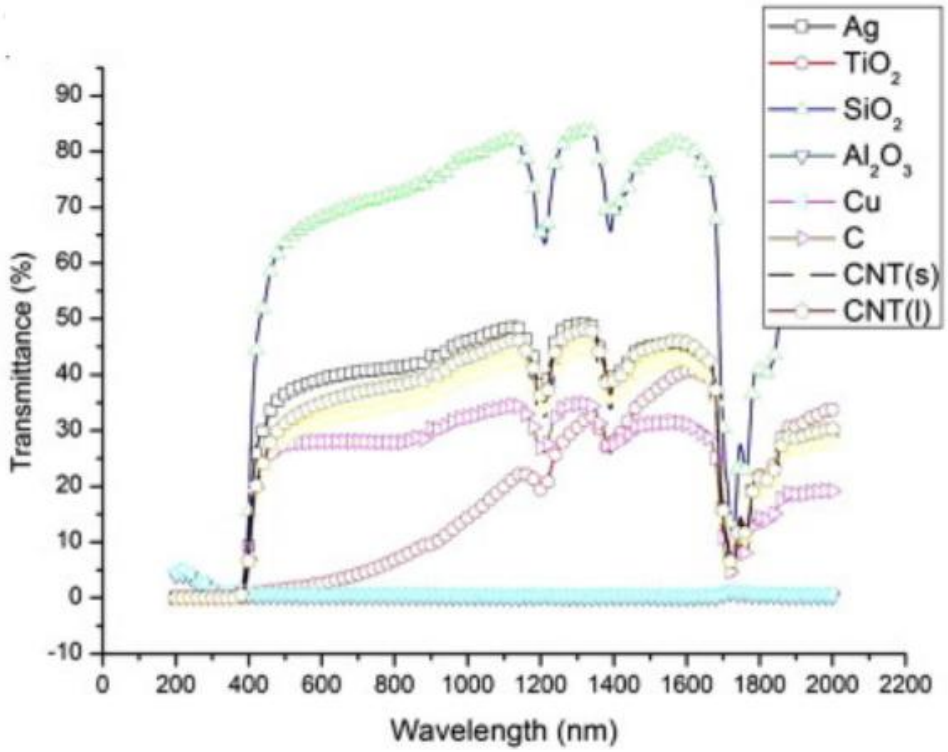

Figure 2-2. Transmittance spectra of different nanofluids with 0.01 wt.% loading [33].

Despite being solar absorptive, most metal or metal oxide nanofluids show poor stability due to the relatively large Van der Waals attractive force between nanoparticles, and their stability remains poor when prepared in water, due to the poor hydrophilicity of most metal nanoparticles. Cu and Ag, for example, were both reported to be unstable over time without the use of surfactant when prepared as nanofluids [34]. Figure 2-3 further demonstrates the sedimentation of Al_2O_3 nanoparticles without surfactant at different time from the preparation of nanofluids.

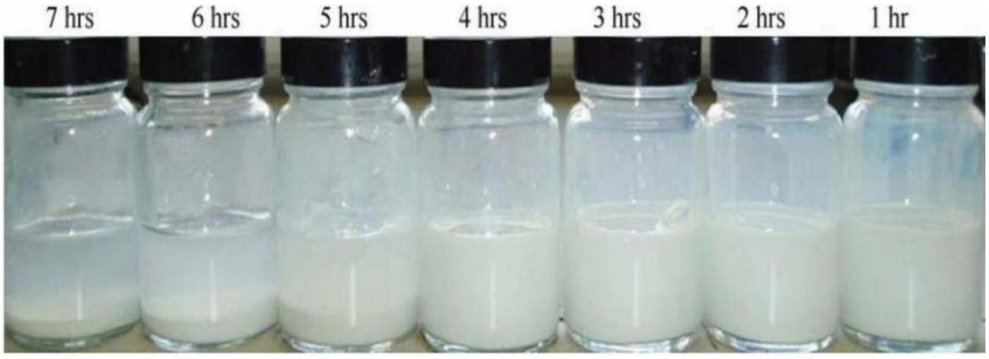

Figure 2-3. Sedimentation of Al_2O_3 nanoparticles (2.5 wt% Loading) without surfactant [35].

Table 1 gives further examples of metal and metal oxide nanofluids serving as working fluids in flat-plate solar collectors (FPSC). Notably, the stability of prepared nanofluids is enhanced by further methods. The maximum working temperature of FPSC mentioned in the table is below 80°C. And the stability of prepared nanofluids needs to be sustained with given methods.

Table 1. Summary of Nanofluids and Their Operating Conditions in FPSC.

Reference	Year	Nanofluids	Working temperature	Methods used to retain stability
Choudhary et al. [36]	2020	MgO/EG-DW	20°C–70°C	Cetyltrimethyl ammonium bromide (CTAB) surfactant
Kaya et al. [37]	2018	ZnO/EG-DW	10°C–50°C	polyvinylpyrrolidone (PVP) surfactant
Said et al. [38]	2016	Al_2O_3/DW	20°C–80°C	pH control
Said et al. [39]	2015	TiO_2/DW	20°C–80°C	pH control

2.3.2 Nanofluids based on Graphene-Related Materials

Carbon-based nanomaterials such as carbon nanotube (CNT), graphene, and GO have been investigated as thermal nanofluids, owing to such advantages as excellent solar-thermal conversion efficiency and thermophysical properties. For example, compared to metal or metal oxide nanoparticles, graphene nanosheets have high thermal conductivity, high solar absorptivity, and low mass density, so they are often used to prepare volumetric solar absorbing fluids [40]. Sadeghinezhad et al. [41] reviewed the thermal conductivity enhancement of ethylene glycol-based nanofluids compared with the pure ethylene glycol base. For most nanofluids containing metallic oxide, the enhancement ratios are in the range of dash lines and solid lines, as shown in (a), yet the enhancement ratios are much larger when it comes to graphene and GO nanofluids. Similar effects are found in research by Nanda et al. [42] as shown in (b),

in which it is clear that the rate of increase of enhancement with concentration of graphene is comparable and is much superior to metallic and ceramic nanofluid. The thermal efficiency of a solar collector has been found to increase by 29% with the use of graphene-based aqueous fluids at flow rates of 0.0075 kg/s when compared with that of the base fluid (water) [43]. Due to the hydrophobic surfaces of graphene, surfactants such as polymer dispersants are needed to prevent the agglomeration and precipitation of graphene nanosheets in the nanofluids.

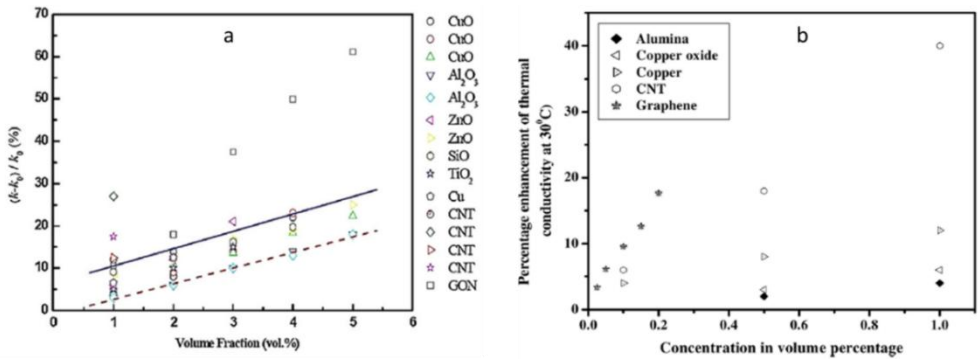

Figure 2-4. Thermal conductivity enhancement of ethylene glycol-based nanofluids (a, [41]) and water-based nanofluids (b, [42]).

2.4 Stability of Graphene based Nanofluids

Despite the advantages mentioned above, a key challenge with graphene-based nanofluids is that graphene nanoparticles tend to aggregate during preparation and processing time. Graphene sheets, unless well isolated from each other, tend to form irreversible agglomerates through van der Waals interactions [44], [45], [46], [47], [48]. The stability of nanofluids is defined as the rate of aggregation of nanoparticles dispersed in the base fluid, generally explained by the frequency and probability of collision [49]. According to the theory of Derjaguin, Verway, Landau, and Overbeek (DVLO) [50], [51], the stability of particles in base fluid is determined by the sum of

repulsive forces and Van der Waals forces. Particles will aggregate if the sum of Van der Waals forces surpasses the sum of repulsive forces. Otherwise, particles will be isolated from each other, and the prepared nanofluids will remain stable. The stability of prepared nanofluids deteriorates quickly as the particles agglomerate. Therefore, preventing the aggregation of graphene particles is of particular importance for graphene-based nanofluids.

There are two types of repulsive forces: steric repulsive forces and electrostatic repulsive forces. Steric stabilization and electrostatic stabilization can be reached accordingly due to corresponding forces. As shown in Figure 2-5, in steric stabilization, the particle surface is grafted with large molecules, usually long-chain polymers. The existence of surface steric hindrance could efficiently prevent particles from aggregation caused by Van der Waals forces. In electrostatic stabilization, an electrostatic charge is given to the particle surface, attracting a cloud of counterions around the particle. The attraction forces (Van der Waals forces) are then counterbalanced by the repulsive electric forces between clouds of counterions, protecting particles from aggregation [52], [53], [54].

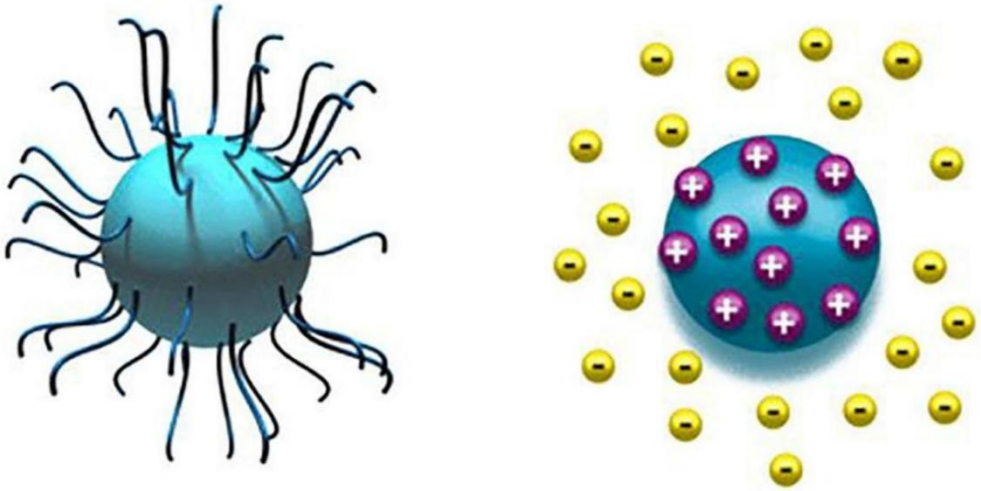

Steric stabilization Electrostatic stabilization

Figure 2-5. Mechanisms of steric stabilization and electrostatic stabilization [55].

2.5 Methods Reported to Maintain Stability of Nanofluids

Multiple methods are available to retain the stability of nonfluids, including but not limited to pH control, ultrasonication, the use of surfactant, and surface modification. The following sections detail each method.

2.5.1 pH Control

pH control is an efficient method to improve the stability of the nanoparticles [56], [57]. This is because the electrokinetic properties of the particle surface directly relate to the pH level of nanofluids. However, the effect of pH level on the stability of nanofluids relates closely to the properties of particles, and different types of particles are subject to different influences on stability caused by pH control [58], [59], [60]. For example, Wu et al. [61] reported in their work that SiO_2 nanofluids could remain stable without surfactant at a pH value of 9.7, while Al_2O_3 nanofluids needed to be prepared at a pH value of 4.9. Chang et al. [62] investigated the influence of pH values on the stability of CuO nanofluids. They found out that CuO nanofluids could remain stable without surfactant only at a pH value larger than 9.5.

2.5.2 Ultrasonication

Ultrasonication is a commonly used physical method to prepare nanofluids. Particle agglomeration before dispersion could occur due to storage and the typical manufacturing process, and such weak-bonded particles could be broken into particles of much smaller size by ultrasonication. The stability of nanofluids prepared by ultrasonication is therefore enhanced [63], [64]. As seen in Figures 2-6(a) and 2-6(b),

there are two types of sonicators available: bath sonicators and probe sonicators. It was also reported that nanofluids prepared by a probe sonicator usually showed better stability than those prepared by a bath sonicator [65].

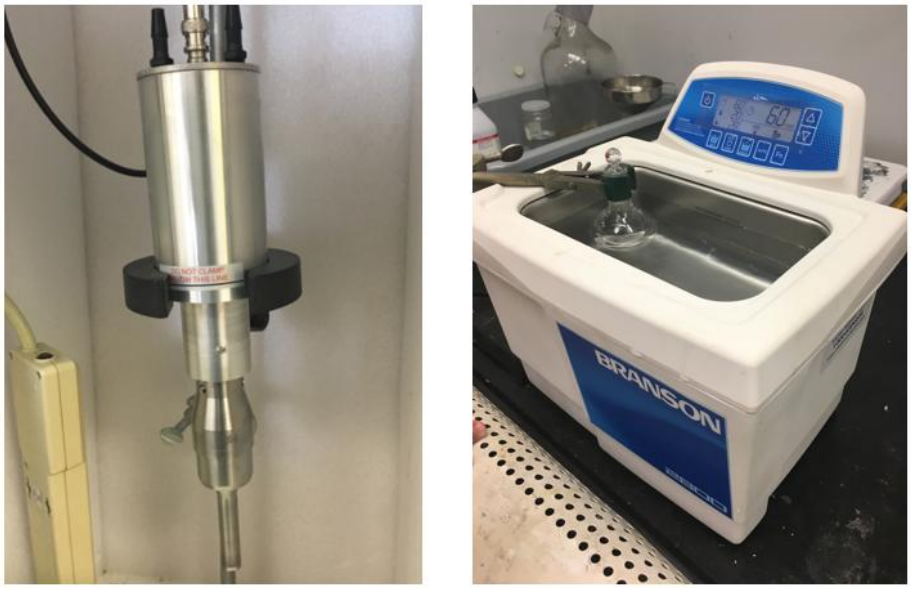

(a) (b)

Figure 2-6. (a) Probe sonicator (b) and bath sonicator.

2.5.3 Addition of Surfactants

Surfactants have effective applications in avoiding particle agglomeration. Adding proper surfactants to nanofluids can reduce the surface tension between the base fluid and dispersed particles, enhancing the stability of the nanofluids [66]. Most surfactants have a hydrophilic "head" part and a hydrophobic "tail" part. The "head" part usually contains polar groups tending to increase the hydrophilic behavior of particles. The "tail" part usually contains hydropobic groups such as long-chain hydrocarbons. By adjusting the length of the "tail" part, surfactants could be adjusted from oil-soluble to water-soluble. The solubility of a typical surfactant can be estimated from the hydrophilic/lipophilic balance (HLB) value. The HLB value is

determined by calculating percentages of molecular weights for both the hydrophilic and lipophilic portions of the surfactant molecule, with a range of 1–20 [67]. Generally, water-soluble surfactants have a larger HLB value, and oil-soluble surfactants have a smaller HLB value.

Rohini Priya et al. [68] studied CuO/water nanofluid stability with different surfactant ratios. Additionally, the minimum CuO:Tiron ratio required to ensure colloidal stability is 2.5:1. Fadhillahanafi, N. M. et al. [69] investigated CNT/water nanofluid stability with and without surfactant, finding that the water-based 0.05 wt% CNT nanofluids prepared without using polyvinylpyrrolidone (PVP) as surfactant exhibited particle sedimentation immediately after the sonication process. Moreover, their work found that 0.05 wt% CNT nanofluids prepared with 0.01 wt% PVP remained stable for over one month at room temperature without sedimentation.

2.5.4 Surface modification

Among the above methods, pH control and surfactant addition will inevitably introduce other types of particles to the as-prepared nanofluids, which could lead to problems such as corrosion and changes to their thermophysical properties. Surface modification of particles, however, contribute no other particles to the original nanofluids. This process is usually accomplished by grafting suitable functional groups to the surface of particles [70]. By selecting proper functional groups, the surface of particles could be tuned from hydrophilic to lipophilic. Consequently, modified particles could be dispersed into base fluids with better stability.

As shown in Figure 2-7, surface modification of GO particles changes the surface condition of the GO nanosheet only by oxidizing the graphene surface. Therefore, to mitigate the stability issue of graphene-based nanofluids, much effort has been put into the surface modification of graphene nanosheets.[71], [72], [73],

[74], [75], [76], [77]. Oxidized graphene nanosheets comprise hydrophilic particles, due to the presence of oxygen-containing functional groups on their surface. GO nanosheets are now considered a better choice in the application of solar absorbing fluids. Liu et al. [34] reported volumetric solar absorbers based on GO nanofluids, and their samples showed UV-vis absorbance change less than 5% after storing for 10 days at room temperature.Wisut Cham-Saard et al. [77] also reported GO nanofluids used for low-temperature solar absorption, and their samples showed a 1.7% drop in absolute zeta potential after storing at room temperature for over six months.

Figure 2-7. Chemical structure of graphene and graphene oxide [78].

2.6 GO Nanofluids in Solar Collectors

GO nanofluids are reported to be widely used for solar steam generation [79], [80], [81], [82]. As shown in Table 2, the working temperature is usually lower than 80°C, and GO nanofluids are used alone without additional methods to maintain the stability of the working fluid. GO particles are also reported to be partially reduced to graphene oxide by either a chemical agent or exposure to UV irradiation, rather than using GO nanofluids directly for solar collectors. Pristine graphene possesses both higher thermal conductivity and solar absorptivity than GO, while GO shows much better stability than graphene when prepared as nanofluids in water. By partially

reducing the GO particles to a certain level, a theoretical balance between stability and solar/thermal performance can be reached.

Table 2. Summary of rGO Nanofluids and Their Operating Conditions in FPSC.

Reference	Year	Working fluids	Working temperature	Stability evaluation
Liu et al. [34]	2018	rGO in water	20-80°C	More than 10 days
Hong et al. [81]	2019	rGO in water	26°C	/
Chen et al. [80]	2017	rGO in water	20-70°C	Zeta potential close to 30 mV at 70°C

In addition to being stable at room temperature, GO nanofluid samples are also reported to remain stable below 180°C. As demonstrated by Niu et al. [83], the reduction reaction was observed at 180°C and warmer, where the oxygen-containing functional groups decomposed in 24 h. Below 120°C, GO sheets underwent cross-linking reactions to form unstable GO aggregates in a hydrothermal process. With increasing temperature to 160°C, the GO aggregates were successfully dissolved in water and could transform into homogeneous GO nanofluids again, as seen in Figure 2-8.

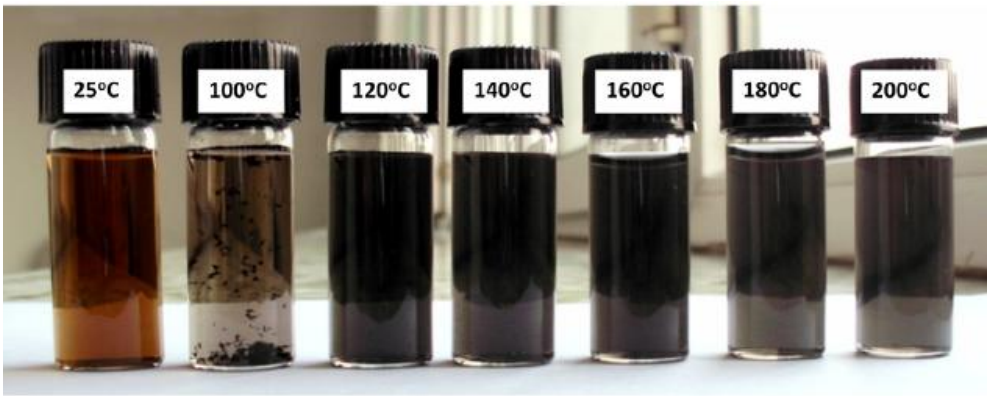

Figure 2-8. GO nanofluids after thermal treatment [83].

2.7 Aqueous Dyes Solution as Volumetric Absorbing Fluids

Textile dyes are chemical compounds that can stick to a fabric, and these chemical compounds can absorb light in the visible range (~350–700 nm). Dye molecules usually contain chromophores, which are responsible for their color, and auxochoromes, which intensify the color. Textile dyes are conventionally used to dye fabrics with durable colors. Thanks to the prosperity of the textile industry, there are numerous types of dye with different colors and solubility to choose from. Different types of dyes are present in the market, classified regarding chemical structure and application [84]. However, due to the complexities of the chemical structure system, classification based on application is often favored [85], as presented here:

1) Acid dyes usually contain a carboxyl, a sulfonic acid group, a hydroxyl, or other soluble group in the molecular structure, and these are used in acid or neutral dye baths.

2) Basic dyes mainly include salts generated by aromatic bases reacting with acids. These groups of dye usually dissolve in water and dissociate into dye cations and acid anions.

3) Direct dyes are usually sodium salts of aromatic compounds. They are soluble in water, and their solubility increases with temperature.

4) Other types of dyes, like dispersed dyes, vat dyes, and sulfur dyes, are mostly reported not to be soluble in water.

The total dye consumption worldwide is more than 10,000 tons/year, and around 100 tons/year of dyes are discharged as wastewater [86]. The result is that the degradation of dye is also widely studied as a method of wastewater treatment. It is hard to remove dye from water by the conventional method, since textile dyes are designed to be resistant to degradation from the very beginning. However, few papers

have discussed the possibility of aqueous textile dye solutions serving as potential volumetric solar absorbing fluids.

2.8 Two-Phase Thermosyphon

The two-phase thermosyphon is among the most commonly used systems designed to utilize natural phase-change cycles [87]. This passive system requires no mechanical pumps or other moving parts within the fluid loop. Figure 2-9 shows the principles of both the traditional two-phase thermosyphon and the loop two-phase thermosyphon. In both cases, a high heat flux will be provided to the working fluid to produce vapor. Vapor produced by phase change in the evaporator is then flowed towards the condenser, where it is further condensed into liquid. In traditional two-phase thermosyphon, the rising vapor shares the same tunnel as the condensed liquid. When the vapor velocity is high, the shear of the vapor traveling to the condenser could prevent the liquid film on the wall from returning to the evaporator, therefore limiting the efficiency of the system. Such a limit on heat transfer is called “the flooding limit” [88]. In loop two-phase thermosyphon, however, both the vapor and the liquid move in the same direction. The flooding limit is therefore bypassed by the loop design.

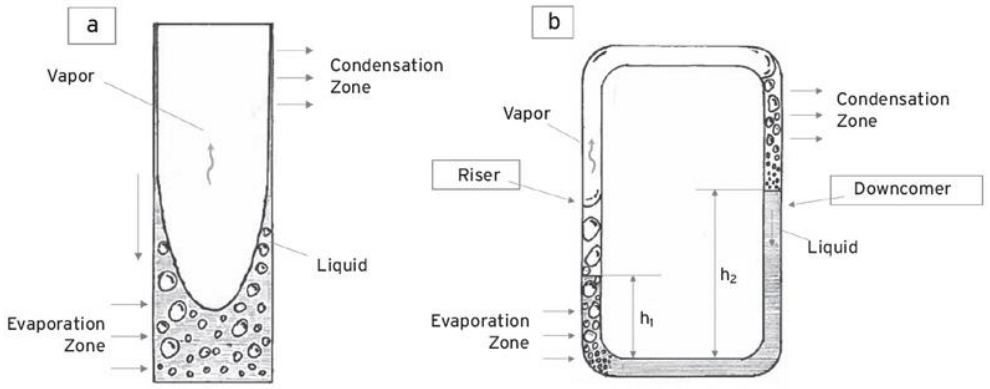

Figure 2-9. Schematic of a (a) Traditional two-phase thermosyphon and (b) Loop two-phase thermosyphon [89].

Nanofluids are widely reported to be employed as working fluids to enhance heat transfer in two-phase thermosyphons due to their improved thermophysical properties [90], [91], [92]. It has been wildly observed that, when compared with using pure fluid as a working fluid, employing nanofluids usually raises thermal performance [93]. Some of the analyses of nanofluid use in two-phase thermosyphons are summarized as follows: Liu et al. [94] evaluated the thermal performance of two-phase thermosyphons using CuO/water nanofluids as working fluids. They reported that the boiling heat transfer performance was significantly enhanced in comparison to pure water. Noie et al. [95] investigated the thermal performance of two-phase thermosyphons using Al_2O_3/water nanofluids as working fluids, observing that the overall system performance increased to around 15% in comparison to pure water. Huminic et al. [96] studied the effect of using iron oxide/water in two-phase thermosyphons. They showed a maximum heat transfer enhancement of 19%, in comparison to pure water.

The external heat transfer structure of an evaporator can be further designed to utilize solar-thermal radiation; therefore, a two-phase thermosynthetic system is also widely used to harvest solar energy [97]. Negm et al. [98] evaluated the performance of using Al2O3/water nanofluids in a two-phase thermosyphon flat plate solar collector. They observed that the collector efficiencies increased by 8.06% and 16.63% with nanofluids of 0.5wt% and 1.0wt% respectively. Chougule et al. [99] investigated the performance of using CNT/water nanofluids in a thermosyphon flat plate collector. They reported that the overall collector efficiencies were significantly improved by using CNT/water nanofluids in comparison with pure water.

2.9 Summary

For applications in two-phase thermosyphons, ideal working fluids must be engineered with a broad solar absorption wavelength range and high stability over the working temperature range of the system. Nanofluids are wildly utilized in heat transfer mediums due to their excellent optical and thermal properties. Based on the reviewed research, metal, metal oxide, and graphene-based nanoparticles can be applied in thermosyphons to improve overall performance. Although an increase in the concentration of nanoparticles leads to both higher thermal conductivity and solar absorptivity, it also leads to a higher possibility of particle agglomeration, which may cause stability deterioration and degradation of system performance. Different methods, including pH control, the addition of surfactant, and surface modification, are reported as effective methods to improve the stability of nanofluids. However, such methods are highly dependent on the types of nanoparticles and working conditions such as temperature, concentration, base fluid, and so on. In addition, there have been few studies related to the long-term stability of nanofluids in two-phase thermosyphons. Furthermore, most nanofluid-related studies have reported the operation of systems only over a couple hours. Apart from nanofluids, textile dyes are also reported to have both good stability and solar absorptivity, such that aqueous dye solutions could be potential candidates as volumetric solar absorbing fluids. However, few reports have discussed the possibility of aqueous dye solutions as volumetric solar absorbing fluids.

Charpter 3. Experimental Measurement

3.1 Microstructure and Thermophysical Property Characterization methods

Property characterization includes the investigation of nanoparticles and prepared fluids. The characterization of nanoparticles covers the investigation of particle morphology, elemental composition, and functionalities. Characterization of fluids includes investigation of optical properties, thermal conductivity, viscosity, and stability. Monitoring these property changes can help illuminate the influence of various working conditions. Doing so is also important to deepen our understanding of the mechanisms and to evaluate nanoparticles and fluids.

3.1.1 Ultraviolet–Visible Spectroscopy

Ultraviolet–Visible (UV-Vis) spectroscopy is one of the most widely used tools to study the optical properties of materials. The only requirement to apply such a method is that particles can absorb light in the near UV region or visible region of the spectrum, making it applicable to various types of fluids. Once particles absorb light in the UV-Vis region, the corresponding electron of the compound or material is then excited from the ground state to the first singlet excited state. Pattern information of the UV-Vis spectra can give both qualitative and quantitative analysis of a given compound or molecule. It has also been widely used to quantitatively characterize the stability of various dispersion [100]. Stability is evaluated by measuring the transmission peak or absorption peak characteristics constantly at different time intervals [101]. A decrease in absorbance over time usually signals the stability and deterioration of fluids. The Beer-Lambert law gives the linear relationship between the absorbance and the particle concentration as follows [102]:

$$A = \varepsilon l c, \quad (1)$$

where A is the absorbance, ε is the absorptivity, l is the optical path length, and c is the concentration of suspended particles.

Transmittance (T) can be converted to absorbance, and vice versa, as follows:

$$T = 10^{-A}, \quad (2)$$

The increase in transmittance value with time indicates a decrease in particle concentration caused by particle agglomeration and sedimentation. However, only fluids with low particle concentrations can use such a method to measure stability [103].

In this work, 10 mm vials were used in the test, and a UV-Vis spectrometer (Perkin-Elmer Lambda 25) was used to collect the transmittance data. Further, the transmittance data of fluids is used for both the evaluation of optical properties and for the stability analysis.

3.1.2 X-ray Photoelectron Spectroscopy

X-ray photoelectron spectroscopy (XPS) is a surface-sensitive method to characterize the elemental compositions of nanoparticles. When X-rays are shot onto a sample, electrons in the sample that have absorbed enough energy are then removed from the sample with certain kinetic energy. Ejected electrons are then captured by an electron detector, and the spectra are then produced by a computer according to the energy pattern of the ejected electrons. The atoms present in a compound are determined according to the following equation:

$$E_{binding} = E_{photon} - (E_{kinetic} + \emptyset), \quad (3)$$

where $E_{binding}$ is the binding energy of an electron attracted to a nucleus, E_{photon} is the energy of the X-ray photons being used, $E_{kinetic}$ is the kinetic energy of ejected

electrons captured by the detector, and ϕ is the correction factor for the instrument. Due to the unique electronic structure of different molecules, the wavelength of the output characteristic X-rays is also unique. Such information could be used for the characterization of the chemical compositions of materials. In this work, XPS is an analytical tool used to identify the atomic ratio of GO nanoparticles. An X-ray photoelectron spectrometer (Kratos Axis 165 Photoelectron Spectrometer) is used to collect the spectra.

3.1.3 Fourier-Transform Infrared Spectroscopy

Fourier-transform infrared spectroscopy (FT-IR) is a key method used to characterize functional groups and chemical bonds in a molecule. When IR light interacts with a molecule, some of the radiation is absorbed by the molecule and initiates the vibration of chemical bonds. The rest of the radiation passes through the sample and is then captured by the detector. Each chemical bond in a molecule has characteristic vibrations. Therefore, the required energy to initiate vibrations varies. The spectral bands of all these different functional groups together form a spectrum that can be further interpreted. In this work, to identify and investigate the degradation mechanism of GO nanoparticles and dye molecules, spectra were collected using an attenuated total reflectance (ATR) – Fourier transform infrared (FT-IR) spectroscopy technique (Thermo Nicolet NEXUS 670 FT-IR). The ATR-FT-IR measurement applied a germanium crystalline prism with a spectra range of 600–4000 cm^{-1}. The FT-IR spectra could be used to identify the characteristic functional groups in the spectral bands. By comparing characteristic peaks before and after certain experiments, molecular degradation could then be identified.

3.1.4 Thermal Conductivity Measurement

Multiple methods, such as steady-state parallel plate [104], transient hot wire [105], temperature oscillation [106], and 3ω [107] have been developed to measure thermal conductivity. In this measurement, a combination of the 3ω method and the hot-wire method is developed and applied to measure the thermal conductivity of the nanofluid. The thermal conductivity is determined by detecting the dependence of temperature oscillation on frequency. In the meantime, a metal wire immersed in the nanofluid acts as both a heater and a thermometer. In the measurement, a current at frequency ω goes through the metal wire heater, and then a heat wave at frequency 2ω is generated. The thermal conductivity of the nanofluid, *k*, is determined by Equation (4).

$$k = \frac{p}{4\pi l}\left(\frac{\partial T_{2\omega}}{\partial \ln \omega}\right)^{-1}, \quad (4)$$

where p is the electric power, l is the length of the metal wire heater, ω is the frequency of the electric current, and $T_{2\omega}$ is the amplitude of temperature oscillation at frequency 2ω in the metal wire heater.

The thermal conductivity enhancement of nanofluid is calculated by Equation (5).

$$\text{Thermal conductivity enhancement} = \frac{k_{nf} - k_{bf}}{k_{bf}} \times 100\%, \quad (5)$$

where k_{nf} is the thermal conductivity of nanofluid and k_{bf} is the thermal conductivity of base fluid.

In this work, a homemade lab-scale 3ω-wire system is to measure thermal conductivity of fluids [108]. A water temperature bath is used to keep fluids at different temperatures during the measurement. Each measurement was repeated three times, and the mean value was used as the thermal conductivity of fluids.

3.1.5 Viscosity measurement

Viscosity is a key parameter in the heat transfer properties of the fluid. It is also an important indication to evaluate the ability of the working fluids to circulate inside a two-phase thermosyphon. The viscosity of working fluids depends on both the weight fraction of particles and the viscosity of the base fluid. Other parameters such as temperature, particle types, and size also contribute to the effects of viscosity. The relative dynamic viscosity is defined thus:

$$Relative\ dynamic\ viscosity = \frac{\mu_{nf}}{\mu_{bf}}, \quad (6)$$

where μ_{nf} is dynamic viscosity of nanofluid and μ_{bf} is the dynamic viscosity of base fluid. As shown in Figure 3-1, a viscometer (Brookfield DV-I Prime) is used for the viscosity measurement of GO nanofluids. Additionally, a water temperature bath is used here to monitor how viscosity of fluids changes with temperature. The viscosity of pure water is also measured first, and the results are compared with viscosity of pure water provided by National Institute of Standard and Technology (NIST) to ensure the precision of the viscometer measurement. The instrument has a ±0.1 cP accuracy. In this work, each measurement was repeated five times, and the mean value was used as the result.

Figure 3-1. Viscometer (Brookfield DV-I Prime) used for the viscosity measurement.

3.1.6 Transmission Electron Microscopy and Scanning Electron Microscopy

Transmission electron microscopy (TEM) and scanning electron microscopy (SEM) are powerful methods used to acquire images formed from the interaction of the electrons with the sample. The main difference between TEM and SEM is that TEM collects information from transmitted electrons, while SEM uses reflected electrons. Therefore, TEM provides more information on the inner structure of the sample, while SEM focuses more on surface topography. Due to the requirement for transmitted electrons, TEM samples are also required to be very thin and as flat as possible, while SEM samples have a lower requirement. In this work, morphology characterization was investigated with both TEM and SEM. About 10 microliter fluid

sample was dropped on a lacey carbon grid using a micropipette, and then it was dried at room temperature before being sent for the TEM inspection (JEM 2100 FE-TEM). SEM inspection is conducted using a field-emission scanning electron microscope (Hitachi SU-70 Schottky FE-SEM). SEM samples were prepared by drying the fluid on a piece of silicon wafer.

3.2 Stability Test Methods

Test methods include sample preparation, surface modification, stability testing under various conditions, a long-term two-phase thermosyphon test, and an enhanced UV resistance test. The details of each test are given below.

3.2.1 Sample Preparation for Nanofluids

In this work, deionized water was used as the base fluid. It had an electrical conductivity of 0.047 μS, which was measured at room temperature using an Orion A212 Conductivity Benchtop Meter. Ultrasonication provided by a probe-type sonicator (Sonics, VCX 750, 300W) is applied for 10 min at 40% amplitude intermittently to properly disperse particles in water. The glass vial with prepared samples was maintained at room temperature in a water bath during the ultrasonication treatment.

3.2.2 Surface Modification of GO Naonoparticles

The UV lamp curing system (SunSpot 2, Uvitron) was used to modify the atomic ratio of the C to O ratio of the GO sample and, thus, to reach a balance between the solar absorptivity and stability of the GO nanofluids. The experiment setup is shown in Figure 3-2(a). A 365 W LED bulb emitting at a wavelength of 365 nm was used in the experiment. As shown in Figure 3-2(b), about 1 W/cm^{-2} UV

beam was expected as the lightguide was placed at 1.5 inches from the nanofluid's surface.

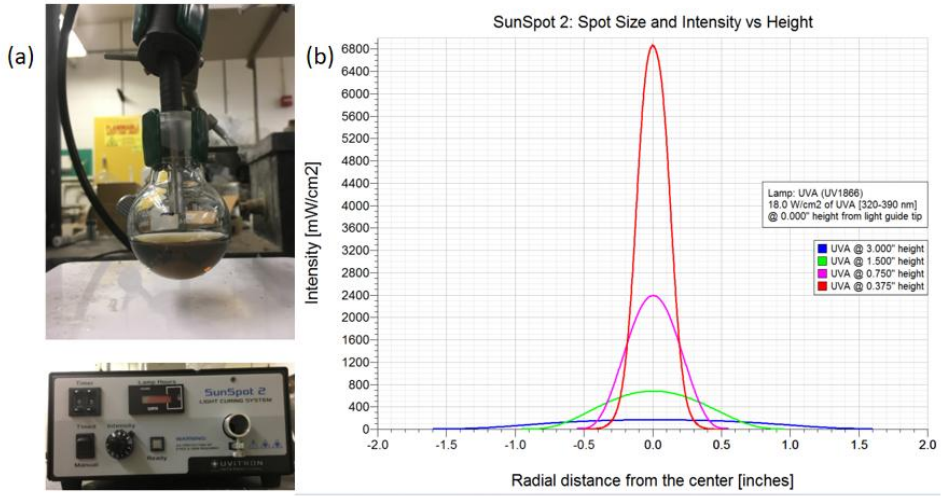

Figure 3-2. (a) UV lamp curing system used to modify the atomic ratio of the C-to-O ratio of the GO sample. (b) Spot size and intensity as a function of distance [109].

3.2.3 Stability Test Under Centrifugal Force

The stability of GO nanofluids was evaluated under centrifugal force. The transmittance of GO nanofluid samples was examined after applying centrifugal force for a certain time. Such a system could accelerate stability measurements, as larger particles settle faster under normal gravitational force. The GO nanofluid samples were centrifuged using a temperature-controlled centrifuge (L-K Industries Benchmark S Centrifuge) at a speed of 1500 rpm and a temperature of 90°C for 3 h. The speed of 1500 rpm is equivalent to 630 g. The GO nanofluid samples tested in the centrifuge had a weight concentration of 0.02%. The transmittance spectrum of the nanofluid samples was measured every hour during the centrifugation process.

3.2.4 Sealed Tube Test Without Boiling

A sealed tube test was performed to test whether the GO nanofluids were stable at the proposed temperature (120°C) without boiling. In this experiment, the GO nanofluid sample was placed in a sealed glass tube, further immersed in a temperature-controlled oil bath (120°C). This experiment lasted nine days.

3.2.5 Boiling and Condensation Experiment

This test was designed to study the influence on sample stability by boiling-condensation conditions, and the experiment setup is shown in Figure 3-3. In the boiling and condensation experiment, samples were boiled by immersing them in an oil bath at around 120°C, and the condenser was cooled by water at room temperature. All samples used in this experiment had a weight concentration of 0.02%, and the volume of the samples was 50 mL. Both the transmittance spectrum and FT-IR spectra of the tested samples were measured and compared throughout the boiling and condensation processes.

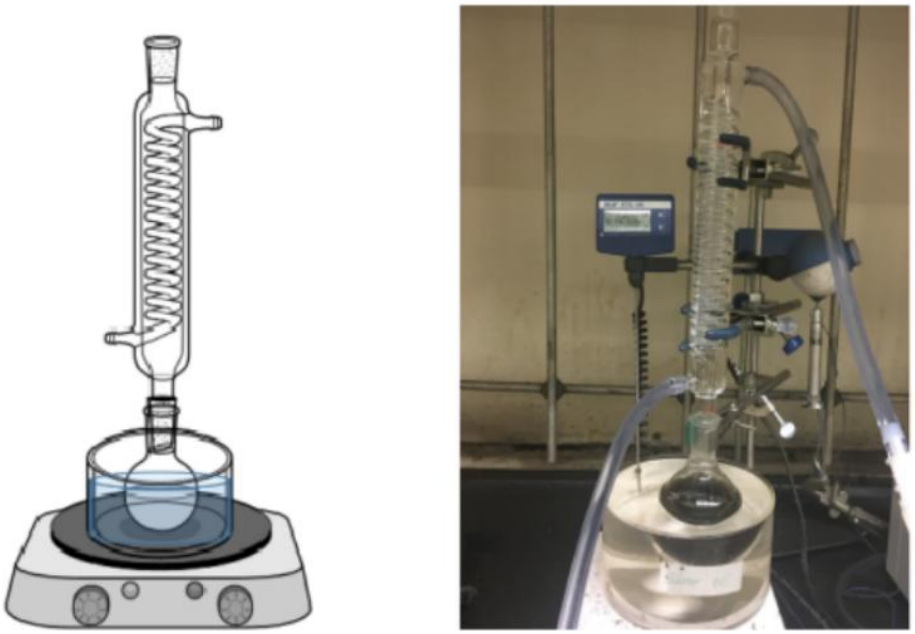

(a) (b)

Figure 3-3. (a) Schematic and (b) Picture of the experiment setup for the boiling and condensation experiments [110].

3.2.6 Two-Phase Thermosyphon Experiment

The fluid showed good thermal stability in the above boiling and condensation experiments and was further tested in a two-phase thermosyphon serving as the working fluid. The working fluid is naturally circulated inside the two-phase thermosyphon due to buoyancy effects and gravity without using an external pump [111]. The two-phase thermosyphon consisted of an evaporator, a riser, a condenser, and a downcomer, as shown in Figure 3-4. The condenser was placed higher than the evaporator for fluid circulation. This two-phase thermosyphon prototype was designed and built with the help of Advanced Cooling Technologies, Inc. (ACT). However, the two-phase thermosyphon prototype shown in Figure 3-4 is made of copper tubes. After characterization of borosilicate glass transmittance over the solar spectral range, a double-wall evacuated glass tube with an optical to thermal efficiency of 85% or above was developed and used to assemble the two-phase thermosyphon.

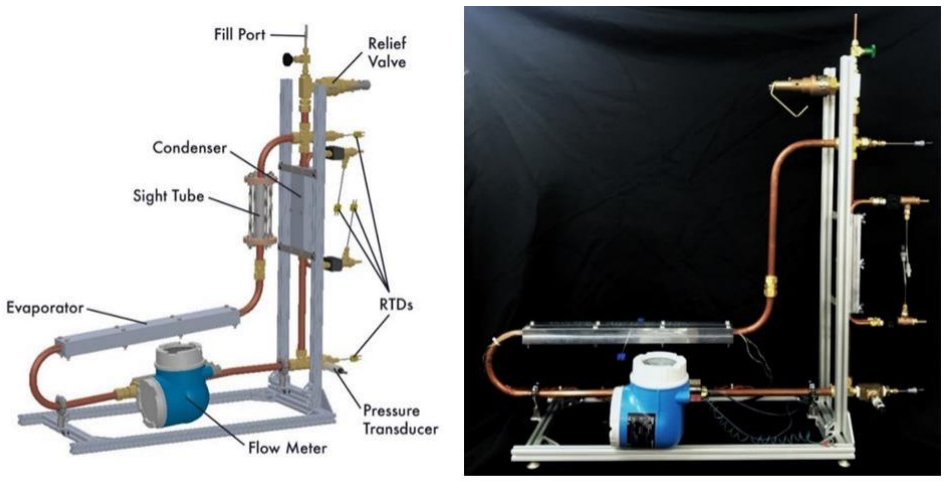

Figure 3-4. (a) Model and (b) Picture of a two-phase thermosyphon prototype.

3.2.7 Enhanced UV Resistance Experiment

To determine the effect of UV exposure time on the degradation of solution, the fluid was exposed to UV radiation five times the flux of the entire UV spectrum of solar radiation for a total of 191 days. The experimental setup is shown in Figure 3-5. A 100 W LED array emitting at a wavelength of 365 nm was mounted above a cylindrical chamber. Optics were used to direct a cone of UV light from the LED array onto the fluid reservoir, passing through the transparent reservoir cover to be directly incident on the fluid. Such method provided a flux of approximately 394 W/m^2 onto the surface of the 12.7-cm-diameter fluid reservoir. The amount of light is equivalent to approximately 5× the intensity of the UV portion of the solar spectrum. The LED array is cooled by a heat sink and integrated fan, with the fluid reservoir similarly cooled by a separate heat sink and fan. A drain port located on the side of the fluid reservoir is used for filling and draining the fluid and to remove samples of the fluid for evaluation.

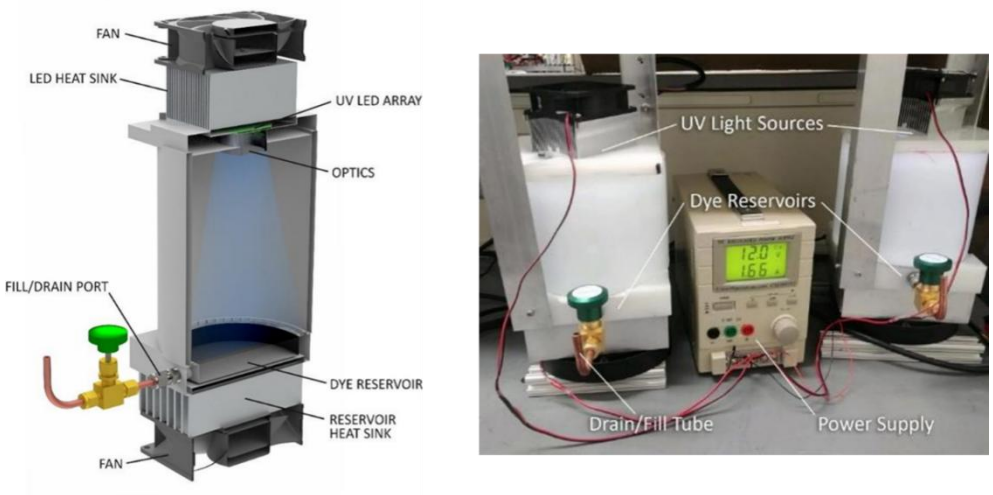

Figure 3-5. (a) Schematic and (b) Picture of the experiment setup for the UV resistance test of the dye aqueous fluid.

Charpter 4. Graphene Oxide Nanofluids for Volumetric Solar Absorption

4.1 Introduction

Conventional fluids, such as ethylene glycol, water, and heat transfer oils, are reported to have both low thermal conductivity and solar absorption properties, so nanofluids tend to outperform pure fluids as volumetric solar absorbing fluids in solar collectors [112]. By dispersing nanoparticles like Al, Cu, Ag, Al_2O_3, CuO, Fe3O4, and GO into pure fluids, different types of nanofluids are prepared. The use of nanofluids in solar collectors has been found to significantly enhance the photo-thermal conversion performance of solar collectors [113]. Compared with other nanofluids, GO-based nanofluids reportedly exhibit much better stability, along with good optical absorption properties and high thermal conductivity [114], [115], [116], [117], [118], [119], [120], especially when prepared in water. The atomic ratio of GO nanoparticles can be further modified by reduction, including thermal reduction, chemical reduction, and UV reduction [120]. By partially reducing GO nanoparticles into rGO nanoparticles, both thermal conductivity and solar absorptivity can be further increased without causing too much influence on the stability of nanofluids. rGO nanofluids are widely reported to be used in solar steam generation, which usually operates below 100°C [34], [80], [81], [122], and both the photo-thermal conversion performance and stability of rGO nanofluids have been variously acknowledged [34], [123], [124], [125], [126]. The application of GO nanofluids in solar steam generation has been reported by many authors [34], [127], [128], [129]. Compared with pure water, these nanofluids' water evaporation efficiency was reported to be significantly increased at an operating temperature below the boiling

point. Liu et al. [34] demonstrated a 40% increase in water evaporation efficiency with an irradiation power of 7 kW/m^2. Fu et al. [127] reported that the water vaporization efficiency of GO-Au nanofluids could be up to 59.2% at room temperature in natural sunlight. Ghafurian et al. [128] reported that the water vaporization efficiency of GO nanofluids was enhanced by 10% at the intensity of 1.5 Suns. Hong et al. [129] showed that water vaporization efficiency could be up to 69% at 4 suns.

GO reduction can be achieved by thermal reduction, chemical reduction, and UV reduction. Thermal reduction is usually carried out by thermal annealing, usually occurring at temperatures over 500°C [130], [131], [132], [133], [134]. In addition to operating temperature, the annealing atmosphere is also important for the thermal reduction of GO. Since oxygen etching will be increased at high temperatures, oxygen gas should be excluded or replaced with inert gas during thermal annealing [135]. Chemical reduction usually involves the use of reducing reagents, which can transform GO into graphene. Such chemical reactions are usually carried out at room temperature or by moderate heating. However, chemical reduction often involves the use of expensive and highly toxic chemicals such as hydrazine [136], [137], [138], sodium borohydrides [139], [140], and hydrohalic acid [141], [142]. UV reduction is executed by irradiating GO particles with UV light, and a deoxygenation reaction is then triggered. Compared with thermal and chemical reduction, UV reduction is usually completed at room temperature without involving any other chemical reagent [143], [144], [145], [146]. Other advantages of UV reduction include fast treatment of GO nanofluids and flexibility in processing as UV exposure time could be precisely manipulated. Thus, UV reduction is applied in this work to adjust the atomic ratio of prepared GO nanofluids.

The stability of GO nanofluids is evaluated by multiple methods in this chapter. The stability of GO nanofluids at room temperature is first tested by placing prepared GO nanofluids at room temperature for 30 days. The stability of GO nanofluids at high temperatures (90°C) is also evaluated under centrifugal conditions. These two experiments focus on stability performance when the temperature is lower than 100°C. As for conditions when the temperature is above 100°C, the sealed tube test is carried out by immersing sealed tubes containing GO nanofluid samples in an oil bath at 120°C for up to 9 days. With the tubes sealed, GO nanofluid samples remain homogeneous without boiling during the experiment. A boiling and condensation experiment is then conducted to study the influence created by the involvement of the boiling-condensation processes.

4.2 Structure of Graphene Oxide

Although GO was developed more than 100 years ago, its precise structure remains unknown. To further understand the extent of thermal stability for GO, its chemical structure must be fully understood. The model of GO structure now widely accepted is shown in Figure 4-1. The carbon plane is decorated with multiple oxygen-containing functional groups [147]. There are four main kinds of oxygen-containing functional groups that exist on GO:

1) Epoxide (-O-)
2) Hydroxyl (-OH)
3) Carbonyl (-C=O)
4) Carboxyl (-COOH)

Epoxide and hydroxyl groups are primarily in the basal plane, while carbonyl and carboxyl groups are primarily distributed at the edges. It is necessary to

understand how to maintain the carboxyl groups on the edges (prevent reduction), as they primarily contribute to the hydrophilicity of GO.

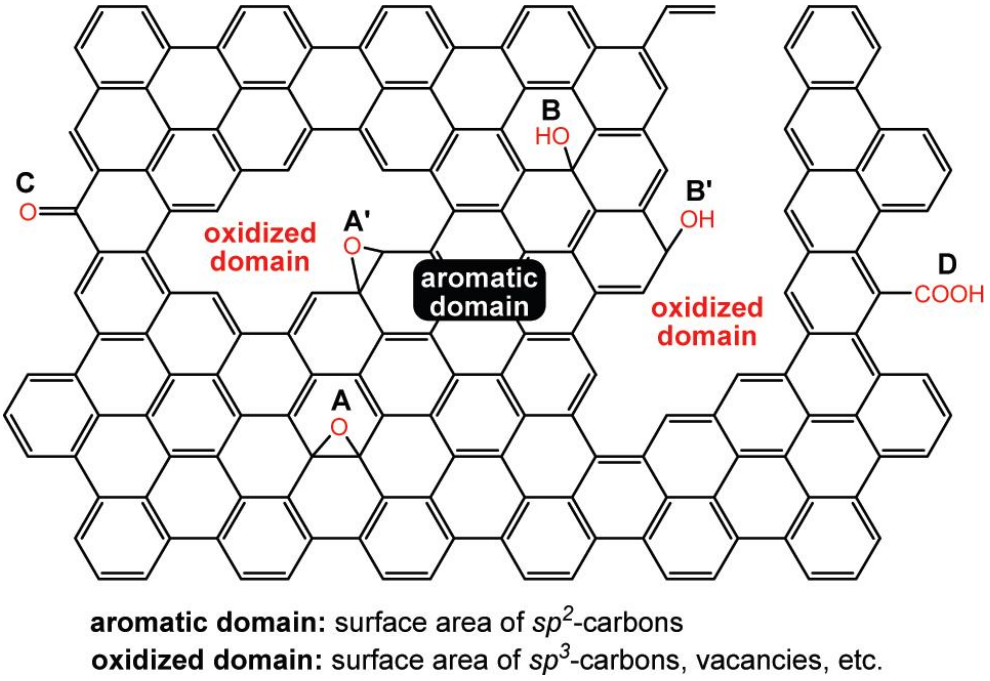

Figure 4-1. Schematic Illustration of Oxygen-Containing Functional Groups in GO. A, epoxide located at the interior of an aromatic domain of GO; A′, epoxide located at the edge of an aromatic domain; B, hydroxyl located at the interior of an aromatic domain; B′, hydroxyl at the edge of an aromatic domain; C, carboxyl at the edge of an aromatic domain; and D, carboxyl at the edge of an aromatic domain [148].

4.3 Preparation of GO Nanofluids

The GO nanoparticles were purchased from Graphene Laboratories Inc. (Ronkonkoma, NY, USA) and used as received. GO powder was added to water to form nanofluids with different weight fractions. Provided by a probe-type sonicator, ultrasonication was used to uniformly disperse GO nanoparticles in water.

4.4 Transmittance Measurement of GO Nanofluids

Figure 4-2(a) presents the digital photo of as-prepared GO nanofluids, while Figure 4-2(b) graphs the transmittance spectra of as-prepared GO nanofluids with weight fractions of 0.01%, 0.025%, and 0.05%. Low-concentration GO nanofluids are light brown and transparent, darkening as the concentration increases. The GO nanofluids are very absorptive in the solar spectrum, and GO nanofluids are far more absorptive than pure water. The transmittance of GO nanofluids decreases as the concentration of GO particles increases, agreement with the Beer-Lambert law.

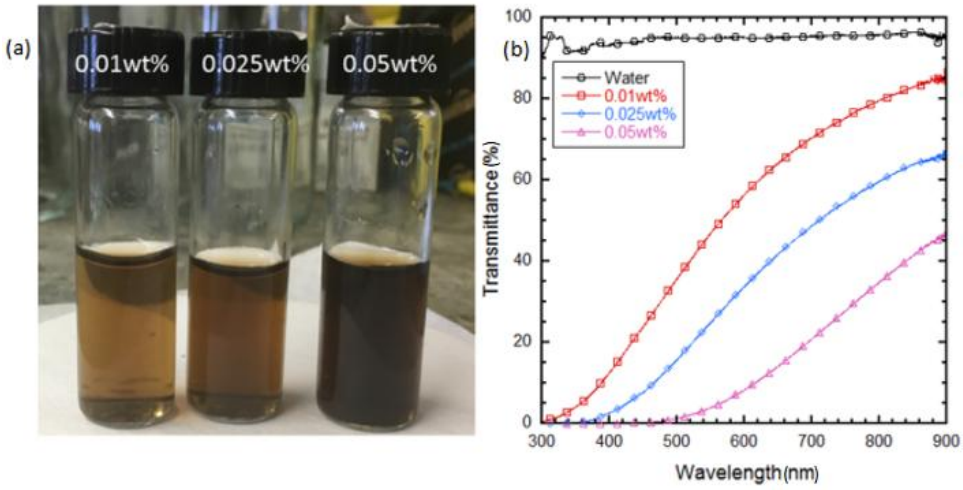

Figure 4-2. (a) Images of GO nanofluids with a weight fraction of 0.01% (left), 0.025% (center), and 0.05% (right). (b) Transmittance as a function of wavelength for as-prepared GO nanofluids with weight fractions of 0.01%, 0.025%, and 0.05%. The transmittance for DI water is also shown for comparison [110].

4.5 Thermal Conductivity Measurement of GO Nanofluids

Figure 4-3 displays the TC enhancement of GO nanofluid as a function of temperature and volume fraction. Compared with pure water, the TC enhancement of nanofluid increases with an increase in both temperature and volume fraction. The largest TC enhancement appears at 90°C and at still less than 5%, caused by the low concentration of GO nanoparticles.

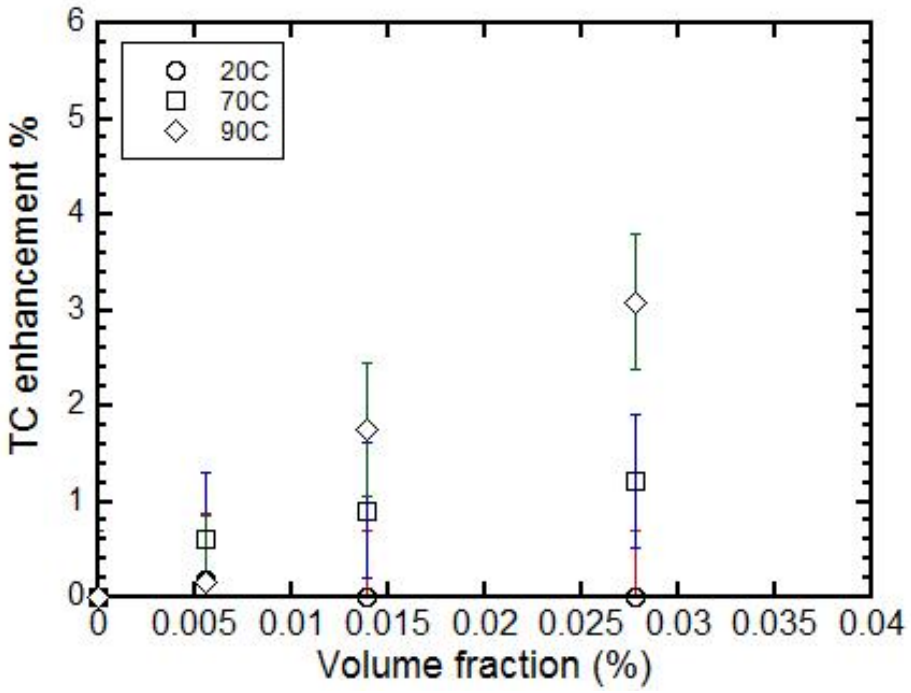

Figure 4-3. Thermal conductivity (TC) enhancement of GO nanofluid as a function of loading and temperature.

4.6 Viscosity Measurement of GO Nanofluids

As shown in Figure 4-4, the relative viscosity of the GO nanofluid increases with the increase in temperature and volume fraction, a similar trend the TC enhancement shown in Figure 4-3. However, the increase in relative viscosity is much greater than the increase in TC enhancement, compared at the same temperature and

volume fraction. For example, the measured viscosity increase is 57% for a 0.014 vol.% GO loading at 90°C, compared to a 1.76% increase in thermal conductivity.

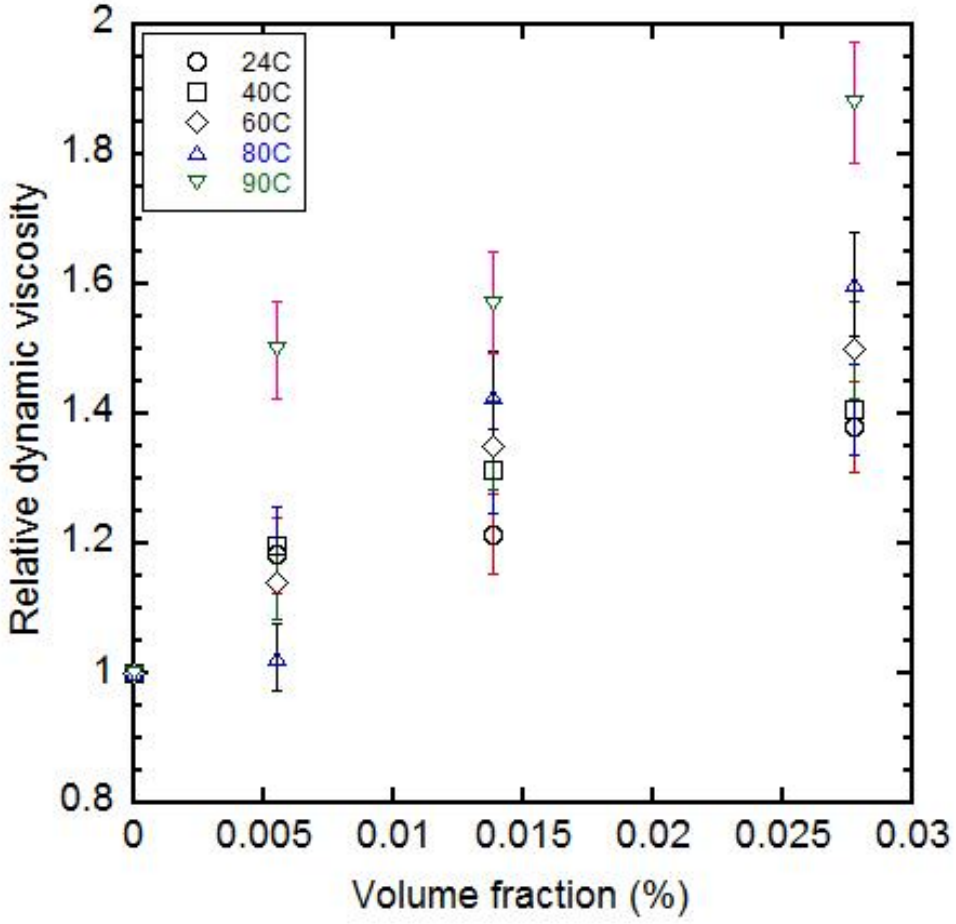

Figure 4-4. Relative dynamic viscosity of the GO nanofluid as a function of loading and temperature.

4.7 Atomic Ratio of GO Nanoparticles Adjusted by UV Reduction

To further enhance the optical property of GO nanofluids without increasing particle concentration, UV reduction is applied to adjust the atomic ratio ([C]/[O]) of GO nanoparticles. As seen in Figure 4-5, the appearance of GO nanofluids became darker as the exposure time increased, and most particles settled down after being exposed to UV light for 1 h. The transmittance was further compared between the samples. As seen in Figure 4-6, the transmittance dropped very quickly as exposure

time increased, indicating that a certain level of reduction was reached by controlling the exposure time. We notice that after 1 h exposure, the nanofluids turned almost transparent, with most particles settled down, indicating the deterioration of nanofluid stability caused by over reduction.

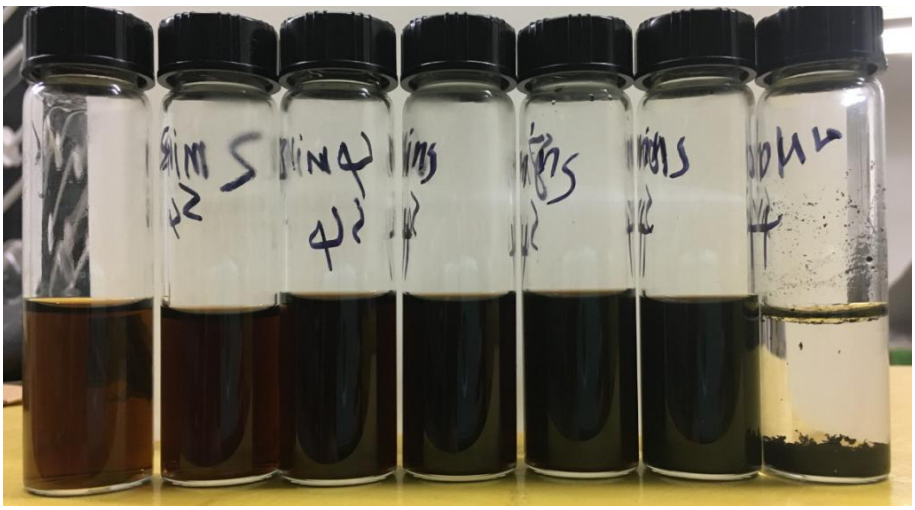

Figure 4-5. GO Nanofluid Samples Exposed to UV Irradiation for 0, 2 min, 4 min, 6 min, 8 min, 10 min, and 1 h (from left to right).

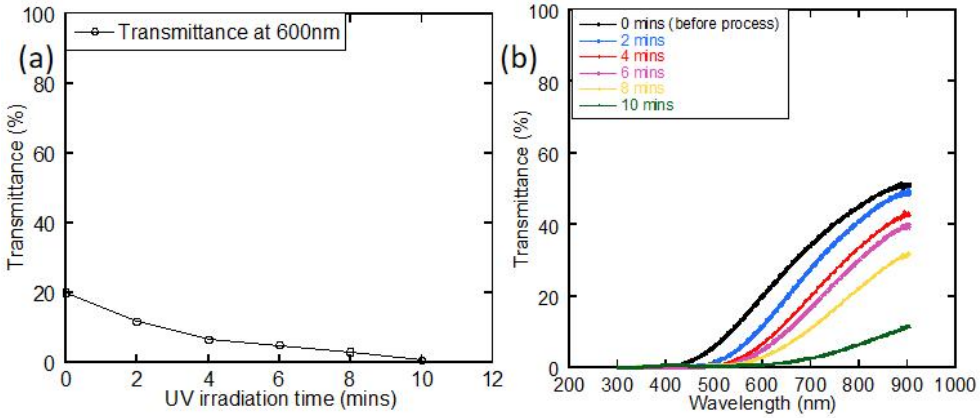

Figure 4-6. (a) Transmittance at 600 nm as a function of UV irradiation time for the GO nanofluids at room temperature. (b) Transmittance spectra of the GO nanofluids after 0, 2 min, 4 min, 6 min, 8 min, and 10 min at room temperature.

Such a result indicates that the optical property of GO nanofluids could be enhanced by increasing the [C]/[O] ratio. However, GO nanoparticles can no longer remain stable in water if the [C]/[O] ratio is too high. The atomic ratio of GO nanoparticles should be controlled at a certain level that can maximize the solar absorptivity of GO nanoparticles without causing too much damage to fluid stability. Such control can be performed by limiting the UV exposure time of GO nanofluids. However, the stability of different GO samples is not yet fully revealed, especially when served at working conditions (boiling at around 100°C). After further testing of GO nanofluid stability at working conditions, a balance between solar absorptivity and fluid stability can be reached. And the exact atomic ratio of GO nanoparticles will be analyzed with XPS spectra.

4.8 Accelerated Stability Test With Centrifugal Force

The stability test of GO nonfluids was first conducted at room temperature for over 30 days. The transmittance at 600 nm of the GO nanofluids as a function of storage time is shown in Figure 4-7(a). The transmittance varies by less than 4% throughout this 30-day test. According to the Beer-Lambert law, the transmittance of the GO nanofluids would increase if the GO particles were to precipitate. This indicates that GO nanofluids can remain stable for quite a long time when stored at room temperature, and similar results were also reported by other researchers [77]. The stability of the GO nanofluids was also assessed by an accelerated stability test. Accelerated stability testing is a common approach to predicting long-term performance [148], [149], [150], [151], [152]. A typical method to conduct such tests is to centrifuge samples at a certain relative centrifugal force and temperature at various times [153], [154], [155], [156], and it is aimed at studying the influence

brought to stability by long-term storage. Due to the density difference between water and GO nanoparticles, over the long term sedimentation will occur as a result of gravity. The determining factor can be ascribed in terms of the sedimentation velocity, and Stokes' law is a formula for determining the rate of sedimentation. It states that a particle moving through a viscous liquid attains a constant velocity or sedimentation rate. The sedimentation velocity is described as follows:

$$V_s = \frac{Gd^2(\rho_p - \rho)}{18\eta}, \quad (7)$$

where V_s is the sedimentation velocity, G is the local gravitational acceleration, d is the particle diameter, ρ_p is the density of the particle, ρ is the density of the fluid, and η is the fluid viscosity.

In this work, accelerated stability testing is performed with a centrifuge at 1500 rpm and 90°C, equivalent to 630 g force. For practical reasons, GO nanofluid boiling cannot be performed during centrifugation, so the testing temperature was set as high as possible: 90°C instead of 100°C in this test to avoid boiling. The centrifugal force applied in the test is to simulate the long-term influence of gravitational force. According to Equation (7), 3 h centrifugation under 630 g force could be used to predict the influence brought on particle sedimentation by 1890 h storage, which is around 79 days. As seen in Figure 4-7(b), the transmittance of the GO nanofluids decreases by less than 6% after 3 h centrifugation at 90°C. Such results indicate that GO nanofluids are quite stable under both room-temperature storage and high-temperature storage. The accelerated stability test further confirms that the sedimentation effect generated by gravity is quite small, even over the long term. The bulky presence of oxygen-containing functional groups on the surfaces of GO nanoparticles makes them hydrophilic and stable in water.

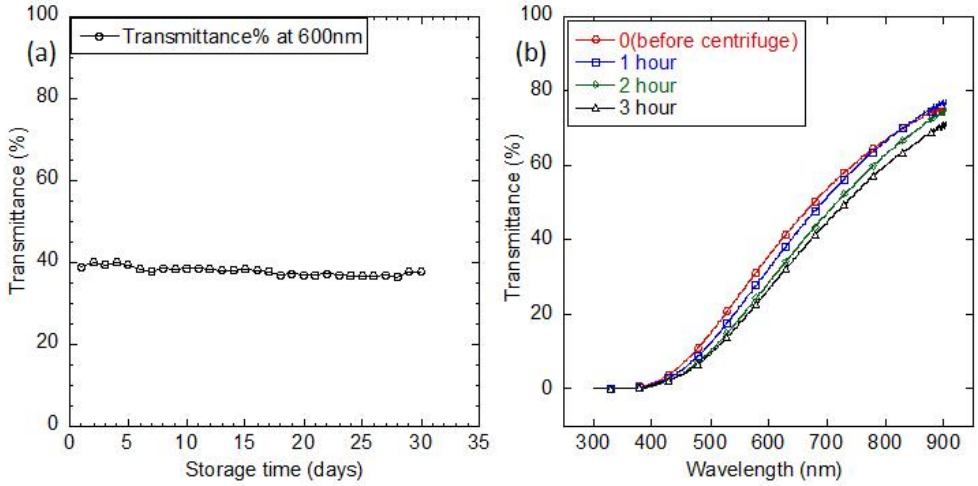

Figure 4-7. (a) Transmittance at 600 nm as a function of storage time for the GO nanofluids at room temperature. (b) Transmittance spectra of the GO nanofluids after 1 h, 2 h, and 3 h centrifugation at 90°C [110].

Due to the limitations of the experimental apparatus, the accelerated stability test cannot be performed under boiling conditions or over 100°C. The accelerated stability test can be used to predict sedimentation caused by gravitational force over the long term. However, particle agglomeration is another important factor leading to sedimentation, and it is dominated by Van der Waals attracting force and other repulsive forces between particles rather than gravitational force. The accelerated stability test under centrifugal force cannot simulate particle collisions over the long term. Stability tests over boiling temperatures are therefore necessary for the evaluation of the stability of GO nanofluids.

4.9 Sealed Tube Test Without Boiling

Many researchers have affirmed that the major thermal degradation of GO particles usually occurs after 200°C, and the weight loss is due to the decomposition of oxygen-containing functional groups after 200°C [157], [158], [159], [160], [161]. Gao et al. [148] found that GO cannot be reduced into pristine graphene by thermal

annealing if the temperature is lower than 1700°C, the thermal decomposition temperature of carbonyl. However, few papers have discussed GO degradation when prepared in water as nanofluids. The degradation behavior of GO nanoparticles in water may vary. A sealed tube test was performed with GO nanofluids kept at 120°C, the proposed working temperature of GO nanofluids in two-phase thermosyphon, and the experiment lasted for 9 days. As seen in Figure 4-8, the appearance darkens after a day of testing, signaling the thermal reduction of GO. Little agglomeration was observed during this 9-day test. The transmittance of the nanofluid was also measured after each cycle, and the results are shown in Figure 4-9. The transmittance of the prepared GO nanofluids dropped significantly in the first 2 days and remained very low for the rest of the 7 days. As reported in Niu et al. [83] and other papers related to GO thermal reduction, GO particles cannot be fully reduced into pristine graphene, as only partial reduction would happen to GO nanofluid when heated at 120°C. The hydrophilicity of reduced GO has decreased, but it is still enough to form stable nanofluids without boiling.

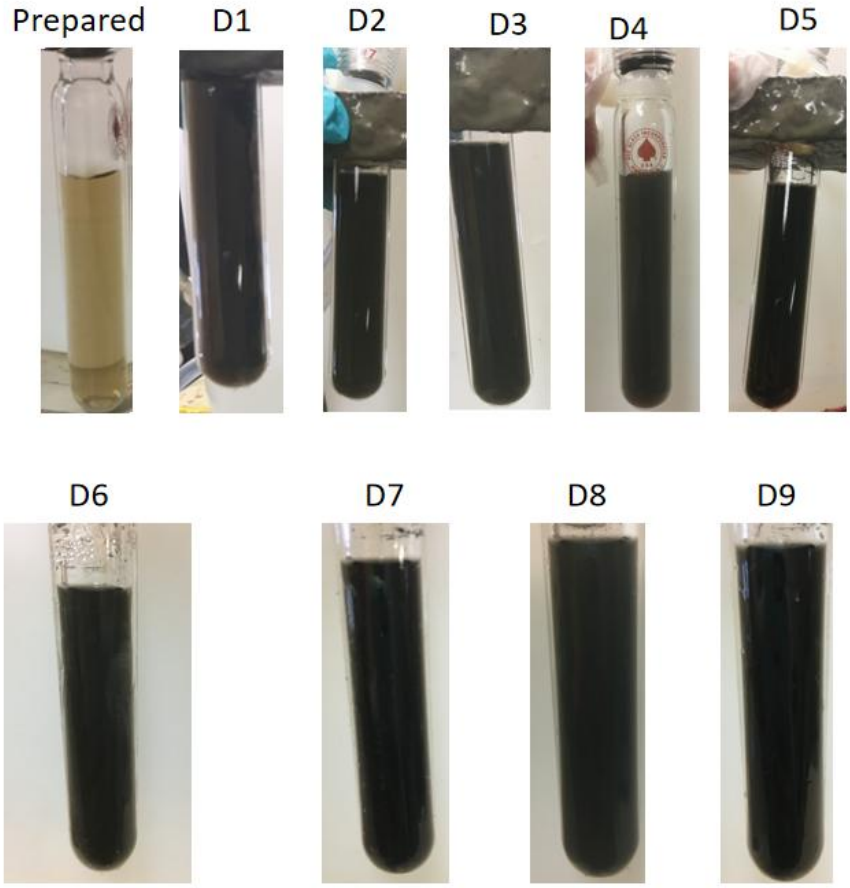

Figure 4-8. Images of the GO nanofluids in a sealed tube for different heating time (From as prepared to 9 days).

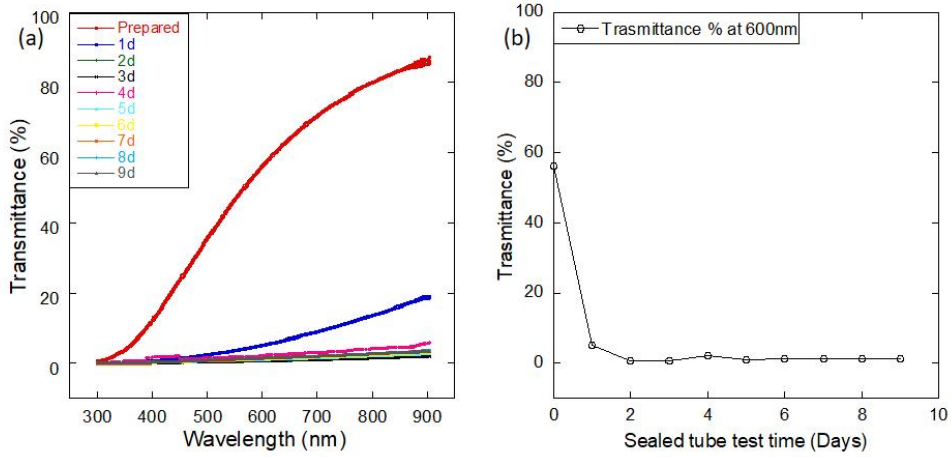

Figure 4-9. (a) Transmittance spectra of the GO nanofluids for different sealed-tube testing times. (b) Transmittance at 600 nm of the GO nanofluids as a function of sealed-tube testing time.

The thermal degradation behavior of GO nanoparticles varies between powders and nanofluids. GO nanofluids showed an extremely small transmittance change during the accelerated stability test at 90°C, and a significant transmittance drop was observed after the sealed-tube test at 120°C. Therefore, the thermal degradation may take place at around 100°C. A similar observation is also reported by Niu et al. [83], stating that thermal degradation of GO nanofluids may occur after 120°C. Niu et al. [83] reported that significant thermal degradation of GO nanofluids was observed only after 180°C. The reported test was conducted without sample boiling, while boiling and condensation are inevitable for GO nanofluids when served as working fluids in a two-phase thermosyphon. So far, GO nanofluids seem to be a strong candidate due to their reportedly excellent optical properties and stability. However, the boiling effect on GO nonfluids has not been thoroughly studied. Thus, it is necessary to extend the results from the few relevant studies that exist by conducting stability tests with boiling and condensation processes involved.

4.10 Boiling and Condensation Stability Test

GO nanofluids remain stable in both the centrifugal test and the sealed tube test without boiling. However, few papers have discussed the influence of the boiling-condensation process on GO nanofluids. Rapid local concentration change is introduced to the nanofluid when the sample is boiled, especially where bubbles form. Molecule interaction between GO particles would then be significantly enhanced, necessitating further investigation on the stability needed for GO nanofluid in boiling conditions. GO nanofluids were first tested for 6 days in the boiling-condensation experiment. As seen from Figures 4-10(a) and 4-10(b), the GO nanofluids darken considerably after the boiling and condensation tests. Nevertheless, GO particle

precipitation can be visually spotted after centrifugation, indicating the stability deterioration that arises from the boiling and condensation processes, as shown in Figures 4-10(c) and 4-10(d). The transmittance change is also tracked during the process. Figure 4-11 presents the transmittance of GO nanofluids decreasing during the first day of the boiling and condensation process and then remaining constant for the rest of the 5-day test.

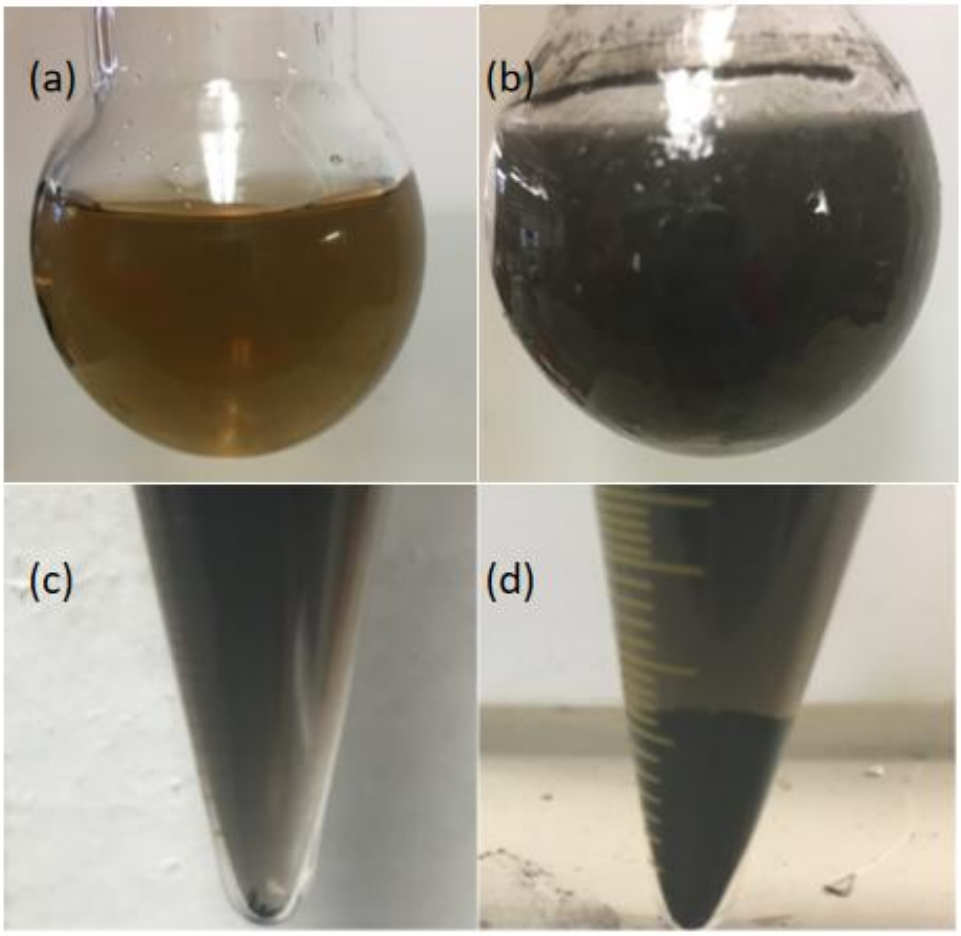

Figure 4-10. Images of the GO nanofluids in a boiling flask (a) Before and (B) After boiling and condensation tests. Images of the after-test GO nanofluids in a test tube (c) before and (d) after centrifugation at room temperature [110].

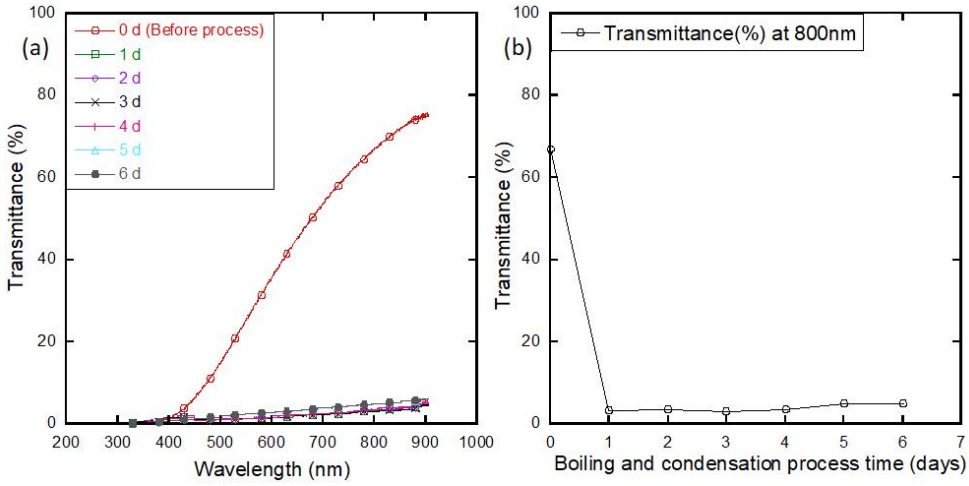

Figure 4-11. (a) Transmittance spectra of the GO nanofluids for different boiling and condensation processes. (b) Transmittance at 800 nm of the GO nanofluids as a function of boiling and condensation process time [110].

The transmittance pattern of GO nanofluids after boiling and condensation tests is similar to the result of the sealed tube test. The transmittance decreased fast after the first-day test and stayed constant for the remaining days of the test. GO nanofluids prepared with the same method were used to remain homogeneous after 3 h centrifugation. For GO nanofluids after boiling and condensation tests, however, precipitation was visible after centrifugation. Particle precipitation signals stability deterioration and is usually caused by overreduction, as we observed during the UV reduction test. Therefore, further degradation mechanism studies and GO particle characterization are necessary before further conclusions are drawn.

4.11 Degradation Mechanism Study of GO Nanofluids.

Depending on the type of reduction that occurs, different oxygen-contained functional groups can be removed from the graphitic structure. A study by Guex et al. [162] determined that both hydroxyl and epoxy groups are reduced using sodium borohydride, while carbonyl and carboxyl groups do not reduce with this method.

This study used high-resolution XPS spectra for GO and rGO nanofluids. The carbon 1s spectrum of all reduced GO samples exhibited a shift from the double peak seen for pristine GO to the single sharp peak toward low binding energies, demonstrating a trend to restore the sp^2 bonding graphene configuration. In other words, the basal plane oxygen-containing functional groups were removed. There was also a decrease in intensity for the peaks associated with the oxidized carbon, from 45.65% in GO to 11.5% in rGO. This reduction occurs within the first 8 min of exposure, leading to the reduction of hydroxyl, epoxy, and even hydroxyl groups associated with carboxylic acid groups. These spectra can be found in Figure 4-12.

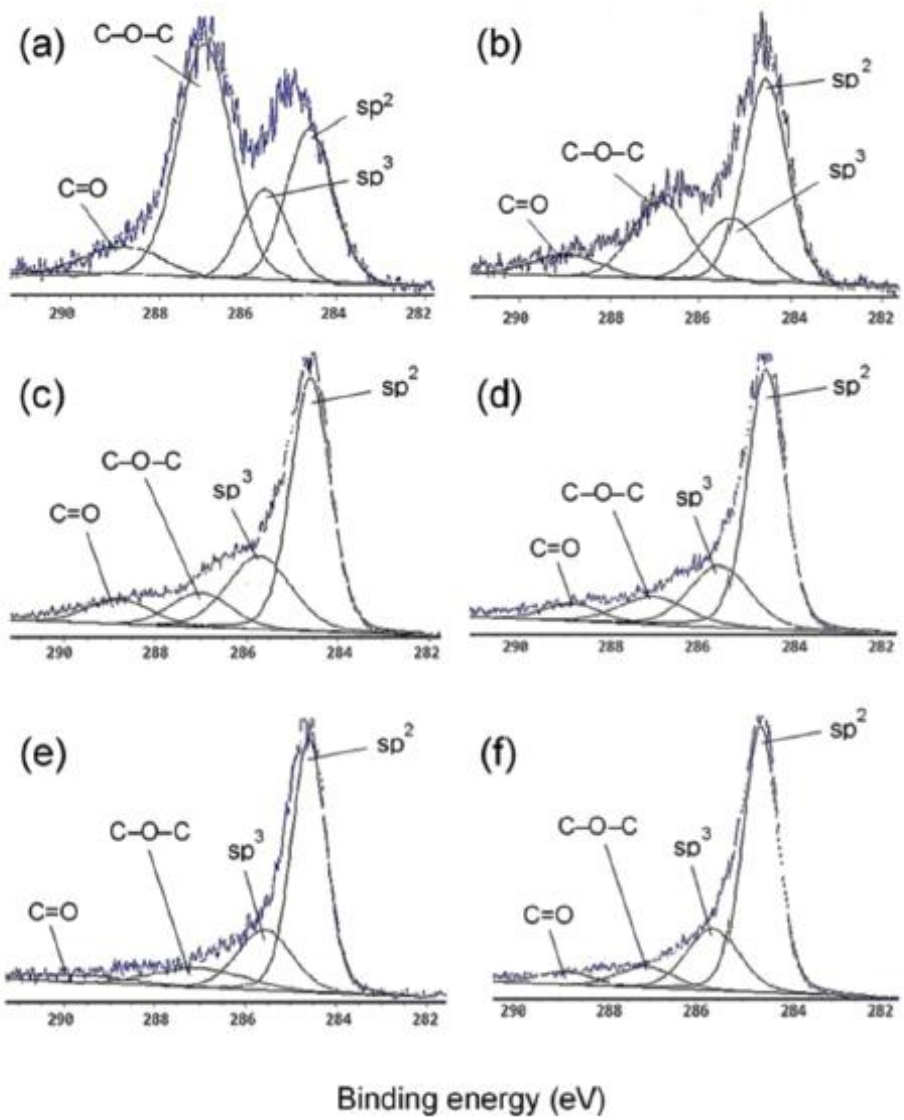

Figure 4-12. XPS data for reduction of GO Using Sodium Borohydride [162].

Gao et al. further developed this mechanistic insight to examine the basal and planar regions of GO [148]. Initial thermodynamic analysis revealed that hydroxyl groups found in the interior aromatic domain are unstable at room temperature and are subject to dissociation due to a negative Gibbs free energy (ΔG). Hydroxyl groups found at the edge are stable due to a positive ΔG, but can reduce at high temperatures (700°C). Decarbonization will not occur spontaneously at low or high temperatures (positive ΔG across all temperatures). Carboxyl groups are expected to reduce slowly at temperatures between 100°C–150°C. For thermal decarboxylation, an increase in temperature reduces ΔG without increasing the reaction energy barrier. As such, thermal decarboxylation is facilitated at higher temperatures. Notably, thermal reduction was applied at 700°C–1200°C, much hotter than our testing at 110°C–120°C. Thermodynamically, however, this study notes that decarboxylation should occur slowly near this temperature range. This study further proposes several possible mechanisms for the thermal reduction of GO. These reaction mechanisms can be seen in Figure 4-13.

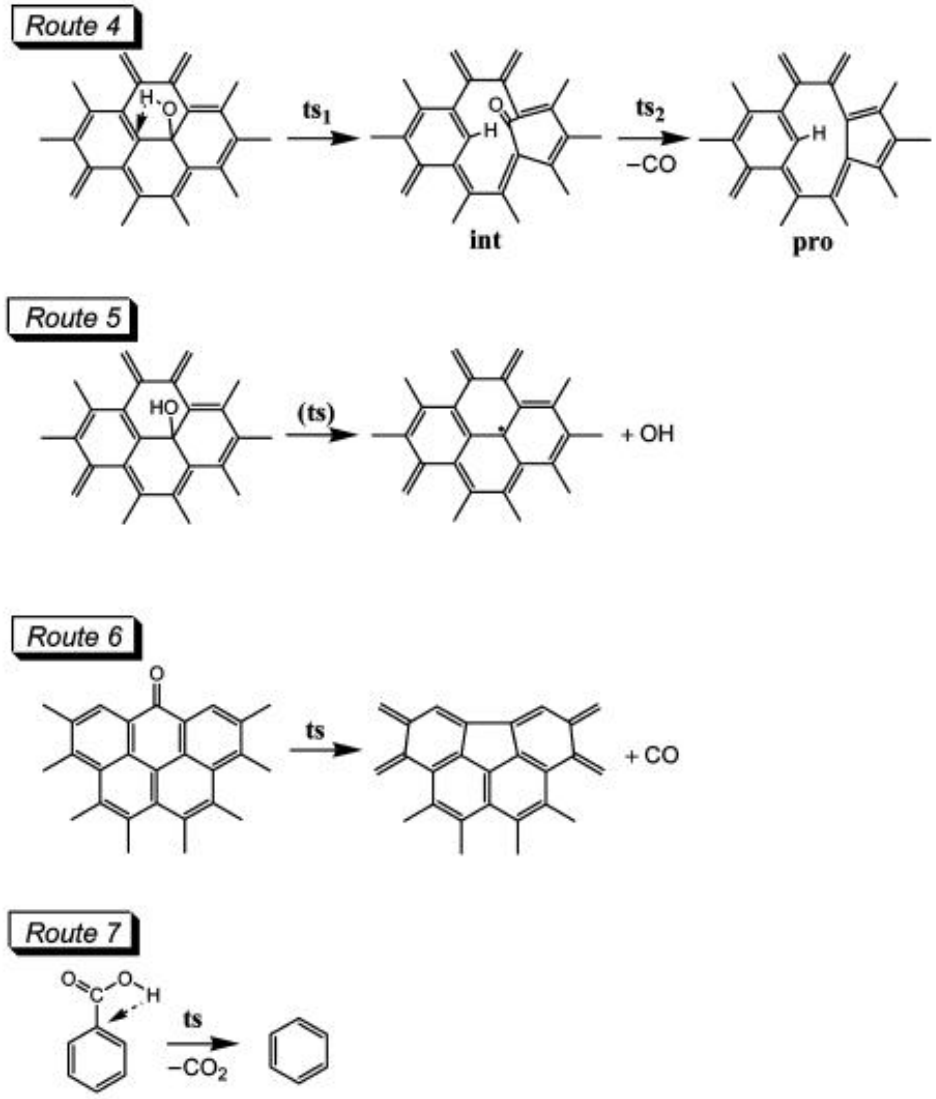

Figure 4-13. Routes 4 and 5 refer to the mechanism for the thermal de-hydroxylation of GO. Routes 6 and 7, respectively, show the mechanisms for thermal de-carbonylation and thermal de-carboxylation of GO [148].

Investigating the removal of functional groups in thermal reduction in our GO nanofluids, this sections details the results of atomic ratio analysis by XPS, functional group study by FT-IR, and morphology characterization of GO nanoparticles.

4.12 XPS Spectra Analysis

Atomic ratio analysis is carried out by XPS to determine the [C]/[O] ratio before and after the boiling and condensation tests, and the spectra of the GO nanoparticles before and after the boiling and condensation tests are shown in Figures 4-14(a) and 4-14(b), respectively. The presence of oxygen and carbon can be identified in both spectra. As determined from the XPS spectra, the atomic ratio of the GO nanoparticles was 70.7% C/29.3% O before the boiling and condensation tests. However, their atomic ratio becomes 79.9% C/20.1% O after the boiling and condensation tests. The corresponding [C]/[O] ratio increases from 2.4 to 3.9, and this result indicates that GO particles lost part of their oxygen-containing functional groups due to the boiling and condensation processes. The [C]/[O] ratio increase signals GO reduction, consistent with the nanofluid appearance change before and after the boiling and condensation tests.

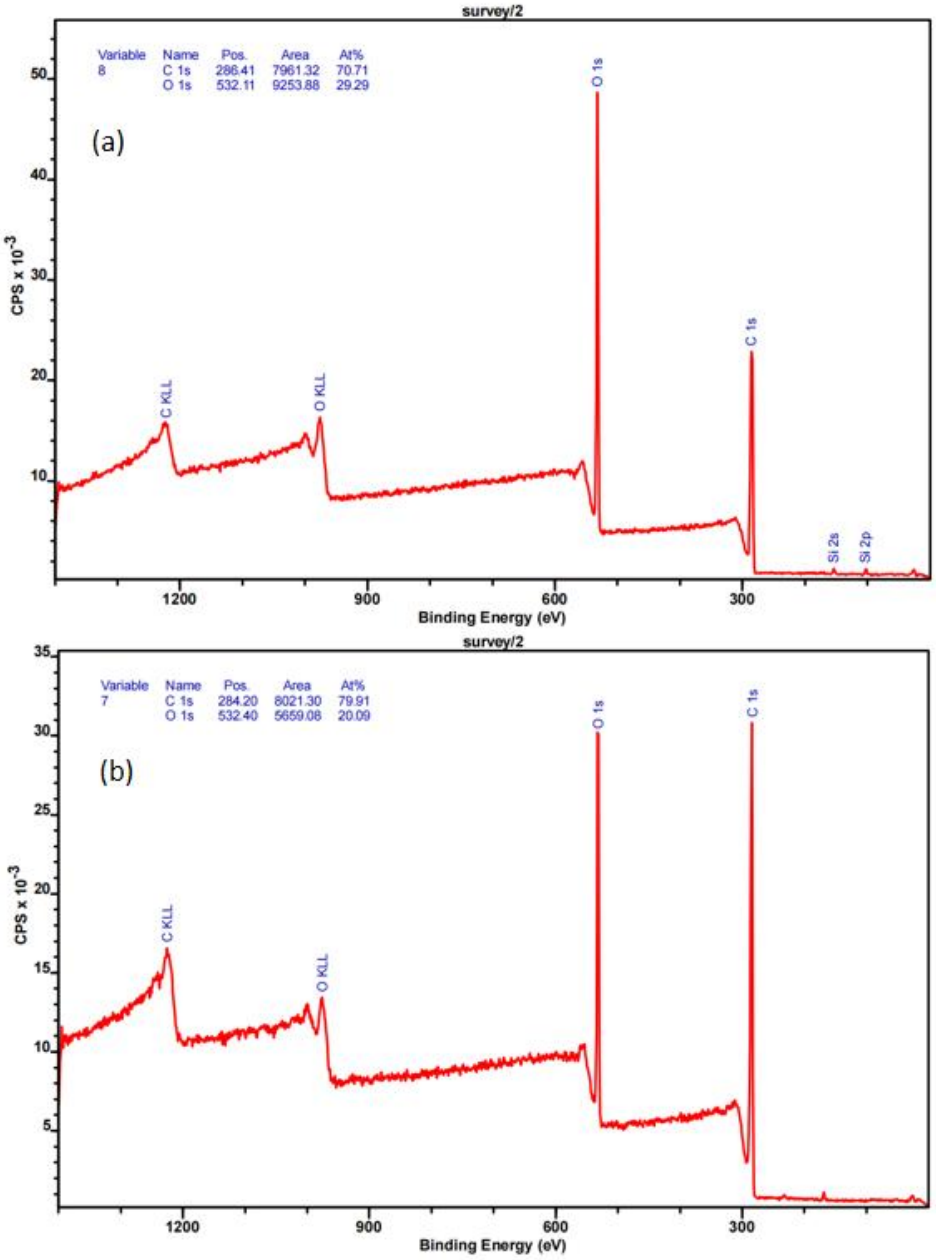

Figure 4-14. XPS spectra of the GO nanofluids (a) Before and (b) After the boiling and condensation processes [110].

4.13 FT-IR Spectra Analysis

FT-IR spectra analysis is carried out to further determine which parts of oxygen-containing functional groups are lost during the boiling and condensation tests. The FT-IR spectra of GO nanofluids were measured before and after a full-day

boiling and condensation test. As seen in Figure 4-15, the FT-IR spectra of GO particles before the boiling and condensation experiment show many features related to oxygen-containing functional groups. The broad peak at around 3400 cm^{-1} is related to hydroxyl groups. The peaks at 1700, 1600, and 1050 cm^{-1} are related to the stretching of carboxylic acid groups, the remaining sp^2 carbon groups after oxidation, and alkoxy groups, respectively. However, most of the signals mentioned above significantly decreased in the FT-IR spectra of GO particles after a day of boiling and condensation experiments. This result indicates that the GO particle underwent thermal reduction during the boiling and condensation processes and lost part of its oxygen-containing functional groups.

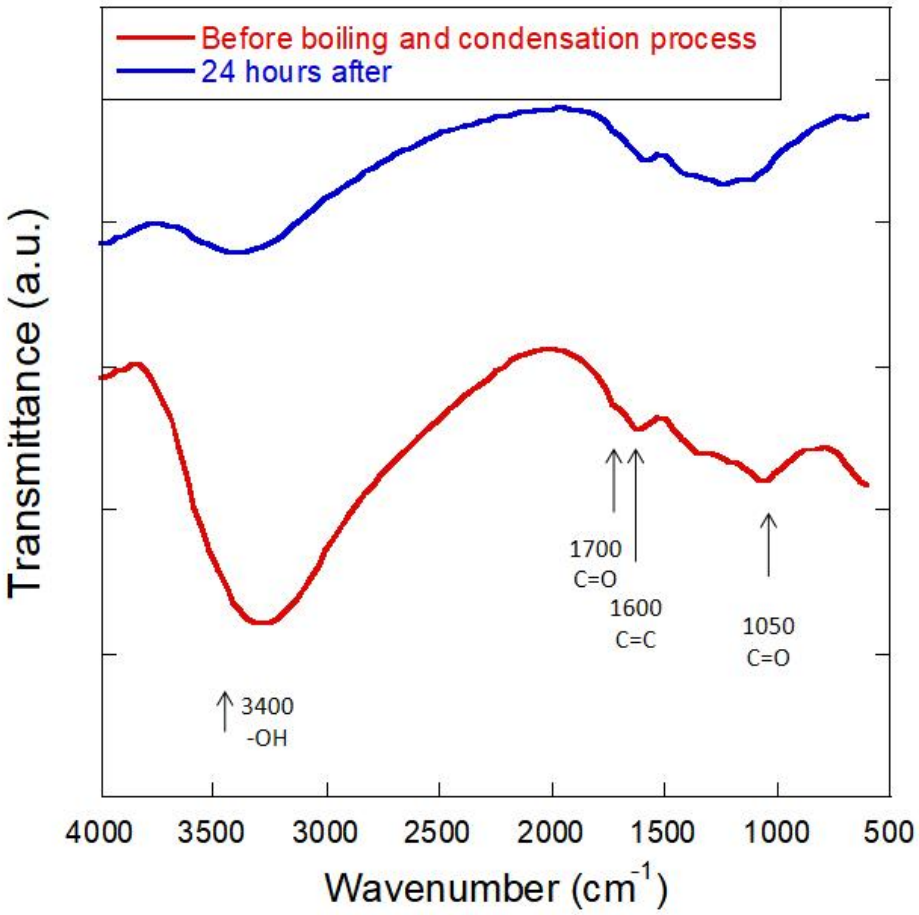

Figure 4-15. FT-IR spectra of the graphene nanofluids (a) Before and (b) After the boiling and condensation processes [110].

Thermal reduction of GO nanoparticles is widely reported to occur at relatively high temperatures [83], [130], [148], [157]. Most oxygen-containing functional groups are reported to remain stable below 150°C, except carboxyl groups, which reportedly decompose slowly at temperatures between 100°C and 150°C [163]. However, by comparing the FT-IR spectra before and after the experiment, de-carboxylation and de-hydroxylation are most likely to occur at around 100°C during the boiling and condensation processes, as their signal peaks significantly decreased after the experiment. Decarbonization is less likely to occur at such a temperature.

4.14 Particle Size and Morphology Characterization of GO Nanoparticles

The TEM image of a GO particle is shown in Figure 4-16(a). The GO particle lies on the lacey carbon film. The GO particles have a sheet-like shape with an average size of 1–3 μm. However, due to the agglomeration of GO particles caused by the boiling and condensation processes. Particles settled down shortly after the boiling and condensation tests, with small flakes visible in the fluid. Since the GO nanoparticles were hard to separate from each other after the boiling and condensation tests, we performed SEM measurements on the GO sample. As seen in Figure 4-16(b), severe GO particle overlap could be directly observed for the sample after the experiment, and it is hard to measure the size of the GO particle due to severe particle agglomeration.

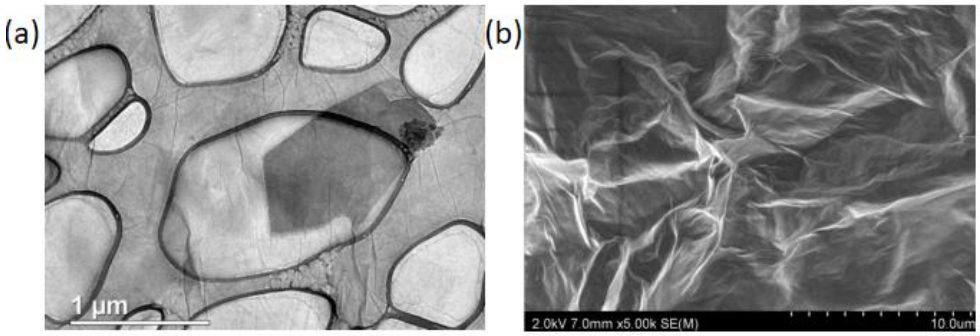

Figure 4-16. (a) TEM image of a GO nanoparticle before the boiling and condensation experiments. (b) SEM image of GO nanoparticles after the boiling and condensation experiments [110].

4.15 Summary

GO nanofluids were prepared and modified by UV reduction. The transmittance of GO nanofluids is much lower than that of pure water, and it decreases as the concentration of GO particles increases. Ergo, GO nanofluids are far more absorptive than pure water, and such optical properties could be further enhanced by increasing GO particle concentration. When compared with pure water, both the TC enhancement and relative viscosity increase with an increase in temperature and volume fraction. However, when compared at the same temperature and volume fraction (e.g., for 0.014 vol.% GO loading at 90°C), the increase found in relative viscosity is around 57%, while it is only 1.76% for the TC enhancement. Higher viscosity could prevent fluid motion, usually considered a less favored specification for thermosyphon's working fluid [163]. Therefore, it is necessary to find other methods to enhance solar absorptivity rather than simply increasing particle concentration. UV reduction could significantly enhance the solar absorptivity of GO nanofluids without increasing GO particle concentration, and the enhancement found in solar absorptivity increased with the increase in UV exposure time. There is also a trade-off from decreased hydrophilicity induced by increased UV exposure time. Such a trade-off restricts the optical performance of GO nanofluids.

The stability of GO nanofluids was tested under various working conditions and evaluated by comparing transmittance before and after each test. GO nanofluids remained stable at room temperature for over 30 days, and the transmittance remained

nearly unchanged over the entire storage time. It also showed a less than 6% decrease in transmittance after centrifugation at 90°C for 3 h. No obvious stability deterioration was observed for these two tests. GO nanofluids were then tested in sealed tubes at 120°C without boiling for 9 days. The transmittance of GO nanofluids was found to decrease significantly on the first day and then remain constant at a very low level for the rest of the test. Such observations indicated that possible GO reduction may occur during the sealed-tube test, and the GO nanofluids remained stable after the reduction. GO nanofluids were further tested under boiling and condensation processes. A similar GO reduction was found as the transmittance decreased significantly after the test. However, stability deterioration of GO nanofluids was also observed after the boiling and condensation tests, as GO nanoparticles settled down quickly after centrifugation.

After the analysis of the structure of the GO nanoparticle and review of all possible reduction reactions that could occur on the surface of the GO nanoparticle, carboxyl groups and hydroxyl groups were easier to remove from the GO surface when compared with epoxyl groups and carbonyl groups due to their relative low energy barriers [148]. Morphology characterization by TEM and SEM confirmed that original GO nanoparticles had an average size of 1–3 μm, and severe particle agglomeration was observed after the boiling and condensation experiment. XPS spectra analysis confirmed that the [C]/[O] ratio increased from 2.4 to 3.9 after the boiling and condensation tests, directly evidencing GO reduction. By observing significant peak intensity drops at 3400 cm^{-1}, 1700 cm^{-1}, and 1050 cm^{-1}, FT-IR spectra analysis further confirmed that GO reduction was induced by both the de-carboxylation and de-hydroxylation reactions.

Charpter 5. Strategies Explored to Enhance Stability of GO Nanofluids

5.1 Introduction

Chapter 4 revealed GO nanofluids remained stable during long-term storage at room temperature and in sealed tubes. However, severe GO degradation and particle agglomeration were observed and confirmed after the boiling and condensation tests. Multiple methods by which to mitigate the stability-deterioration issue are now explored, including pH control and the functionalization of GO nanoparticles with surfactants and cellulose nanofiber. Each method is detailed below.

5.2 Materials

GO nanoparticles were purchased from Graphene Laboratories Inc. (Ronkonkoma, NY, USA). Hydrochloric acid (HCl), Sodium hydroxide (NaOH), Monosodium phosphate (NaH_2PO_4), Disodium phosphate (Na_2HPO_4), IGEPAL® CO-520, IGEPAL® CO-630, IGEPAL® CO-720 were purchased from Sigma-Aldrich. TEMPO-oxidized cellulose nanofiber was purchased from the University of Maine.

5.3 PH Control

The surface charge of nanoparticles is an important factor in dispersing nanoparticles. Zeta potential is an indicator of the surface charge of nanoparticles. It is accepted that absolute zeta potential values over 30 mV are enough to form stable dispersion, whereas nanoparticles with absolute zeta potential values less than 30 mV are considered unstable [164], [165], [166]. As mentioned in many nanofluid experiments, the stability of an electrostatically stabilized dispersion is highly

dependent on pH [167], [168], [169], and the results showed that the stability of prepared fluids increased as the pH value increased. This is because adjusting the pH value of fluids will lead to either a smaller or larger surface charge of nanoparticles, further altering the repulsive force between nanoparticles [170]. Particle agglomeration will occur when the repulsive force is smaller than the Van der Waals attractive force, according to the DLVO theory. Konkena et al. [171] investigated the relationship between zeta potential and pH of both GO and rGO nanofluids. As shown in Figure 5-1, when pH was lower than 10, the zeta potential of both GO and rGO decreased as pH increased, so a more electrostatically stable nanofluid was formed. GO nanoparticles were also more stable in water than rGO nanoparticles, as they showed much lower zeta potential when compared at the same pH value. The ionization of the carboxylic groups is primarily responsible for the buildup of charge on the graphene surfaces, contributing to the repulsive forces between nanoparticles. Therefore, pH control influences the stability of rGO nanofluids less than GO nanofluids do, because of the lack of carboxyl groups on the surface of rGO nanoparticles.

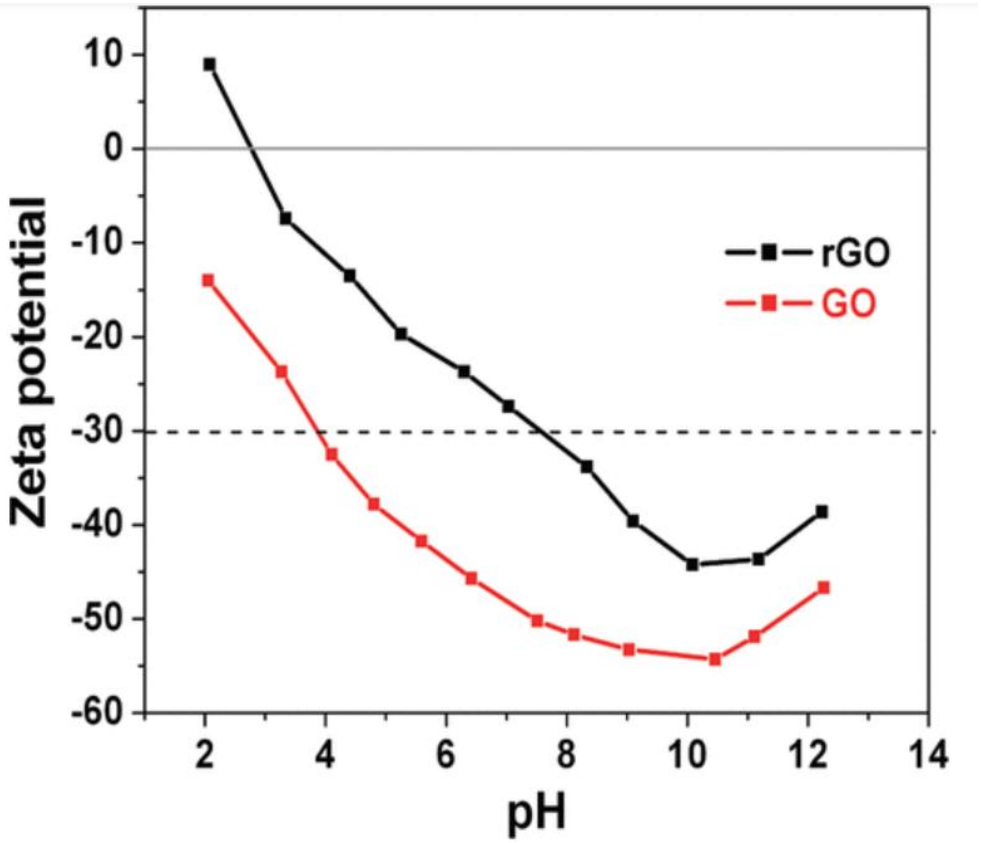

Figure 5-1. Zeta potential of GO and rGO nanofluids as a function of pH [171].

Relatively stable GO nanofluids could be prepared when the pH level was between 4 and 11.5. Considering the GO reduction caused by the boiling and condensation processes, the pH level should be adjusted to between 8 and 11 to retain fluid stability. However, different GO nanoparticles may possess different portions of carboxyl groups, which could directly influence the stability enhancement of pH control. GO nanofluids with different pH levels were therefore prepared and tested.

An extreme pH condition (pH = 2.4, pH = 12.5) was first tested by adding strong acids and alkalines (HCl and NaOH). As seen in Figure 5-2, GO particles started to aggregate quickly when prepared in such extreme conditions. Specifically, GO nanoparticles aggregated quickly in extreme acidic conditions with a pH level lower than 4, and the stability of GO nanofluids also deteriorated quickly when

prepared with a pH value over 12. Such observations align with Konkena et al.'s [171] findings.

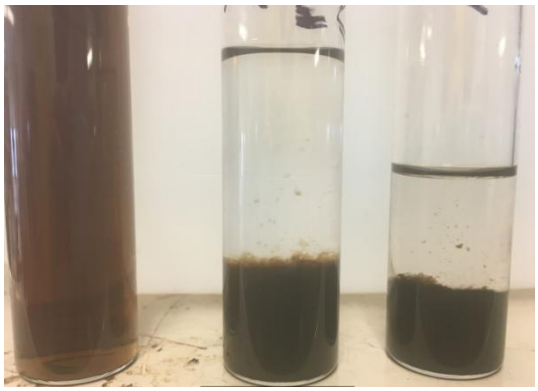

Figure 5-2. From left to right, GO nanofluids prepared with pH = 4.8 (as prepared), pH = 2.4, pH = 12.5.

The pH-adjusted GO nanofluids were then prepared with buffer solution (NaH_2PO_4/ Na_2HPO_4) and sent to the boiling and condensation experiments. As seen in Figure 5-3, when pH was adjusted to 6.2, the GO nanofluids remained visibly stable. The transmittance of GO nanofluids was further measured to evaluate their stability. As seen in Figure 5-4, even though the appearance changed little, the transmittance of GO nanofluids decreased on the first day and then increased as testing time increased. The transmittance decrease on the first day was a signal of GO reduction, and the following increase was probably caused by particle aggregation.

Figure 5-3. From left to right, pH-adjusted GO nanofluids after boiling and condensation experiment for 0 days (as prepared), 1 day, 2 days, and 3 days.

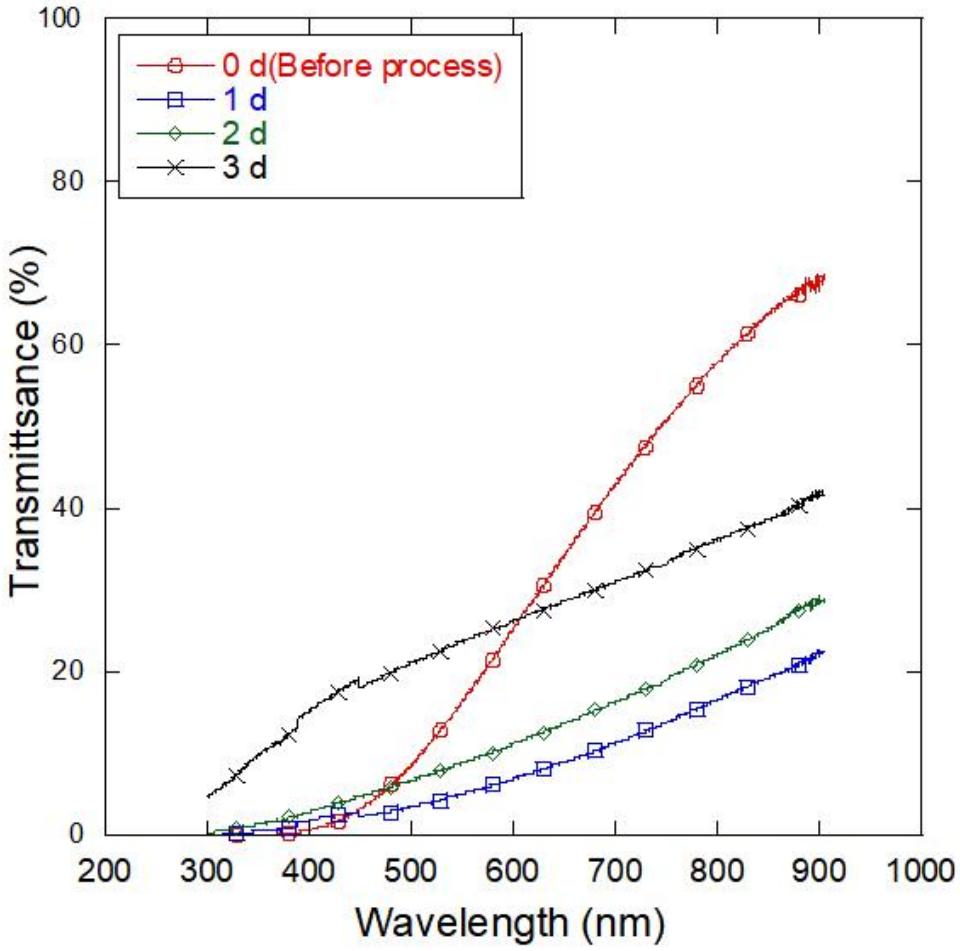

Figure 5-4. Transmittance spectra of pH-adjusted GO nanofluids for different boiling and condensation process Time.

GO nanofluids were then adjusted to a pH value of 8.5 and tested under boiling and condensation processes. As seen in Figure 5-5, GO nanofluids remained stable for the first day without severe agglomeration after tuning the pH from 4.8 (original) to 8.5, but such equilibrium started to break down quickly, and severe particle agglomeration was observed on the second day.

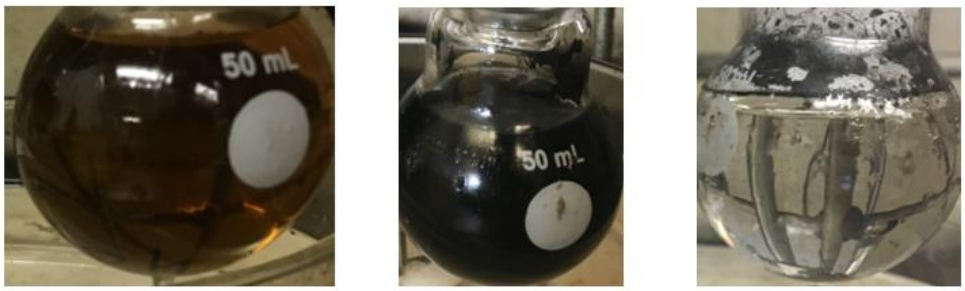

Figure 5-5. From left to right, pH-adjusted GO nanofluids after boiling and condensation experiment for 0 days (as prepared), 1 day, and 2 days.

pH control was widely reported to be an effective method to enhance the stability of nanofluids [56], [164]. However, most papers focus on the stability of nanofluids at room temperature, and few papers have discussed the feasibility of using pH control to enhance the stability of nanofluids under boiling and condensation processes. Our test showed that pH-adjusted GO nanofluids were unstable under boiling and condensation processes. There are two possible reasons for this result:

1. GO reduction, especially de-carboxylation, could take place during the boiling and condensation processes, and pH control has been reported as far less effective after GO nanoparticles underwent de-carboxylation [171].

2. Electric double layer formed around GO nanoparticles could be heavily disrupted when the fluid was boiled. The formation and evolution of bubbles around the surface of GO nanoparticles could disrupt the original distribution of ions and counterions.

5.4 Functionalization with Surfactant

Another method developed to address the aggregation problem was functionalizing the GO nanoparticles with surfactant. The existence of surfactant could significantly contribute to the steric repulsive force, preventing the aggregation of GO nanoparticles. A more stable nanofluid can be formed by isolating the GO particles with surfactant molecules. As water was used as a continuous phase in this work, surfactant with a relatively higher HLB value (e.g., IGEPAL® CO-630) was selected and tested in the boiling and condensation experiments. The chemical structure of IGEPAL® CO-630 is shown in Figure 5-6. The testing results are shown

below in Figures 5-7 and 5-8. With the GO particles functionalized with surfactant, stability deterioration slowed slightly, as evidenced by the appearance of the nanofluids over the first 4 days. However, the slowly increased transmittance indicated that the deterioration of GO nanofluids was not completely prevented. The prepared GO nanofluids were still slowly degrading, as the processing time increased.

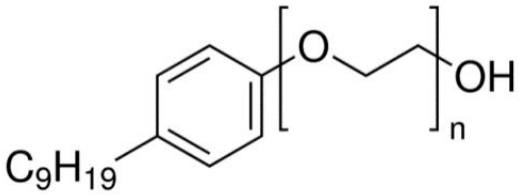

Figure 5-6. Chemical structure of IGEPAL® CO-630, *n* = 9~10, HLB = 12 [172].

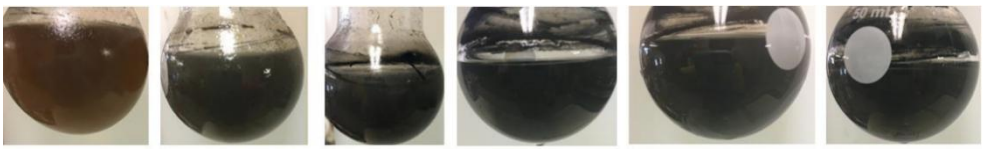

Figure 5-7. From left to right, GO nanofluids functionalized with IGEPAL® CO-630 after boiling and condensation experiment for 0 days (as prepared), 1 day, 2 days, 3 days, 4 days, and 5 days.

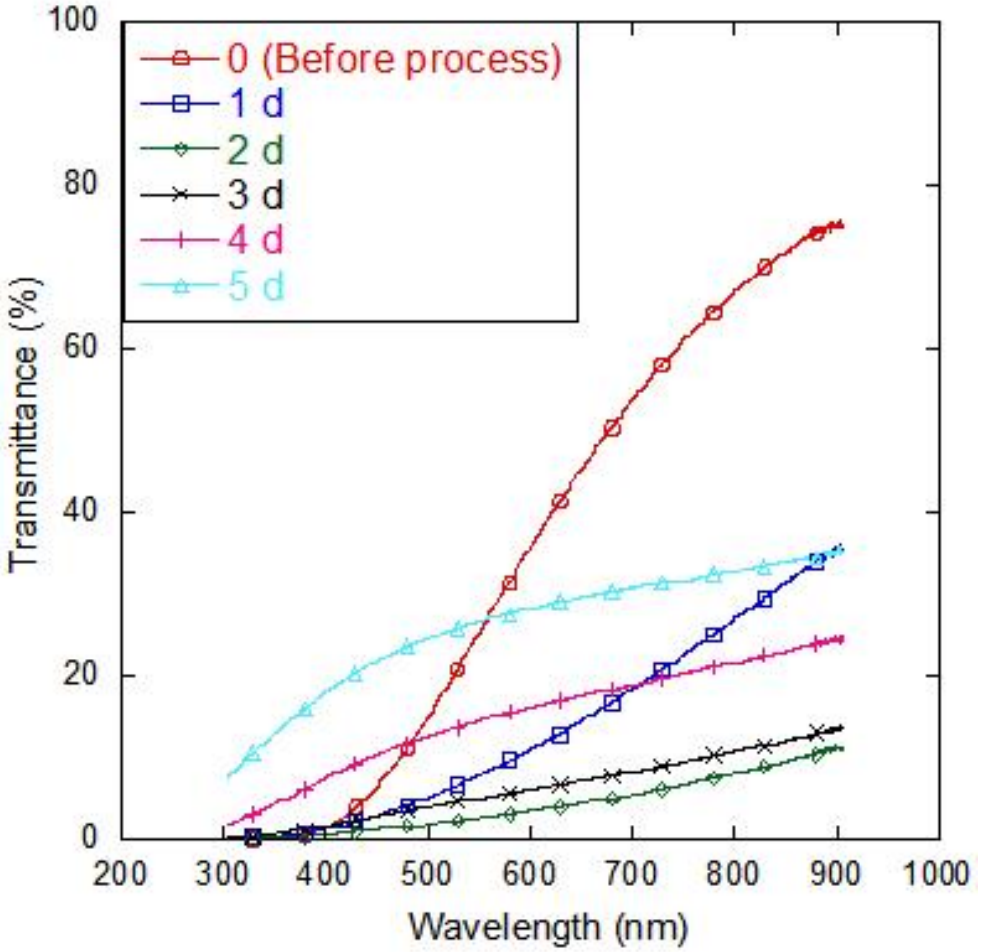

Figure 5-8. Transmittance spectra of the GO/IGEPAL® CO-630 nanofluids for different boiling and condensation process time.

Other surfactants, such as IGEPAL® CO-520 and IGEPAL® CO-720, were also tested. The chemical structures of IGEPAL® CO-520 and IGEPAL® CO-720 are shown in Figure 5-9(a) and (b), respectively. As water was used as the base fluid when preparing GO nanofluids, a more hydrophilic surfactant was then favored. As shown in Figure 5-10(a) and (b), the IGEPAL® CO-520/GO mixture was insoluble in water. IGEPAL® CO-720 showed trend similar to that of IGEPAL® CO-630 when prepared with GO as nanofluids, as stability deterioration was slowed but not stopped.

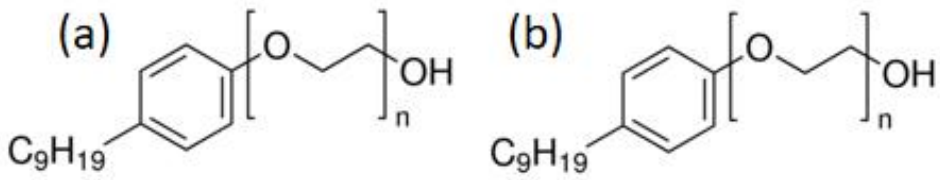

Figure 5-9. Chemical structure of (a) IGEPAL® CO-520, *n* = 5, HLB = 10 [172], (b) IGEPAL® CO-720, *n* = 10~12, HLB = 14[172].

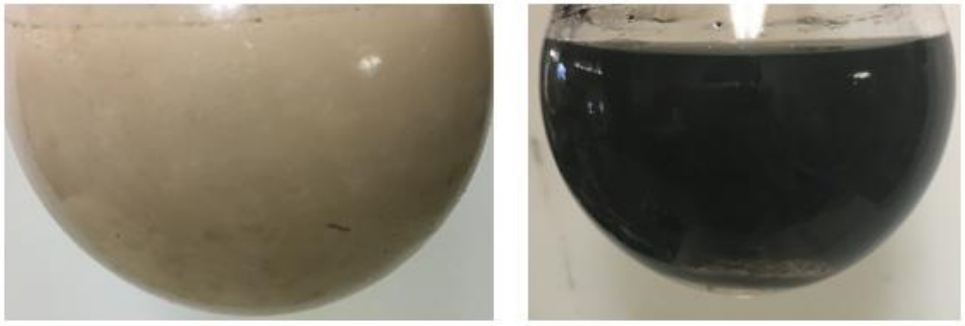

Figure 5-10. (a) GO nanofluids functionalized with IGEPAL® CO-520 as prepared, (b) GO nanofluids functionalized with IGEPAL® CO-720 after boiling and condensation tests for 5 days.

5.5 Functionalization with Nanocellulose

5.5.1 Nanocellulose

Cellulose is an organic polymer chain usually extracted from plants. Nanocellulose is generally prepared from cellulose by using multiple methods, such as mechanical treatment, oxidation treatment, biological treatment, and enzymatic degradation [174]. Oxidation of cellulose occurs when the functional group of hydroxyl groups is replaced by carboxyl groups, as shown in Figure 5-11.

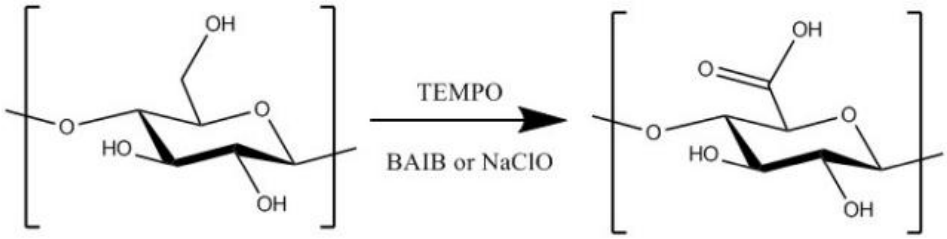

Figure 5-11. Oxidation of cellulose [175].

Cellulose is well known for being hydrophilic due to the bulky presence of oxygen-containing functional groups on its surface. However, it also has extremely low solubility in water because those long microfibrils are firmly bonded to each other by hydrogen bonds. Nanocellulose, however, has a much smaller size, with a width of 3 nm–20 nm and a few micrometers of length [176]. Hwang et al. reported that aggregation and sedimentation of a TEMPO-oxidized cellulose nanofiber (CNF) nanofluid could be prevented due to the low density and long-range repulsion (high zeta potential) of CNF [173]. Figure 5-12 demonstrates the structure and particle dimension of CNF, TEM images, and the potential thermal stability benefits outlined in Hwang et al.'s study.

To evaluate the use of CNF, two different nanofluids were synthesized by Hwang et al. TiO_2 (as a reference nanofluid) in water and CNF in water. For relatively high concentrations of CNF (0.1wt%), increased critical heat flux (CHF) values were measured for the CNF solution. In addition, Hwang et al. found that the turbidity of the CNF-water solution was stable for over a month. Turbidity is an indication of nanoparticle aggregation. In addition, with pool boiling or cooling cycles for their systems, CNF continued to remain stable compared to TiO_2 nanoparticles, with no aggregation or sedimentation reported, while TiO_2 nanofluids were spotted with severe aggregation and sedimentation. Similar to the mechanism of surfactant, which gets adsorbed at interfaces between water and nanoparticles, it therefore prevents

nanoparticle aggregation. The presence of highly branched CNF contributes significantly to the steric repulsive force, preventing particle aggregation and sedimentation.

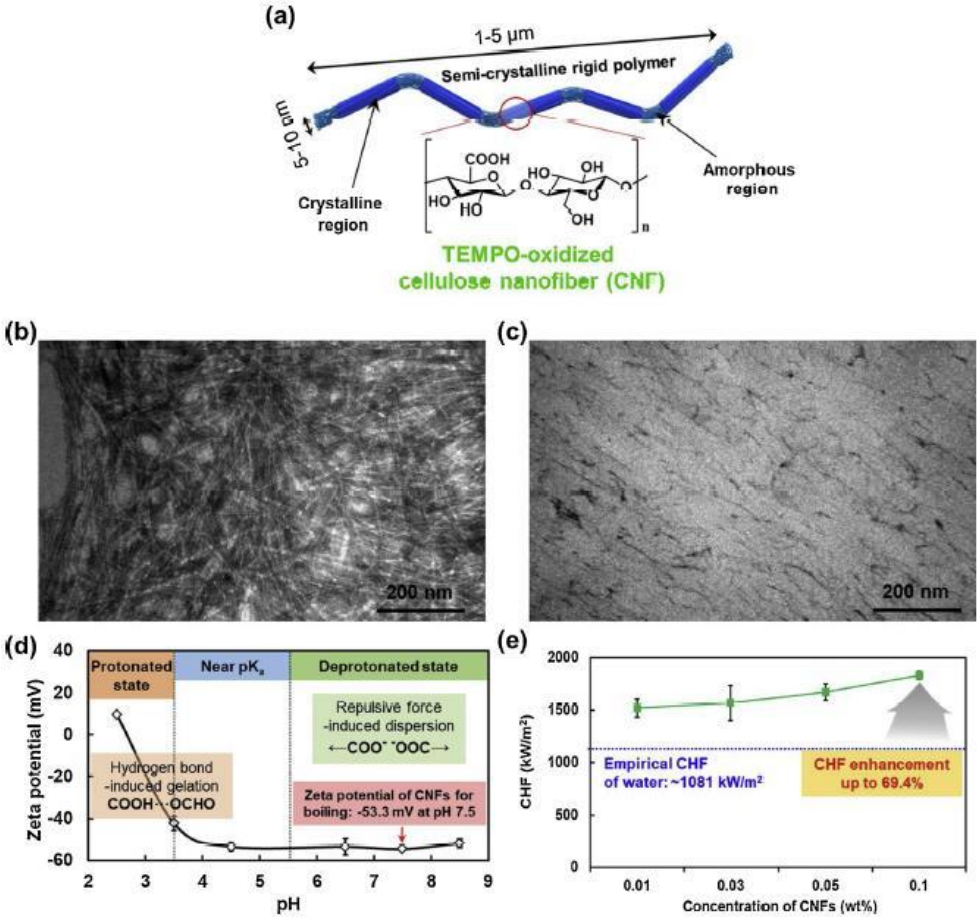

Figure 5-12. (a) Chemical structure of CNF, (b) TEM image of CNF, (c) TEM image of CNF in water, (d) Zeta potential of CNF as a function of pH, I CHF enhancement as a function of CNF loading [173].

5.5.2 Graphene-Based Nanofluids Prepared With Nanocellulose

Dimic-Misic et al. reported that the presence of nanocellulose could effectively prevent the aggregation of graphene nanoparticles when dispersed in water [177]. Malho et al. reported a suspension formed by directly dispersing graphene into a nanocellulose solution. The authors also claimed that such a process was an efficient method to prepare stable and homogeneous graphene nanofluids with a relatively low

loading (1.25wt%) [178]. Han et al. showed that GO nanoparticles aggregated easily in NaOH/urea aqueous solutions, while the presence of nanocellulose could efficiently prevent the aggregation [179]. Further, Nie et al. introduced a uniform dispersion that could be formed by mixing nanocellulose with graphene. Without the presence of nanocellulose, graphene nanoparticles aggregated easily in the aqueous environment [180]. However, most of these experiments were conducted over only several hours, and nanofluid stability was tested and reported to be enhanced only at room temperature. Few papers have discussed the long-term stability and performance of graphene-based nanofluids prepared with nanocellulose, especially when boiling and condensation processes are involved.

5.5.3 Boiling and Condensation Tests for GO/CNF Nanofluids

Because of these promising results reported by other researchers, GO/CNF nanofluids were prepared and tested in this work. The GO/CNF nanofluid underwent the boiling and condensation tests for 11 days. As seen in Figure 5-13, the GO/CNF nanofluids darkened as the processing time increased. Little sedimentation was visually spotted during the test, and the GO/CNF nanofluid remained quite stable visually after 11 days.

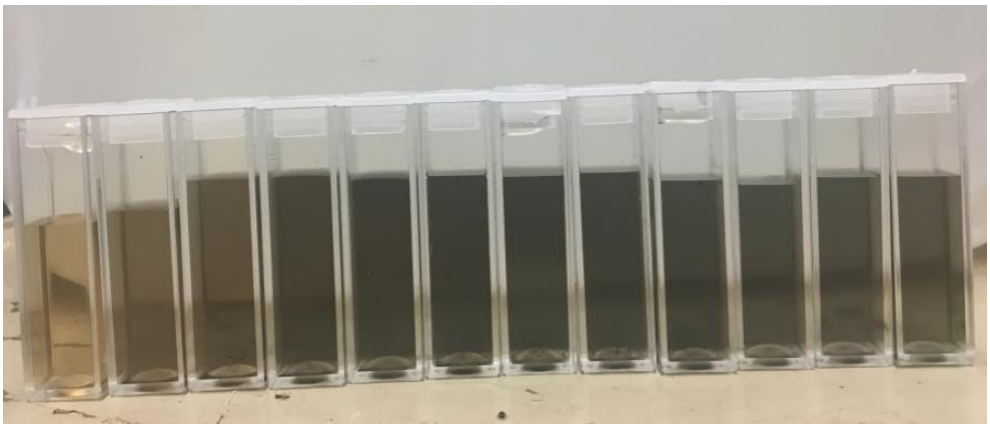

Figure. 5-13. Photo of the GO/Nanocellulose nanofluid for different boiling and condensation process time. From left to right: 0 days (before process) to 11 days.

The transmittance of the nanofluid was also measured every day, with the results presented in Figure 5-14. The transmittance of the prepared GO/CNF nanofluid samples dropped significantly in the first 2 days and remained low for the rest of the testing time. This outcome indicates that the presence of CNF cannot inhibit the reduction of GO nanoparticles. However, it does help considerably in slowing the aggregation and sedimentation of rGO nanoparticles.

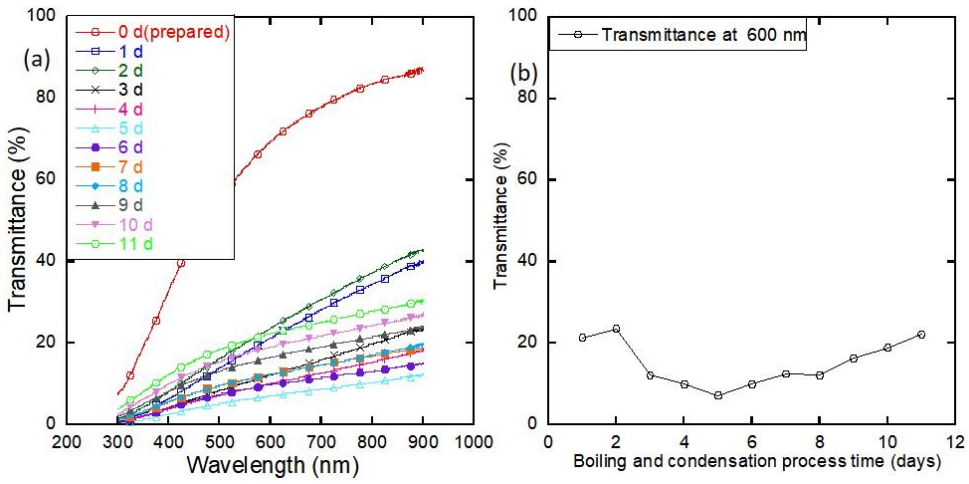

Figure 5-14. (a) Transmittance spectra of the GO/CNF nanofluids for different boiling and condensation processes. (b) Transmittance at 600 nm of the GO/CNF nanofluids as a function of boiling and condensation process time.

5.6 Summary

Multiple methods have been developed and applied in this chapter to address the aggregation problem of GO nanofluids. Original GO nanofluids have a pH value of 4.8, and it was reported that the zeta potential of GO nanofluids could be further decreased to lower than -40 mV, corresponding to more stable nanofluids, by

adjusting the pH value to around 9 [44] [171]. PH-adjusted GO nanofluids were prepared and tested under boiling and condensation processes, and it was proven that pH-adjusted GO nanofluids still underwent GO reduction and aggregated quickly after reduction. The electric double layer formed around GO nanoparticles by pH control is crucial to the mechanism of the electrostatic stabilization of nanofluids. Such a balance could be heavily disrupted by the rapid formation and evolution of bubbles. Therefore, such a method may be less effective when fluid boiling and condensation are involved.

GO nonfluids were also tested with the use of surfactant. GO nanofluids were prepared separately with IGEPAL® CO-520, IGEPAL® CO-630, and IGEPAL® CO-720 as surfactants. The test results showed that GO nanofluids favored surfactants with a higher HLB value. However, the use of surfactant could inhibit neither GO reduction nor particle aggregation during the boiling and condensation processes. The addition of surfactant makes the nanofluids more complicated when it comes to chemical composition analysis. It also affects other physical properties of nanofluids, such as thermal conductivity and viscosity.

Similar to the mechanism of surfactant, the steric repulsive forces between GO nanoparticles are also enhanced due to the presence of CNF. Furthermore, GO/CNF nanofluids were prepared and tested under boiling and condensation processes. The testing result indicated that GO reduction still occurred during the boiling and condensation tests. However, particle aggregation and sedimentation were slowed significantly due to the presence of CNF in GO nanofluids. Notably, CNF and most polymeric surfactants possess very large molecules. Both the addition of surfactant and CNF could complicate the characterization of nanofluids, especially for long-term processes, due to the degradation of macromolecules.

GO nanofluids were found to be light, absorptive, and stable at temperatures below boiling point. GO nanofluids could also remain stable at room temperature for more than 30 days, as well as for 9 days at 120°C in a sealed-tube without boiling. Such observations indicated that GO nanofluids could be a possible candidate for low-temperature solar applications featuring water evaporation, such as solar steam generation. In processes involved with boiling and condensation, GO nanofluid stability significantly deteriorates due to GO reduction. Commonly used methods to prevent particle aggregation—such as pH control, the addition of surfactant, and the addition of CNF—were found to be far less effective when fluid boiling was involved. Only the addition of CNF was found to effectively slow the aggregation of GO nanoparticles under boiling and condensation processes, and GO nanofluids prepared with CNF were found to remain stable for around 11 days.

Charpter 6. Other Possible Solar Absorbing Fluids

6.1 Introduction

In the last chapter, GO nanofluids were found to perform better as working fluids for low-temperature solar apparatus. To develop solar absorbing fluids that could serve in two-phase thermosyphon, multiple fluids (i.e., nanofluids and aqueous solutions) are explored and tested in this chapter. Specifically, rhodamine B aqueous solution, thermal-treated CNF aqueous solution, and commercial printer ink were selected and tested.

6.2 Materials

Rhodamine B was purchased from Sigma Aldrich and used as received. CNF was obtained from the University of Maine. The corresponding aqueous solution was prepared after thermal treatment in our lab. Pigmented black ink was purchased from Inkowl and used as received.

6.3 Rhodamine B

Rhodamine B is a water-soluble dye commonly used in the textile industry. Hence, it is also a common constituent of textile wastewater released into the environment. The chemical structure of rhodamine B is shown in Figure 6-1. Since textile dye is designed to be robust against deterioration caused by weathering, such as UV degradation, biodegradation, and thermal degradation. Traditional wastewater treatment methods have proven ineffective. Therefore, the removal of rhodamine B has been the subject of much research. Su et al. [181] have reported rhodamine B to have good photo-stability, and the color of rhodamine B applied to celery transplants

remained visible after 27 days of exposure to sunlight. Hariprasad et al. [182] reported that without the presence of TiO_2 as a catalyst, the degradation rate of rhodamine B was extremely small under both sunlight and UV light, and the minimum degradation is likely caused by the self-fading of rhodamine B. Not many papers have discussed the thermal degradation of rhodamine B in water. And it was reported by Lin et al. that the degradation of rhodamine B in water could be accomplished by the heat/persulfate process, requiring the addition of sodium persulfate ($Na_2S_2O_8$) to the rhodamine B solution.

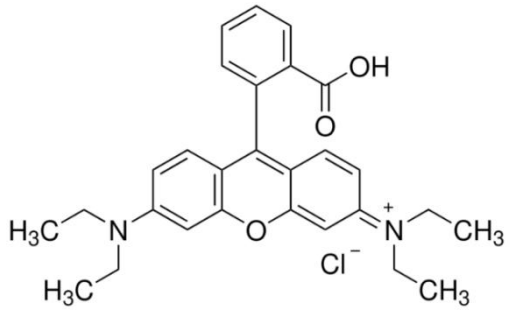

Figure 6-1. Chemical structure of rhodamine B [172].

Due to its strong stability, as reported in other researcher, the rhodamine B aqueous solution was further tested in our lab as a possible solar absorbing fluid. As shown in Figure 6-2(a), rhodamine B appeared red when prepared as an aqueous solution. It was then tested under boiling and condensation processes for up to 9 days. Rhodamine B aqueous solution after the test was also shown in Figure 6-2(b), and little aggregation could be observed.

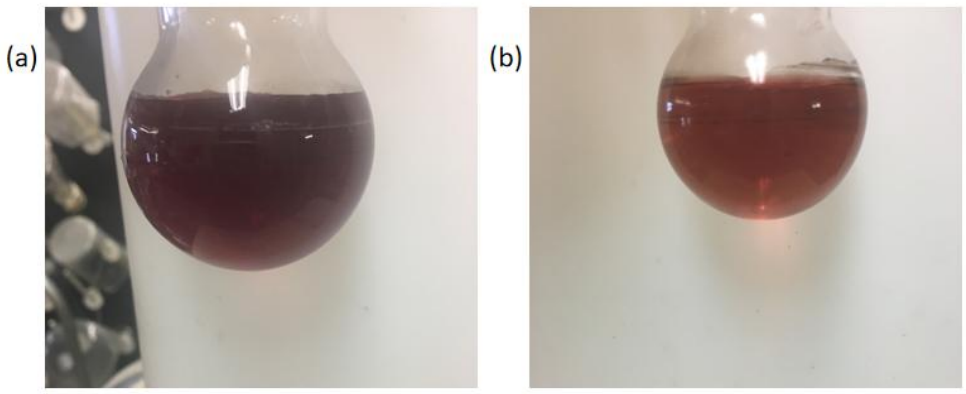

Figure 6-2. Rhodamine B aqueous solution before (a) and after (b) boiling and condensation test for 9 days.

The transmittance of the rhodamine B aqueous solution was measured every day during the boiling and condensation tests, and the results are shown in Figure 6-3. Even though the visual appearance of the rhodamine B aqueous solution changed little during the test, the transmittance spectra still increased as the processing time increased, as shown in Figure 6-3(b). Rhodamine B aqueous solution was found to be more stable than GO nanofluids during the boiling and condensation tests. However, it was also found to be less absorptive than GO nanofluids. Figure 6-3 (a) showed that the rhodamine B aqueous solution was absorptive before 600 nm and almost transparent over 700 nm.

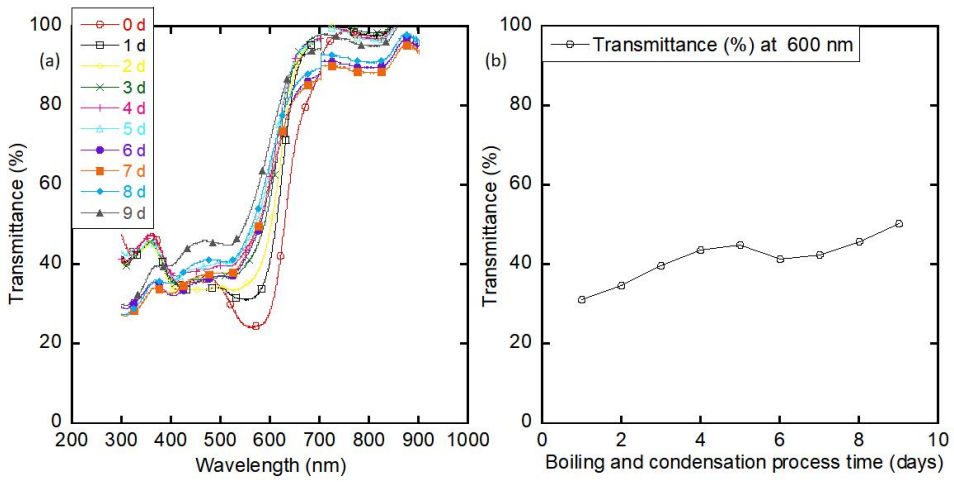

Figure 6-3. (a) Transmittance spectra of the rhodamine B aqueous solution for different boiling and condensation processes. (b) Transmittance at 600 nm of the Rhodamine B aqueous solution as a function of boiling and condensation process time.

6.4 Thermal-treated CNF

CNF drew our attention during the test of GO/CNF nanofluids due to the superb solubility and stability presented by CNF itself. However, the aqueous solution prepared with CNF alone is almost transparent, making it far less attractive than volumetric-absorbing fluids. Similar to GO, thermal reductions such as decarboxylation and decarbonization were also reported to occur on CNF when temperatures rose above 250°C [183]. However, Niskanen et al. [184] reported that the discoloration of CNF could take place between 150°C and 200°C, which was below the typical degradation temperature of CNF. A significant decrease in transmittance was then observed after the discoloration of CNF.

Due to the drastic optical property change of CNF at high temperatures reported by other researchers [173], [183], [184], a thermally treated CNF aqueous solution was then prepared in our lab. As seen in Figure 6-4, the CNF solution was transparent when prepared in water, and the appearance changed from transparent to light brown after being heated inside an autoclave at 180°C for 24 h.

Figure 6-4. Photos of (a) CNF solution prepared in water, (b) thermal treating process in an autoclave at 180°C, and (c) thermally treated CNF aqueous solution.

The CNF aqueous solution was then tested under the boiling and condensation processes. And the transmittance data was collected every day after the test. As seen in Figure 6-5(a), original CNF aqueous solution was almost transparent from 300 nm to 900 nm. Thermally treated CNF showed a significant decrease in transmittance. The boiling and condensation tests lasted 6 days. As seen in Figure 6-5(b), the thermally treated CNF aqueous solution was quite stable through the test, and the transmittance changed little after a 6 day test.

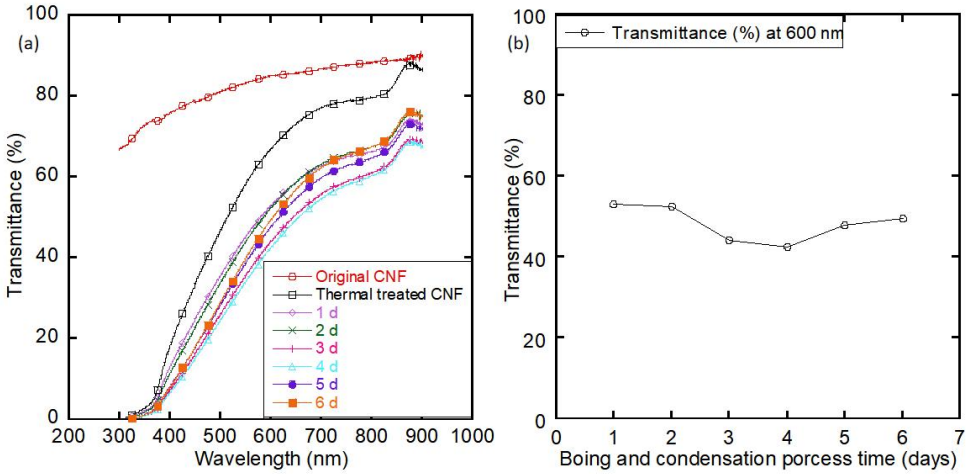

Figure 6-5. (a) Transmittance spectra of the CNF aqueous solution for different boiling and condensation processes. (b) Transmittance at 600 nm of the thermally treated CNF aqueous solution as a function of boiling and condensation process time.

6.5 Pigmented Black Ink

The potential of ink-based nanofluids as solar absorbing fluids was also investigated in this chapter. Wang et al. [185] reported the application of Chinese ink

as solar absorbing fluids in solar thermal collectors, and it was reported that Chinese ink could remain stable for 4 h at 80°C. Zuo et al. [186] investigated the photo-thermal conversion properties and stability of lampblack ink nanofluids, and lampblack ink with 0.2 wt% loading was reported to reach nearly zero transmittance from 190 nm to 1100 nm. Prepared lampblack ink was also reported to show little sedimentation after 15 days of storage at room temperature. Zhu et al. [187] proposed the application of cuttlefish ink nanofluids as working fluid in direct absorption solar collectors, and they reported an overall photo-thermal efficiency of 60.2% under solar simulator irradiation with 0.02 wt% cuttlefish ink nanofluids. The solar collector was operated for 2 h in the range of 24°C to 90°C, and the cuttlefish ink nanofluids were reported to remain stable throughout the experiment.

Various types of commercial inks were tested in our lab, including Chinese painting ink, two types of black refill ink for printers, and pigmented black ink. Among all the selected commercial inks, only pigmented black ink was found to show little sedimentation during the boiling and condensation tests. As seen in Figure 6-6, the appearance of pigmented black ink turned dark brown from black after a 20-day test, and little sedimentation could be spotted after the test.

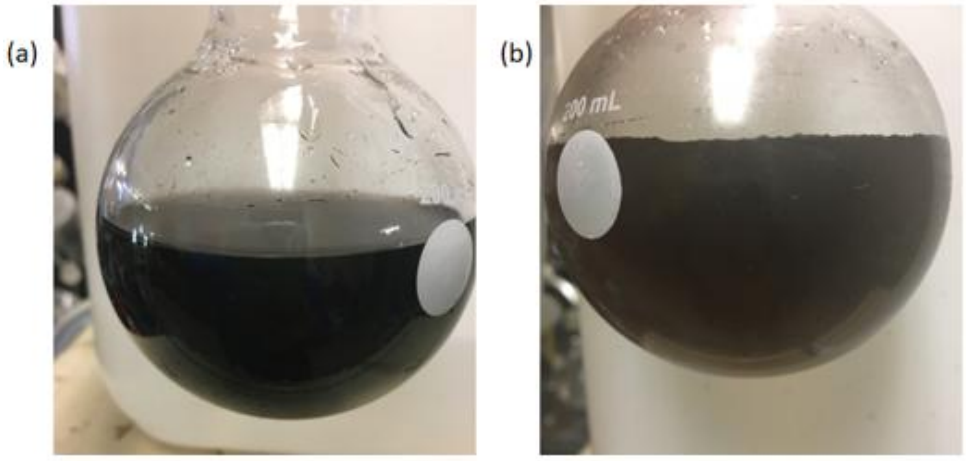

Figure 6-6. Pigmented black ink before (a) and after (b) boiling and condensation test for 20 days.

The transmittance spectra of pigmented black ink were collected during the boiling and condensation tests. Figure 6-7 shows that while the fluid remained homogeneous, pigmented black ink slowly "faded" as the processing time increased.

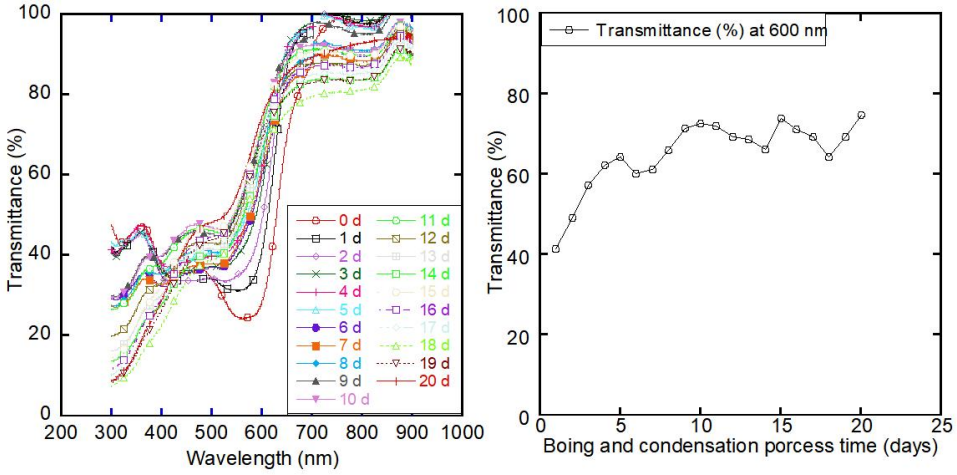

Figure 6-7. (a) Transmittance spectra of the pigmented black ink for different boiling and condensation processes. (b) Transmittance at 600 nm of pigmented black ink as a function of boiling and condensation process time.

6.6 Summary

This chapter tested and evaluated the potential of fluids other than nanofluids to work as solar absorbing fluids, including rhodamine B, thermal-treated CNF, and pigmented black ink. Due to the severe particle reduction and agglomeration issues encountered with GO nanofluids, we emphasized fluidic stability. The rhodamine B aqueous solution was found to remain stable during the boiling and condensation tests with little transmittance change. However, as the vast majority of solar energy was concentrated in the visible and near-infrared regions. Rhodamine B itself is much less absorptive in this wavelength band than GO nanofluids. The original CNF aqueous

solution was almost transparent. The thermal treatment significantly enhanced its light absorption capacity, although it was still not as good as that of GO nanofluids. The thermally treated CNF aqueous solution also showed good stability during the boiling and condensation tests, as the transmittance remained nearly unchanged. Pigmented black ink was found to show little sedimentation over the course of the test. However, the transmittance slowly increased as the processing time increased, and it kept increasing even after the 20-day test.

Charpter 7. Aqueous Dye Solution for Volumetric Solar Absorption

7.1 Introduction

Despite the poor solar absorption capacity of rhodamine B and pigmented black ink, the superb stability of these two types of dye has still drawn much of our attention. The prosperity of the textile industry has also prompted many researchers to evaluate the properties and degradation mechanisms of different dyes. In this chapter, possible dye fluid candidates were downselected after reviewing their chemical structure and degradation mechanisms. These candidates were further tested and evaluated with boiling and condensation processes.

7.2 Photo Degradation of Dye

The dyeing and textile industries nowadays use over 100,000 commercially available synthetic dyes. Annually, around 1000 tons of these dyes are discharged into natural streams and water [188], [189]. Since dyes are designed to be stable against chemical and photological processes, wastewater containing dyes seriously threatens the environment. Therefore, dye degradation has attracted much attention in wastewater treatment. Figure 7-1 shows the several main methods of dye treatment. Conventional physical methods, such as adsorption, membrane filtration, and ion exchange, can be used for dye treatment. Chemical processes such as ozonation, chemical oxidation, electrolytic precipitation, and photodegradation have also been used to remove dyes from wastewater.

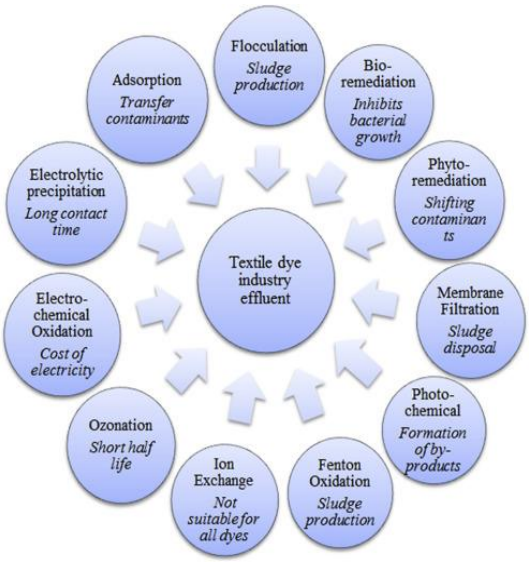

Figure 7-1 , Treatment methods of dye in waste water.[190]

Since we seek dye candidates for solar absorption, a comprehensive mechanism study of the photodegradation of dye is necessary. The typical photodegradation of a dye is shown in Figure 7-2. Semiconductors are widely used as photocatalysts for dye degradation. Upon irradiation with incident photons, electrons are excited in the conduction band (CB) of the photocatalyst, while holes are formed in the valance band (VB). The photo-excited electrons and holes can further produce superoxide radicals (O_2) and hydroxyl radicals (OH). These reactive species can react with the dye molecules absorbed by the surface of the photocatalyst and decompose them into small molecules such as CO_2 and H_2O [191].

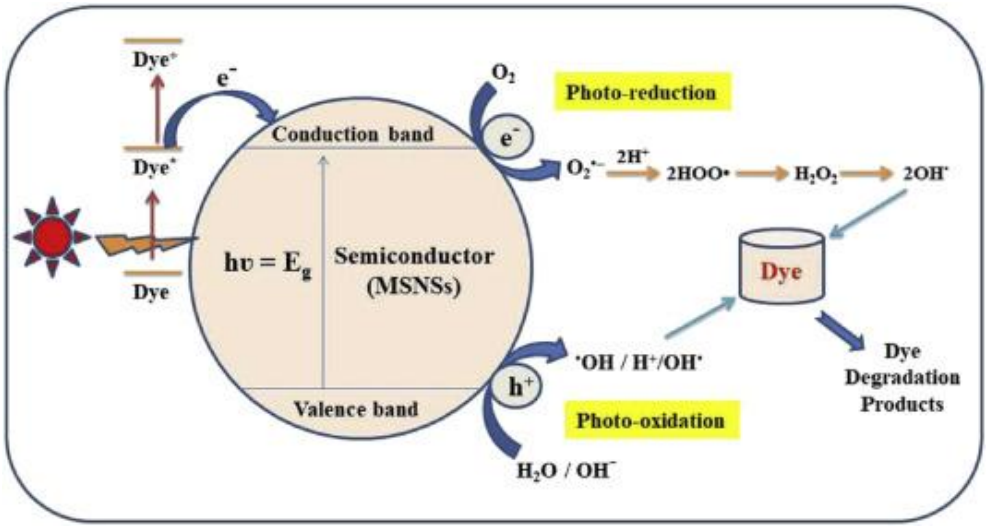

Figure 7-2. Schematic illustration of photodegradation of dyes over semiconductor photocatalysts.[192]

The photodegradation of dyes assisted by photocatalysts is widely studied as a green and sustainable method of dye treatment. However, not many papers have considered the photodegradation of dye without the presence of photocatalysts. Most experiments in studies focusing on wastewater treatment are also extremely time-limited, and their light exposure time is usually within a few hours [193,194,195,196,197]. In the degradation of dye exposed to sunlight alone (as shown in Figure 7-3), no significant degradation has usually been observed [198].

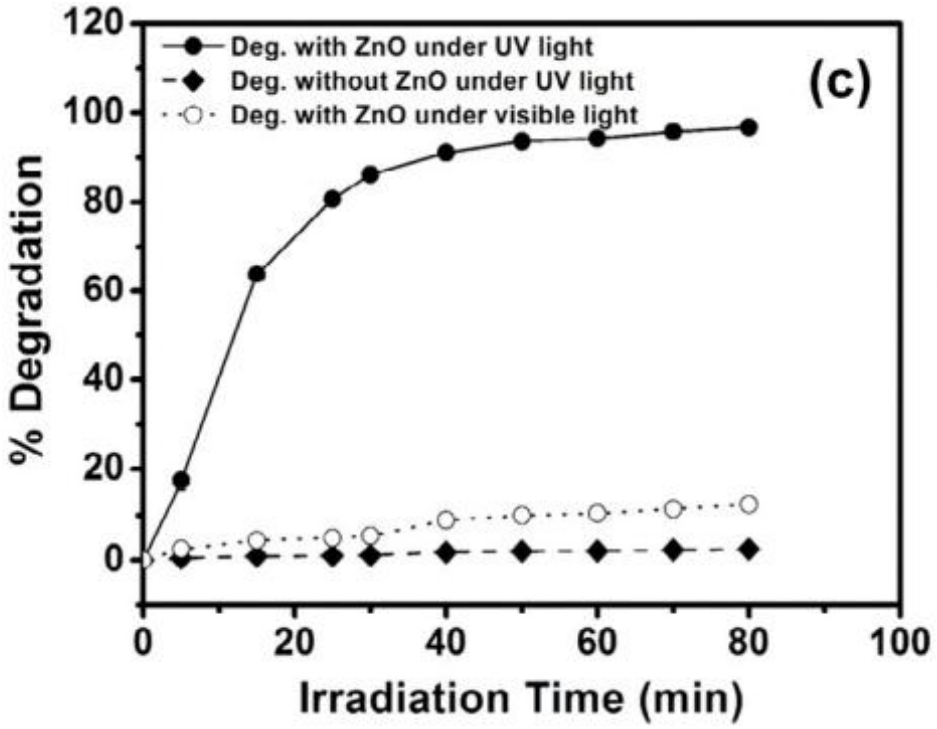

Figure 7-3. Degradation rate (%)of Rhodamine B dye with respect to time intervals for the photocatalytic degradation of as-synthesized ZnO.[198]

Porter [199] studied the photodegradation of dye caused by sunlight without a photocatalyst. Exposing the dye solution directly to sunlight at 50°C revealed that nine of 36 dye types (acid black 52, acid blue 40, direct 80, direct blue 86, disperse orange 3, disperse red 15, disperse blue 27, disperse red 60, and sulfur blue 7) showed a very small degradation rate during 200 h exposure time. As an example, the degradation rate of acid black 52 is shown in Figure 7-4. Among these nine types of dyes reported, dispersed dye and sulfur dye were known to be difficult to dissolve in water. Therefore, they were not further investigated in this chapter.

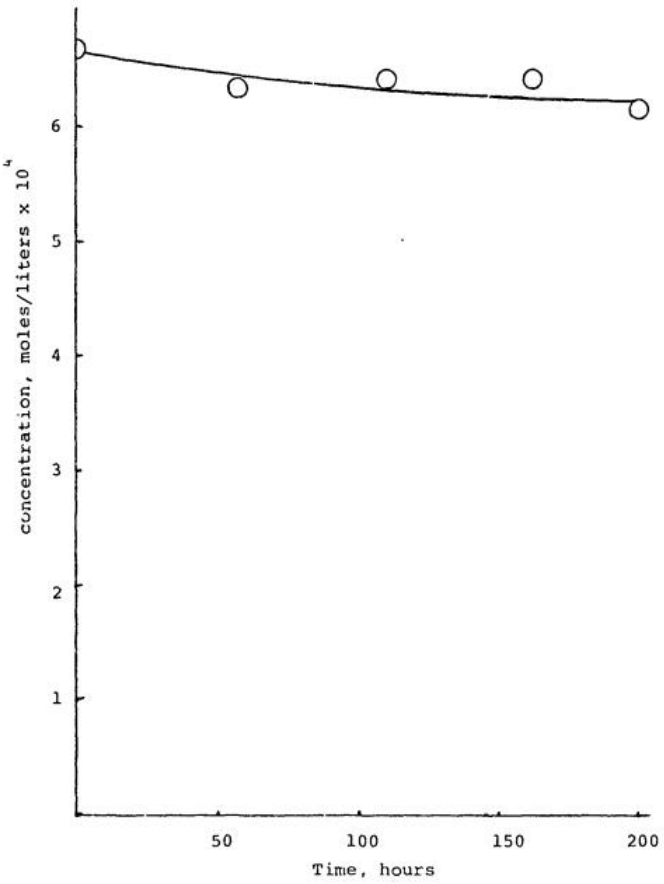

Figure 7-4. Photo-degradation rate of acid black 52 in water at 50°C [199].

7.3 Materials

Acid black 52, basic yellow 9, and basic blue 3 were purchased from Sigma Aldrich. Direct red 80 was purchased from Santa Cruz Biotechnology. Direct blue 86 was purchased from Fisher Scientific.

7.4 Dye Solution Preparation

Due to their reported solubility in water and stability against photo-degradation, acid black 52, direct red 80, and direct blue 86 were downselected as possible volumetric-absorbing fluids. Other types of dye, like basic yellow 9 and basic blue 3, were also studied together. The chemical structure of all the different types of

dye tested is shown in Figure 7-5. To further test the light absorption capacity of different dye solutions. Acid black 52, direct red 80, direct blue 86, basic yellow 9, and basic blue 3 were prepared separately by directly dispersing into DI water at 0.02wt%. Mixture sample 1 was prepared by mixing direct red 80 and direct blue 86 together and being dispersed into DI water with a total particle concentration of 0.02wt%. Mixture sample 2 was prepared by mixing basic yellow 9 and basic blue 3 together and being dispersed into DI water with a total particle concentration of 0.02 wt%. Figure 7-6 shows the digital photo of the prepared mixture sample. To avoid unexpected precipitation, a mixture sample was prepared by mixing the same types of dye.

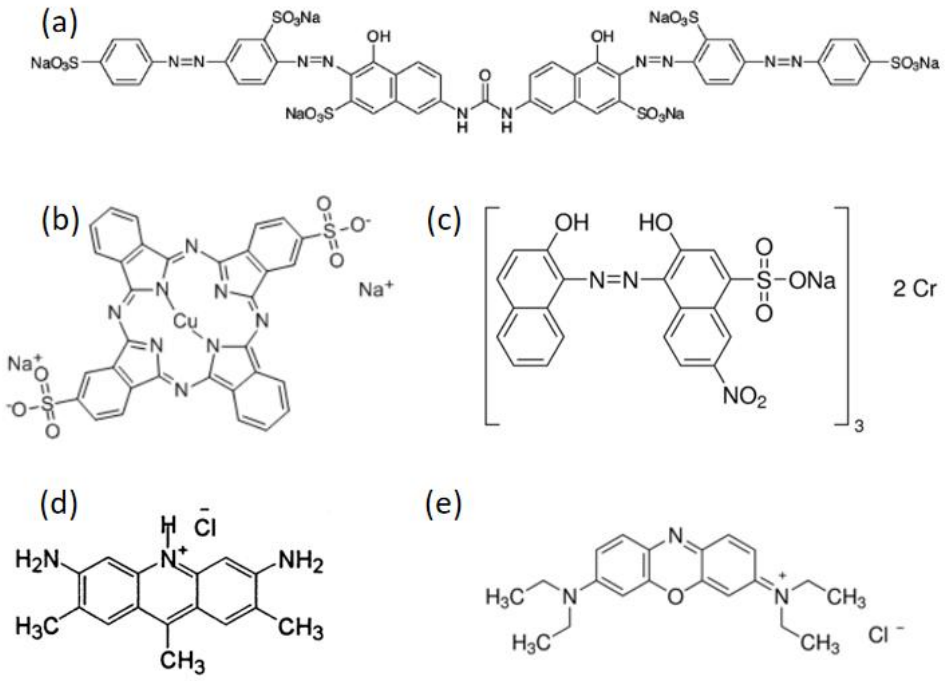

Figure 7-5. Chemical structure of (a) direct red 80 [200], (b) direct blue 86 [201]. (c) acid black 52 [202], (d) basic yellow 9 [172], (e) basic yellow 3 [172].

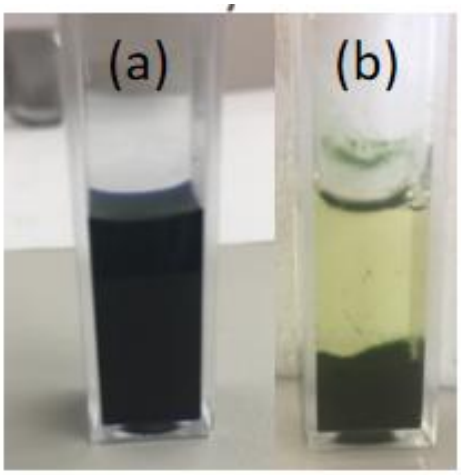

Figure 7-6. Photo of the mixture sample prepared by using (a) same types of dye (direct red 80 and direct blue 86) and (b) different types of dye (acid black 52 and basic yellow 9).

7.5 *Transmittance Measurement of Dye Solution*

The transmittance spectra were also obtained for all the prepared dye solution samples. As shown in Figure 7-7, certain dye types (e.g., direct red 80, direct blue 86, and basic blue 3) were much less absorptive in the near-infrared region. Therefore, mixture samples prepared with different dyes were prepared to enhance light absorption capacity. When prepared at the same concentration, mixture sample 1, mixture sample 2, and acid black 52 showed the lowest transmittance in the visible region.

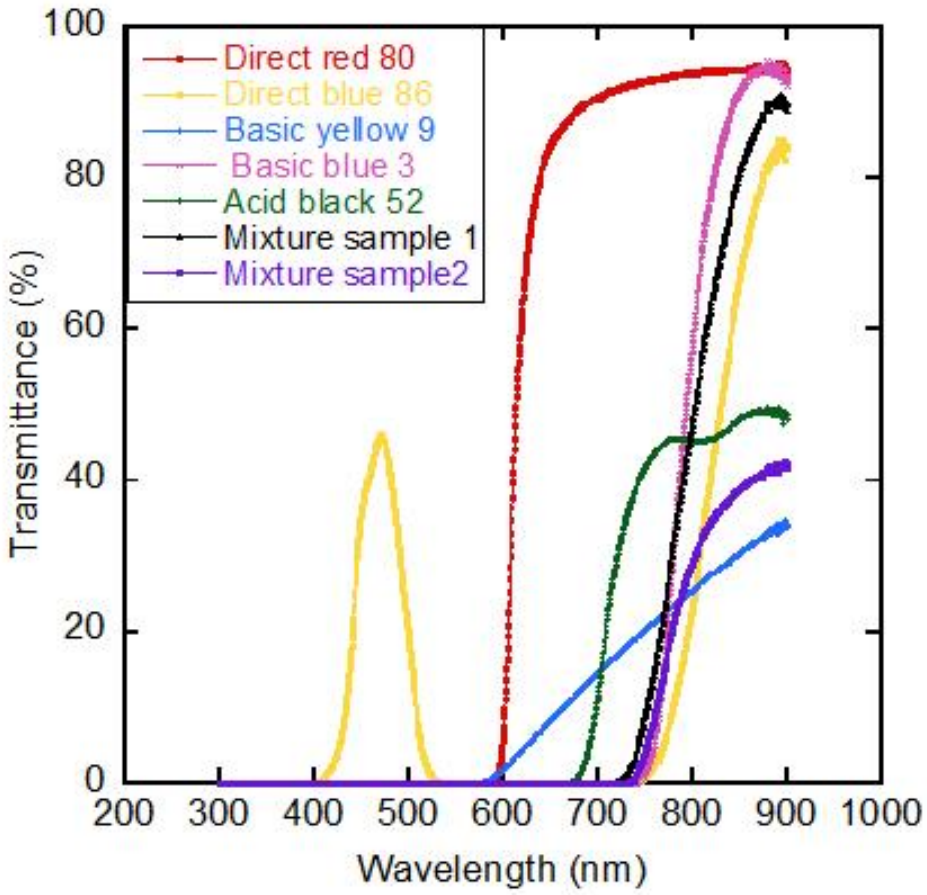

Figure 7-7. Transmittance as a function of wavelength for as-prepared acid black 52, direct red 80, direct blue 86, basic yellow 9, basic blue 3, mixture sample 1, and mixture sample 2 with a weight fraction of 0.02%.

7.6 Boiling and Condensation Tests

Mixture sample 1, mixture sample 2, and acid black 52 were further tested under boiling and condensation processes. As shown in Figure 7-8, the transmittance of mixture sample 1 remained nearly unchanged during the 10-day test, confirming the superb stability of mixture sample 1. It also reached nearly zero transmittance below 700 nm, indicating excellent light absorption capacity in this region. However, the light absorption capacity was weak in the near-infrared region.

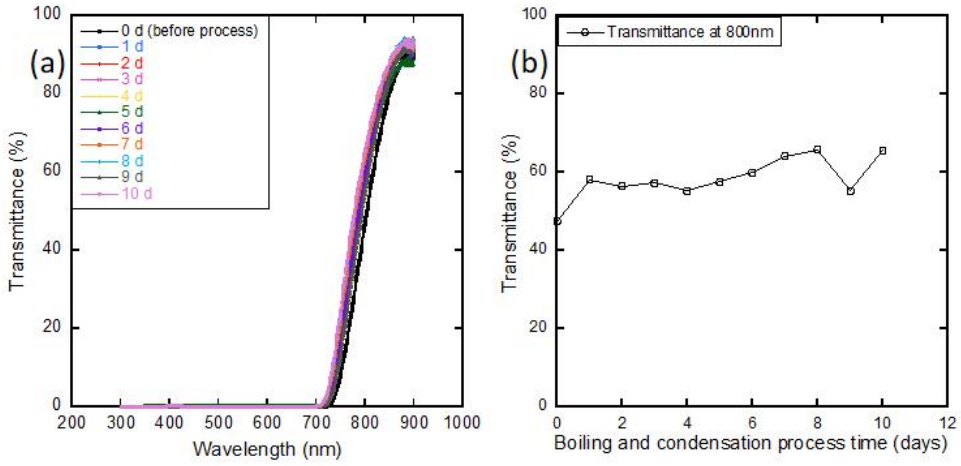

Figure 7-8. (a) Transmittance spectra of mixture sample 1 solution for different boiling and condensation processes. (b) Transmittance at 800 nm of mixture sample 1 as a function of boiling and condensation process time.

Unlike mixture sample 1, the transmittance of mixture sample 2 remained low in both the visible region and the near-infrared region. However, the transmittance was not constant over 9 days of testing, as shown in Figure 7-9.

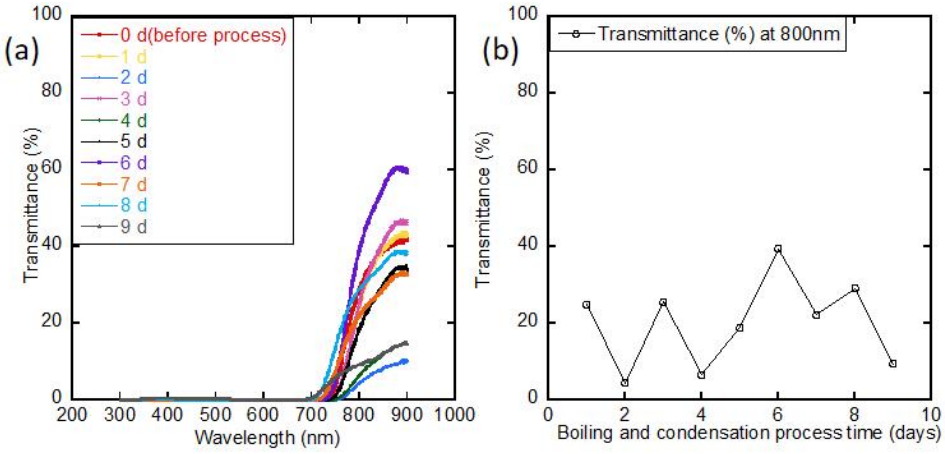

Figure 7-9. (a) Transmittance spectra of mixture sample 2 solution for different boiling and condensation processes. (b) Transmittance at 800 nm of mixture sample 2 as a function of boiling and condensation process time.

The transmittance spectra of the acid black 52 aqueous solution are shown in Figure 7-10. The transmittance data remained both low and nearly unchanged during

the 10-day test. These results indicate that acid black 52 experienced both little degradation and particle aggregation under the boiling and condensation processes. Both the good stability and excellent light absorption capacity of the acid black 52 aqueous solution were retained after a 10-day test.

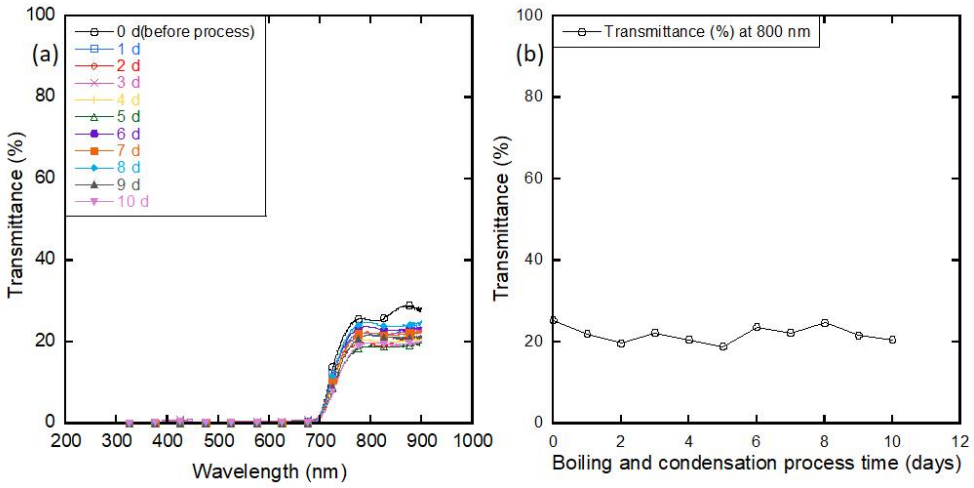

Figure 7-10. (a) Transmittance spectra of the acid black 52 solution for different boiling and condensation processes. (b) Transmittance at 800 nm of acid black 52 solution as a function of boiling and condensation process time.

7.7 FT-IR Analysis of Acid Black 52

To further examine whether there were any chemical changes in acid black 52 on the molecular level, FT-IR spectra of acid black 52 particles were also measured before and after the boiling and condensation tests. As seen in Figure 7-11, all peaks remained nearly unshifted after the 8-day test. Figure 7-12 further demonstrates the relation between peaks and the molecular structure of the acid black 52 particle. The peak at 3400 cm^{-1} is related to hydroxyl groups. The peak at around 1550 cm^{-1} is related to the azobenzene structure. The peaks at around 1420 cm^{-1} and 1200 cm^{-1} both relate to the structure of sulfonate. All those peaks related to the structure of the acid black 52 molecule remained nearly unchanged throughout test.

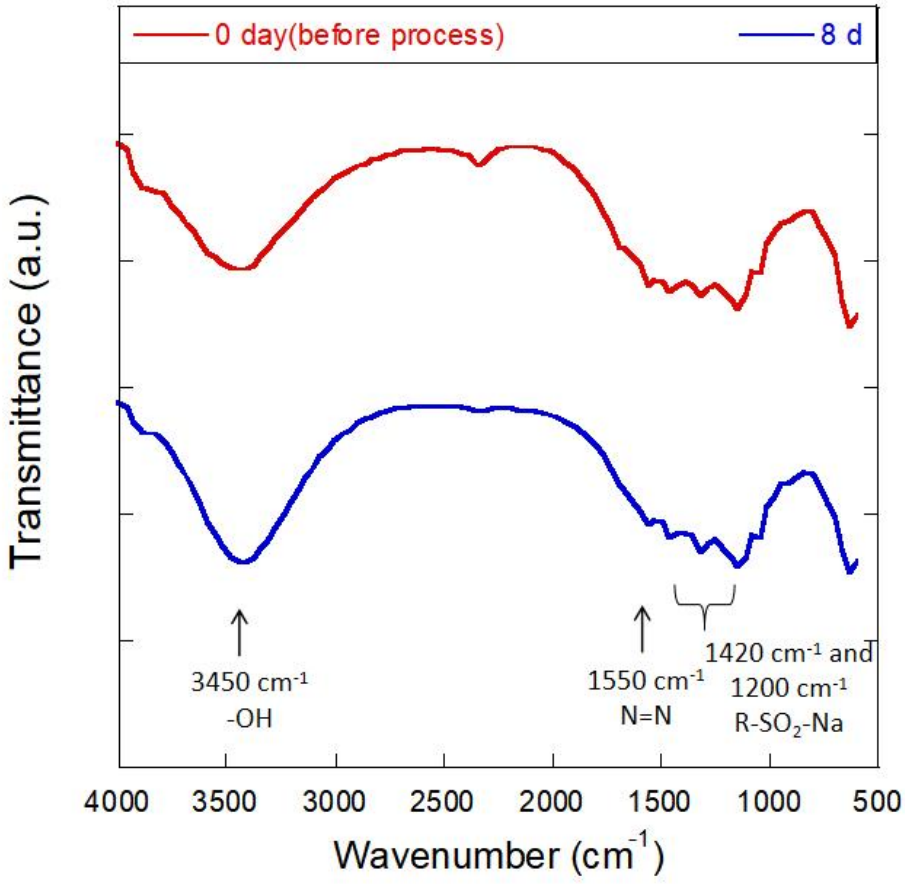

Figure 7-11. FT-IR spectra of acid black 52 solution before and after 8 days of boiling and condensation test.

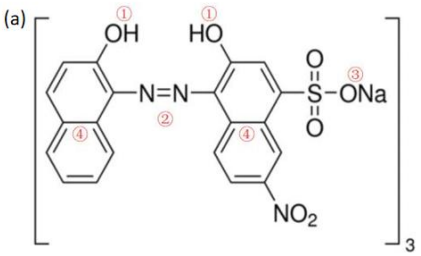

Bond #	Bond	Wavenumber(s) [cm^{-1}]
1	-OH	3,366, 3,471
2	N=N	1,550
3	R-SO2-ONa	1,420 – 1,330 1,200 – 1,145
4	Naphthalene	3,200
Other	CO_2	2,400

Figure 7-12. (a) Chemical structure of acid black 52. (b) Molecular bonds and corresponding wavenumber(s) for FT-IR analysis.

7.8 Viscosity Measurement of Acid Black 52

The viscosity of the acid black 52 solution was measured at different temperatures and with a viscometer. Figure 7-13 shows that the verification of testing

methods was accomplished by comparing the results for water measurement with the data provided by NIST. It was also shown that the viscosity of the sample followed a similar trend for water, decreasing with temperature. Due to the relative low particle concentration, the addition of acid black 52 in water had a little impact on the viscosity of the prepared fluids. The viscosity of the acid black 52 solution was almost the same as that of DI water from 24°C to 90°C.

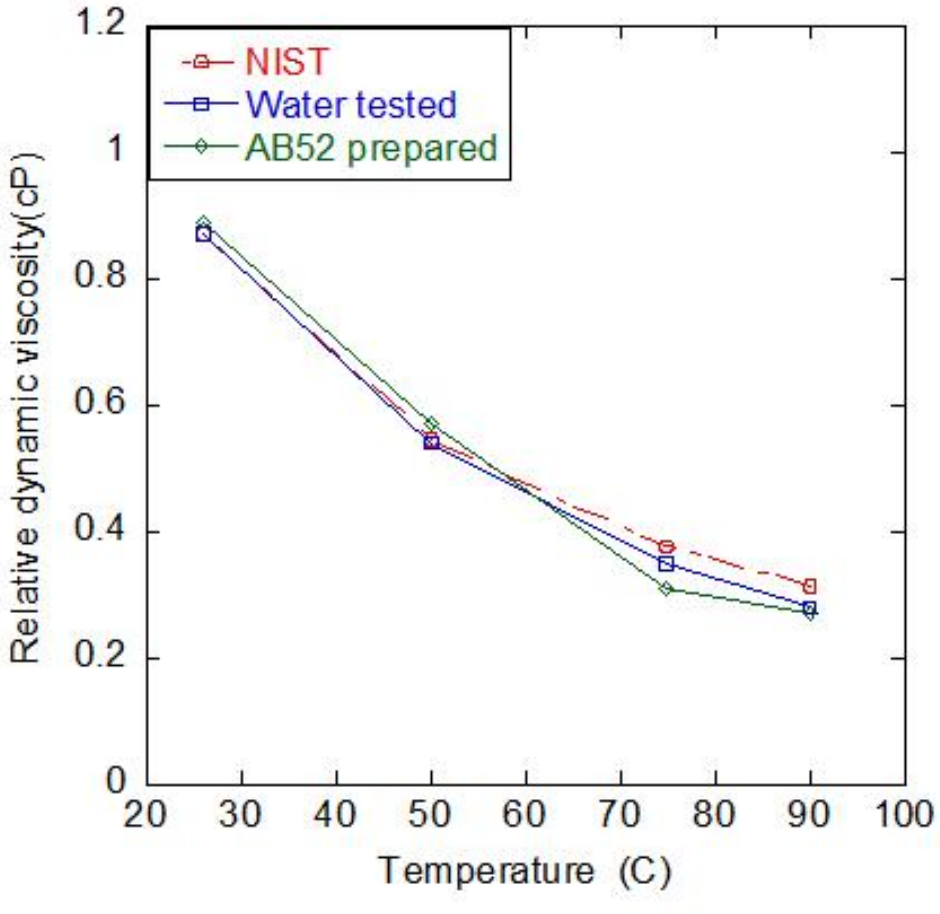

Figure 7-13. Relative dynamic viscosity of acid black 52 dye solution as a function of temperature.

7.9 Summary

The classification and degradation mechanisms of dye have been reviewed in this chapter. Most dyes were reported as robust against weathering, and it was hard to

eliminate dye from wastewater. Photodegradation was widely investigated as an eco-friendly method to remove dye from wastewater, and most photodegradation of dye relied heavily on the use of photocatalysts such as semiconductors.

Multiple types of aqueous dye were tested under boiling and condensation processes, and mixture sample 1 showed superb stability with weak light absorption capacity. Mixture sample 2 showed excellent light absorption capacity, while the stability seemed to be disrupted by the boiling and condensation processes. The acid black 52 aqueous solution showed both superb stability and excellent light absorption capacity during the 10-day test. Further FT-IR analysis confirmed that boiling and condensation processes caused little impact on the chemical structure of the acid black 52 molecule.

Charpter 8. Long-Term Stability Test With Two-Phase Thermosyphon

8.1 Introduction

In the last chapter, both mixture sample 2 and acid black 52 aqueous solution exhibited potential as volumetric absorbing fluids due to their excellent light absorption capacity and stability. Long-term testing with the boiling and condensation experiment setup shown in Figure 3-3 may cause problems such as water loss by evaporation and air contamination. In this chapter, these two samples were further tested inside a two-phase thermosyphon prototype that can be purged with inert gas before testing and well-sealed during long-term operation. Possible degradation mechanism of acid black 52 was discussed. Long term enhanced radiation experiment was conducted with acid black 52 aqueous solution.

8.2 Solar Spectrum and Total Absorbance of Dye

The reference solar spectrum has been refined over the years. The American Society for Testing and Materials (ASTM) G-173 spectra are the general used spectrum for solar research. As seen in Figure 8-1, a global horizontal irradiance spectrum with an absolute air mass of 1.5 (AM1.5G) is displayed and used for total absorbance calculation. AM1.5G is usually chosen as a reference for solar testing because the conditions selected are a reasonable average for the U.S. over one year.

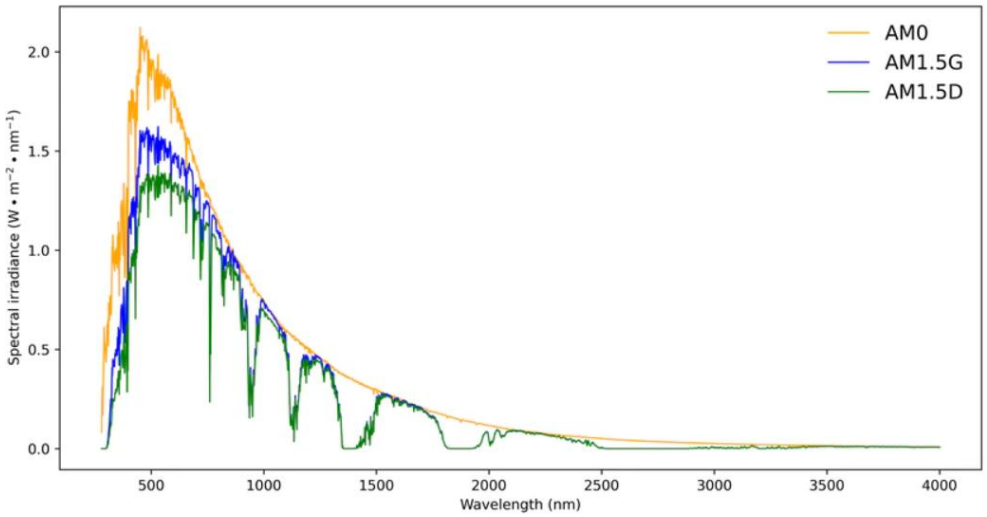

Figure 8-1. Reference solar spectral irradiance (ATSM G173-03) [203].

According to Figure 8-1, around 70% of the energy of solar radiation concentrates in the wavelength band from 300 nm–900 nm. More than 90% of the energy is contained within the spectral range of 300 nm–4000 nm. Only a very small amount of energy exists below 300 nm, and UV exposure could cause the degradation of dye fluids. It is necessary to fabricate a thermosyphon receiver with UV-absorbing glass. Borofloat® was chosen to fabricate a thermosyphon receiver. As seen in Figure 8-2, the transmittance of Borofloat® borosilicate glass below 300 nm nearly reached zero when the thickness of the glass reached 4 mm. And it retained high light transparency in the wavelength band from 300 nm to 2500 nm.

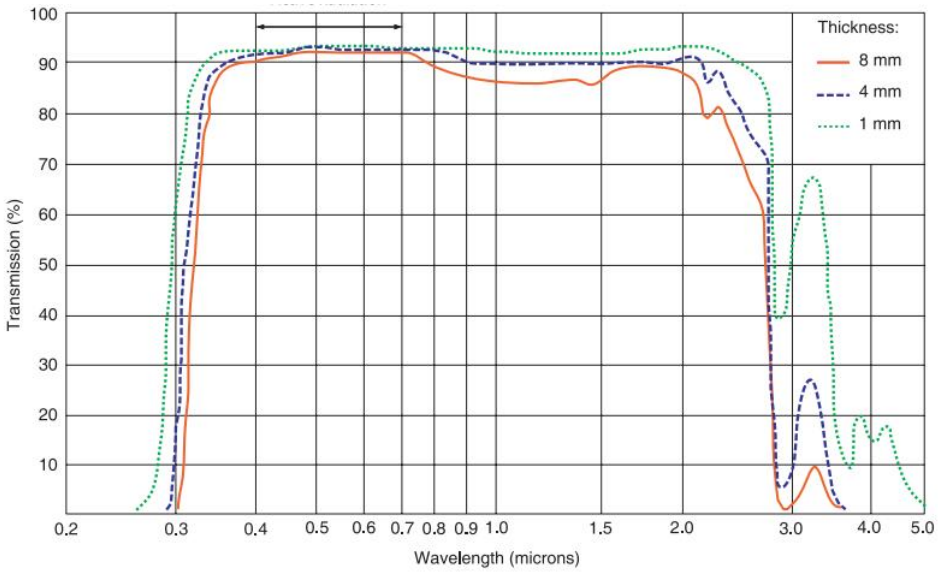

Figure 8-2. Transmission spectrum of the Borofloat® borosilicate glass with different thickness [204].

The optical path/thickness of the fluid is another parameter that will directly influence the absorbance of fluids. As seen in Figure 8-3, the relation between the thickness of the fluid and the spectral absorbance of the acid black 52 aqueous solution was investigated, and the fluid reached maximum absorption when the thickness of the fluid reached 30 mm.

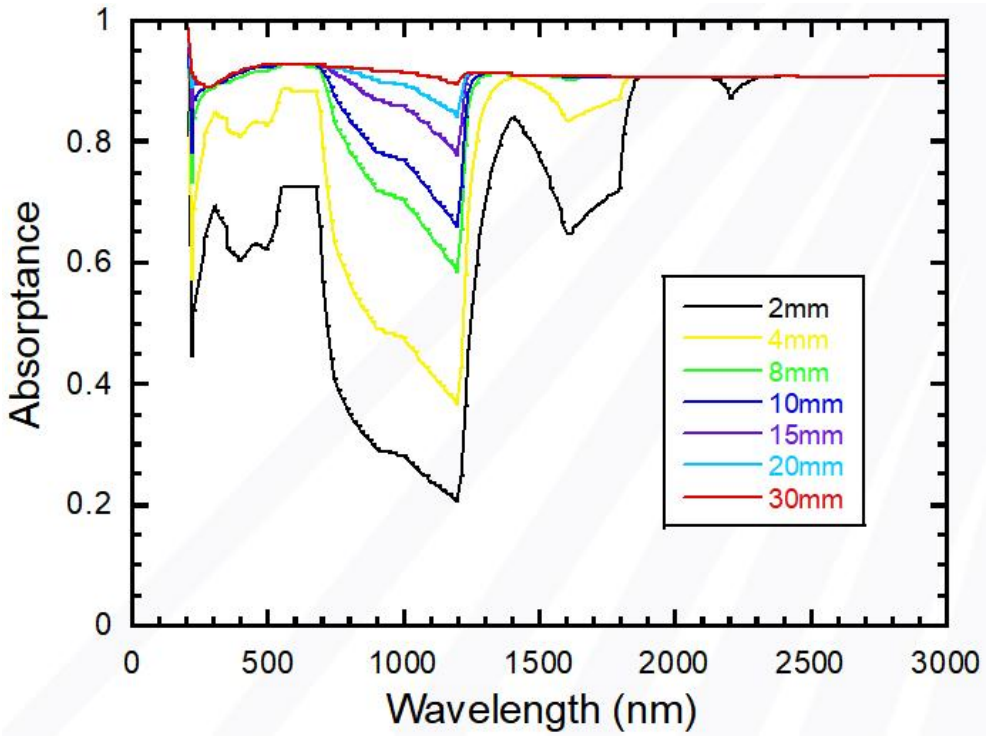

Figure 8-3. Spectral absorbance of the two-phase thermosyphon for the difference thickness of the acid black 52 aqueous solution.

By combining the spectral absorbance of acid black 52 aqueous solution, the transmittance spectrum of Borofloat® borosilicate glass, and the solar spectrum, the relation between total absorbance and thickness of fluid can then be calculated. As seen in Figure 8-4, the total absorbance increased as the thickness of the fluid increased, and a thickness of 15 mm was needed to reach more than 90% solar absorbance.

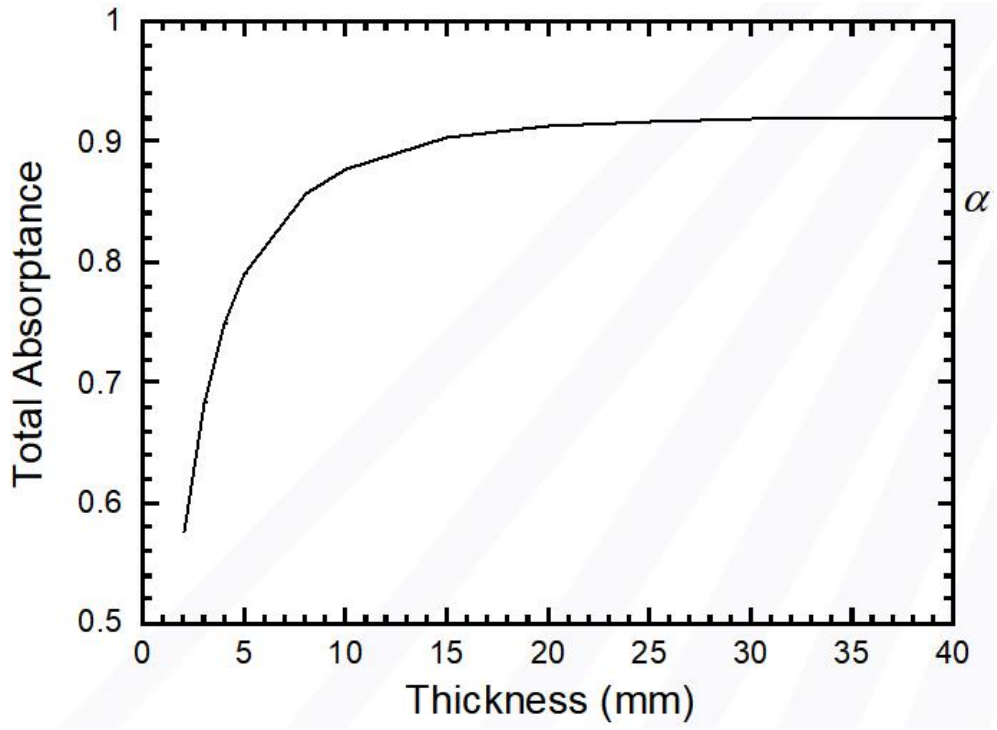

Figure 8-4. Total absorbance of the solar collector increases with increasing thickness of the acid black 52 aqueous solution.

8.3 Two-Phase Thermosyphon Prototype

To further evaluate the performance of mixture sample 2 and acid black 52 aqueous solution, a two-phase thermosyphon prototype was assembled with the help of ACT. To fully visualize the complex two-phase flow throughout the loop. The

glass two-phase thermosyphon prototype is fabricated. As shown in Figure 8-5, a copper wire is used to provide heat to the evaporator, and cooling water (CW) is pumped by a water chiller through an aluminum block for the condenser. Thermocouples (TCs) are placed in the vapor and liquid spaces, and the vapor pressure is measured using a pressure transducer (PT). After charging with prepared volumetric solar absorbing fluids, the fluids are circulated within the thermosyphon.

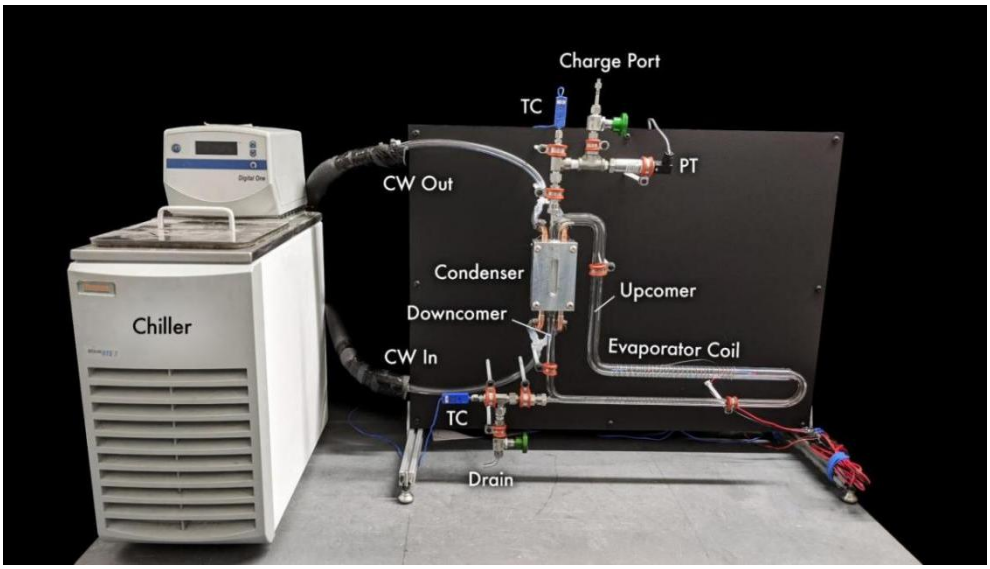

Figure 8-5. Experiment setup of a two-phase thermosyphon prototype built by ACT.

8.4 Long-Term Two-Phase Thermosyphon Test

8.4.1 Long-Term Two-Phase Thermosyphon for Mixture Sample 2

The performance of mixture sample 2 during the two-phase thermosyphon test was further tested on the glass prototype. As shown in Figure 8-6(a), mixture sample 2 can be visually spotted being circulated passively inside the glass thermosyphon prototype. Unlike the boiling and condensation experiment for GO nanofluids, which showed precipitation inside the flask after several days, here there was still no aggregation or precipitation inside the glass even after running for months. The

transmittance change of mixture sample 2 was tracked during the whole experiment. As seen in Figure 8-6(b), the transmittance of mixture sample 2 increased as the testing time increased. The transmittance at 800 nm after a 32-day experiment was almost 10 times larger than the freshly prepared sample.

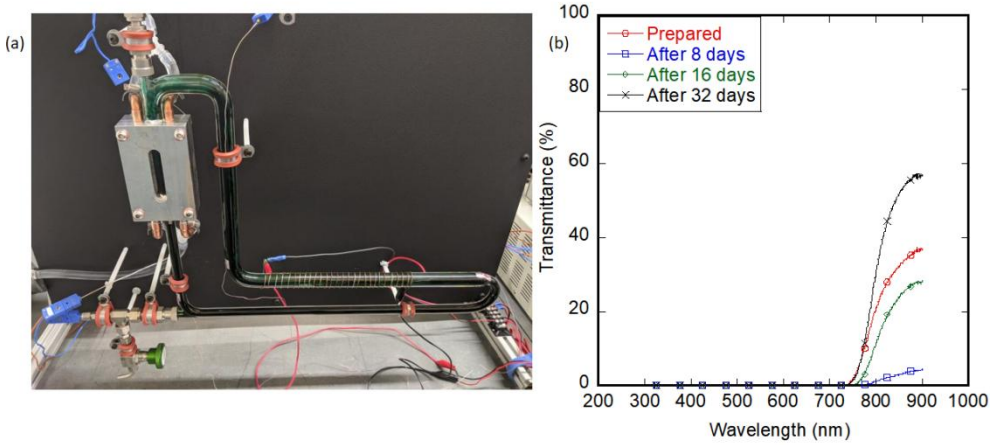

Figure 8-6. (a) Photo of the two-phase thermosyphon experiment of mixture sample 2. (b) Transmittance spectra of acid black 52 solution for different thermosyphon running time.

8.4.2 Long-Term Two-phase Thermosyphon for Acid Black 52

The performance of the acid black 52 aqueous solution was also evaluated with a long-term process. As seen in Figure 8-7, acid black 52 aqueous solution also showed little sedimentation during long-term operation. The transmittance spectra of the acid black 52 aqueous solution are shown in Figure 8-8. Distinct from the performance of mixture sample 2, which increased with processing time, the transmittance of the acid black 52 solution remains low and nearly unchanged during the 199 days of testing.

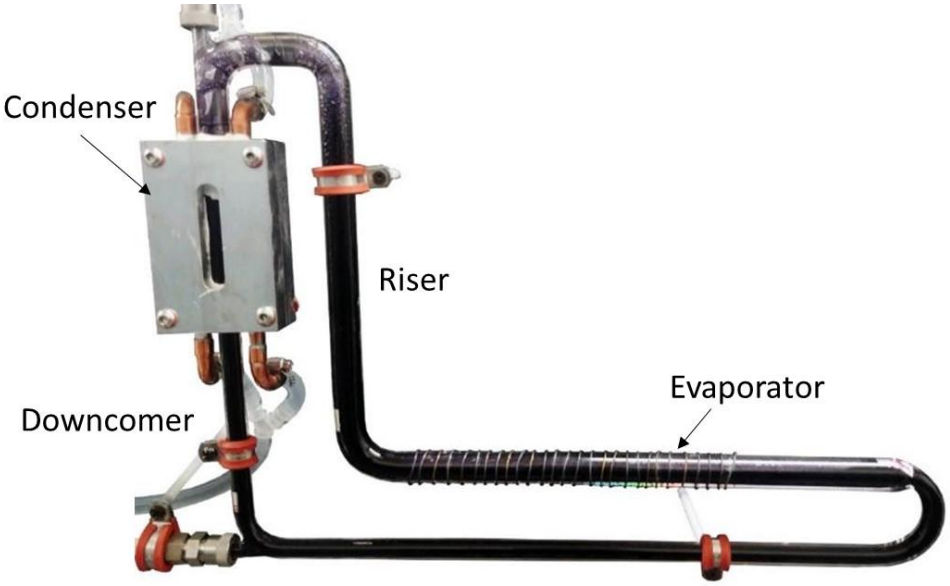

Figure 8-7. Photo of the two-phase thermosyphon experiment with acid black 52 aqueous solution.

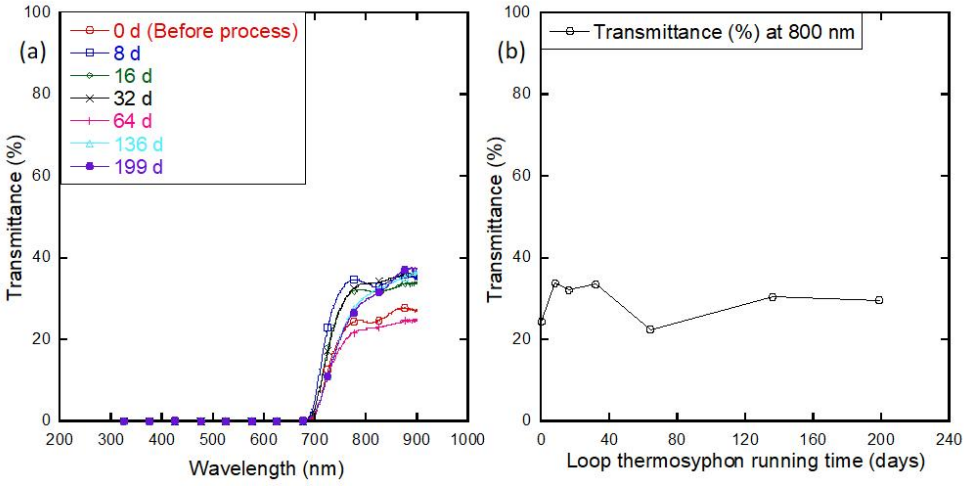

Figure 8-8. (a) Transmittance spectra of the acid black 52 solution for different thermosyphon running time. (b) Transmittance at 800 nm of the dye acid black 52 solution as a function of thermosyphon running time.

8.5 FT-IR Spectra Analysis

The infrared transmission spectra of the acid black 52 aqueous solution were measured to probe the possible change in molecular structure of the black dye during the test in the two-phase thermosyphon, and the results are shown in Figure 8-9. Different wavelengths of IR light are absorbed by different chemical bonds in acid black dye molecules. The large and broad absorption peak at 3400 cm^{-1} is typical of hydroxyl group (O-H) stretches. The peak at around 1550 cm^{-1} is related to the azobenzene structure (N=N). The peaks at around 1420 cm^{-1} and 1200 cm^{-1} are both related to the structure of sulfonate. These IR absorption peaks are characteristic of the molecular structure of the acid black 52 dye molecule, and they remain unchanged throughout the thermal stability test in the loop thermosyphon. Such results indicated that the acid black 52 aqueous fluid remained quite stable during two-phase heat transfer processes.

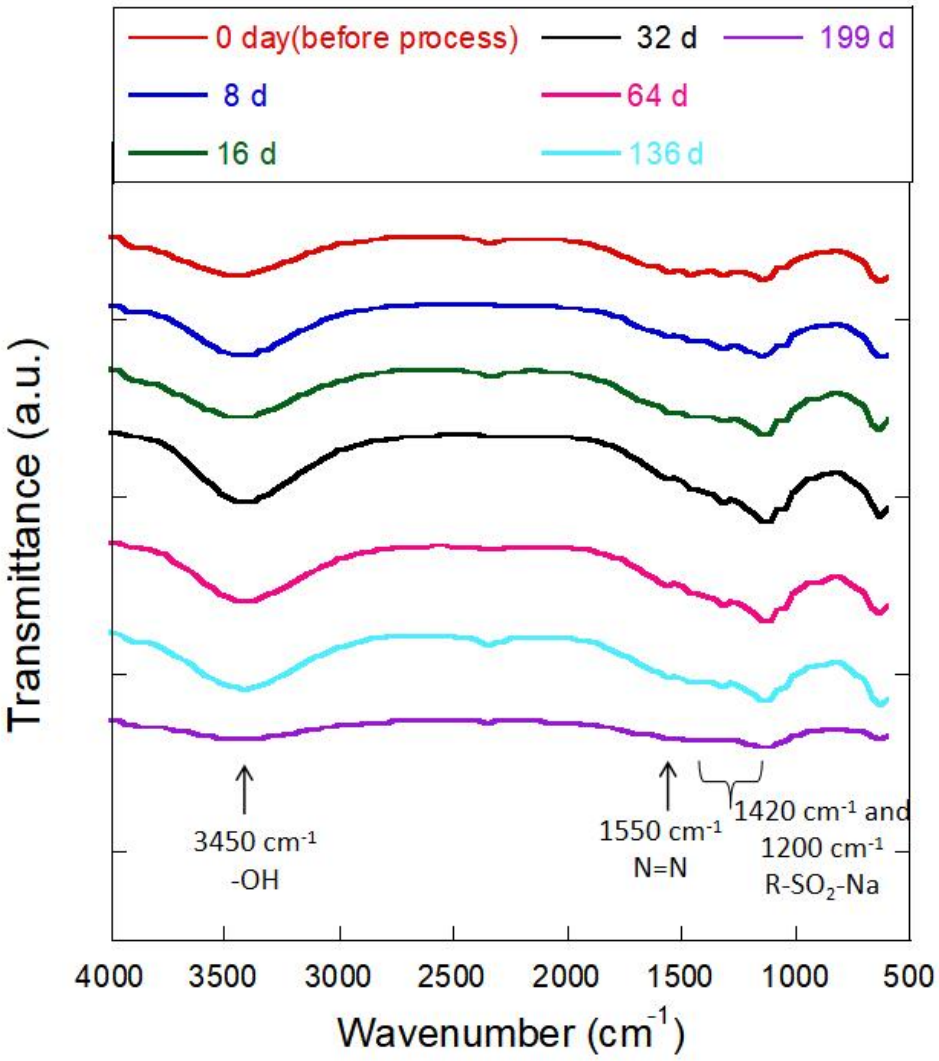

Figure 8-9. FT-IR transmittance spectra of the acid black 52 aqueous solution for different running time in a two-phase thermosyphon.

After reviewing possible degradation methods of acid black 52 dye, we found that UV degradation may be the only way when serving as volumetric absorbing fluids in two-phase thermosyphon. Therefore, an enhanced radiation experiment was developed, and the performance of an acid black 52 aqueous solution under enhanced UV radiation was evaluated in following sections.

8.6 Degradation of Acid Black 52 Dye

The degradation of acid black 52 dye was reported to occur in the presence of high-voltage-generated plasma [205], [206], [207] or UV radiation [199], [208]. Naraginti et al. [208] investigated the degradation of acid black 52 dye under simulated solar light, finding that degradation occurred only in the presence of semiconductor catalysts. Naraginti et al. [208] further proposed a possible degradation mechanism for acid black 52. As seen in Figure 8-10, the removal of hydroxyl groups, sulfonate groups, N=N bonds, and naphthalene rings was considered a sign of the degradation of acid black 52 dye. This observation was in accordance with our understanding of the degradation of acid black 52 dye in Figures 7-11 and 8-9.

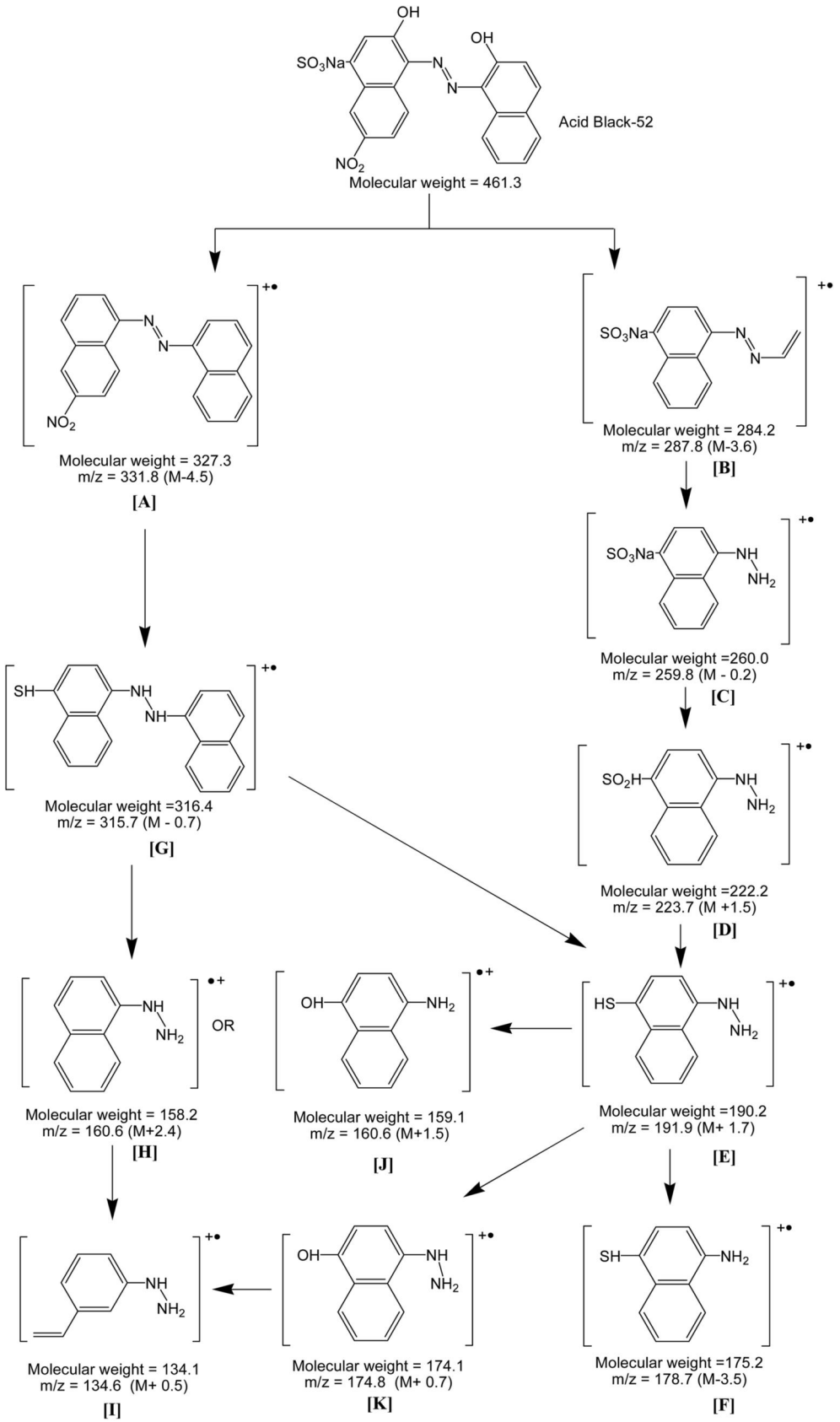

Figure 8-10. Possible degradation mechanism of acid black 52 under simulated solar light [208].

8.7 Long-Term Enhanced Radiation Test

The transmittance of the acid black 52 aqueous solution fluid after an enhanced UV exposure test was also measured. Figure 8-11 shows that acid black 52 changed little in terms of transmittance after 191 days of enhanced UV exposure with five times the flux of the entire UV spectrum of solar radiation. This result further confirmed that acid black 52 dye was robust against UV degradation.

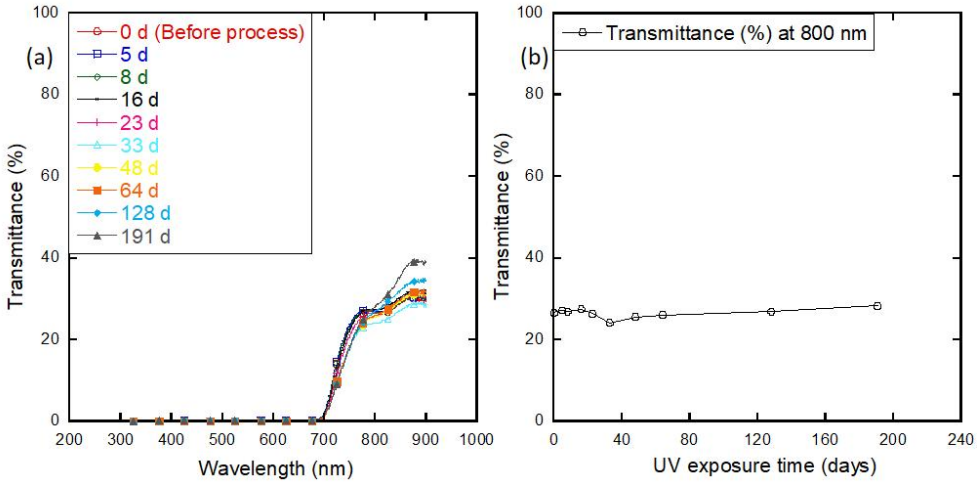

Figure 8-11. (a) Transmittance spectra of the acid black 52 solution for different UV exposure time. (b) Transmittance at 800 nm of the acid black 52 solution as a function of UV exposure time.

8.8 FT-IR Spectra Analysis

FT-IR spectra were collected to probe whether long-term enhanced UV exposure could change the molecule structure of acid black 52 (see Figure 8-12). Characteristic peaks at around 3400 cm^{-1}, 1550 cm^{-1}, 1420 cm^{-1}, and 1200 cm^{-1} remained nearly unchanged throughout the entire UV resistance test. This results indicate that enhanced UV radiation did not greatly influence the molecule structure of acid black 52.

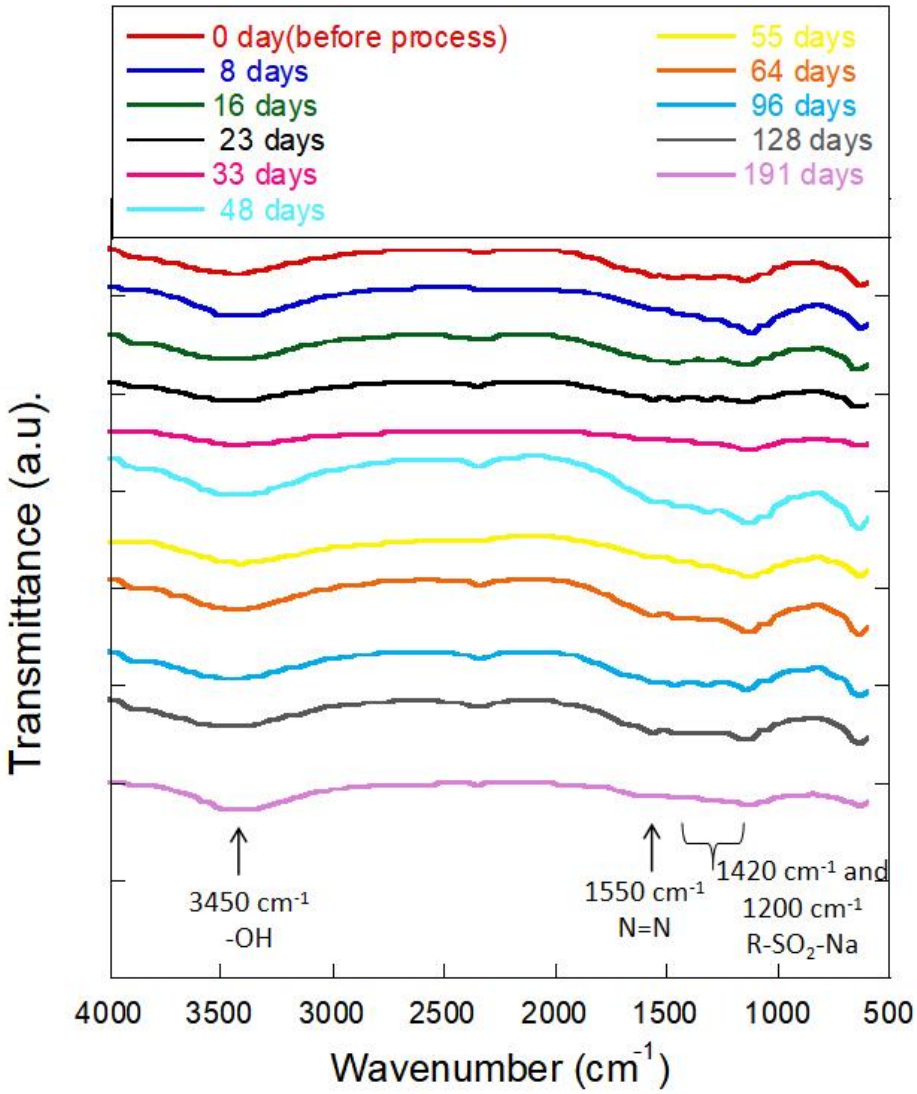

Figure 8-12. FT-IR spectra of the acid black 52 aqueous solution for different UV exposure time.

8.9 Summary

The solar spectrum, the spectral absorbance of acid black 52 aqueous solution, and the transmittance spectrum of Borofloat® borosilicate glass have been investigated in this chapter. It was found that 90% of total absorbance could be reached when the thickness of dye fluids was over 15 mm. A two-phase thermosyphon prototype fabricated with Borofloat® borosilicate glass was assembled and used for a long-term test. Both mixture sample 2 and the acid black 52 aqueous solution showed little

aggregation and sedimentation over the long-term test. After further collecting the transmittance data, it was found that mixture sample 2 turned more transparent as the processing time increased. Such results suggested that the acid black 52 aqueous solution may slowly degrade as the thermosyphon operating time increases. Acid black 52 aqueous solution continuously served as working fluids inside the two-phase thermosyphon prototype for more than 199 days. And it showed constant and low transmittance during the whole test. Such results indicated that the acid black 52 aqueous solution possessed both excellent stability and light absorption capacity. FT-IR analysis further confirmed that long-term processes inside the thermosyphon made little change to the original molecule structure of the acid black 52 particle.

An acid black 52 aqueous solution was exposed to enhanced UV radiation for 191 days at five times the flux of the entire UV spectrum of solar radiation. Both transmittance measurement and FT-IR spectra analysis confirmed that acid black 52 dye was strong against UV degradation.

Charpter 9. Reliability Prediction Based on Stability Test

9.1 Introduction

In Chapters 8, the acid black 52 aqueous solution went through a long-term stability test with two-phase thermosyphon and enhanced UV radiation. Reliability prediction could be approached by estimating the service life of acid black 52 aqueous solution without waiting for actual failures to occur. A two-phase thermosyphon test was conducted at the normal operating temperature, and the service life was estimated based on the average degradation rate during the test. An enhanced radiation test was conducted with enhanced UV radiation exposure compared to solar light, and the service life was estimated based on an accelerated degradation test. Details are given below.

9.2 Reliability Prediction With Two-Phase Thermosyphon

The absorbance spectra of the acid black 52 aqueous solution are shown in Figure 9-1. The large and broad absorption peak at 3450 cm^{-1} is typical of hydroxyl group (O-H) stretches. The peak at around 1550 cm^{-1} is related to the azo-benzene structure (N=N). The peaks at around 1420 cm^{-1} and 1200 cm^{-1} both relate to the structure of sulfonate. These infrared absorption peaks are characteristic of the molecular structure of the acid black 52 dye molecule. According to the Beer-Lambert law, which states that the absorbance of light is proportional to the concentration of chemical species, these three characteristic peaks of the acid black 52 molecule are used to estimate the degradation rate of the acid black 52 aqueous solution.

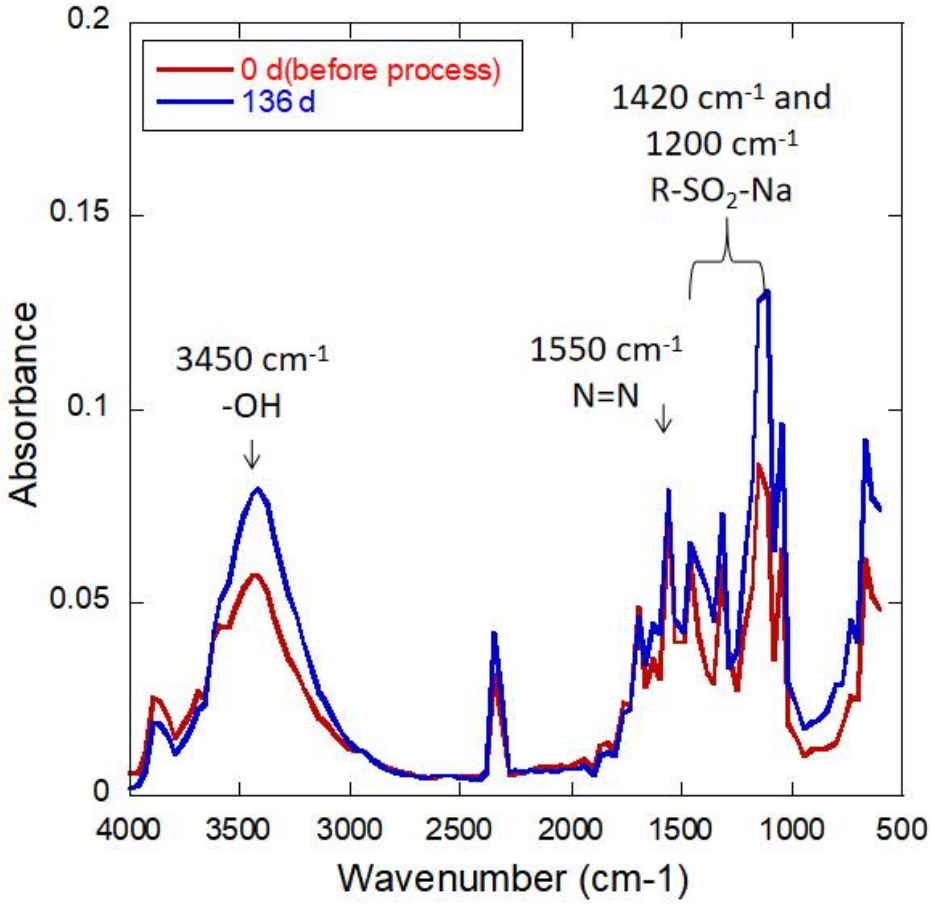

Figure 9-1. Absorbance spectra of the acid black 52 aqueous solution before and after 136-day processing time in two-phase thermosyphon.

The absorbance spectra of the acid black 52 aqueous solution with different processing times are also shown in Figure 9-2. Table 3 lists the absorbance and standard deviation of each characteristic peak. As seen in Table 3, the absorption peaks at 3450 cm^{-1}, 1550 cm^{-1}, 1420 cm^{-1}, and 1220 cm^{-1} changed very little after the 136-day process. We can estimate the degradation rate of the acid black 52 aqueous solution using the equation below:

$$I_t/I_0 = (1-R)^{136}, \quad (8)$$

where I_0 is the initial absorbance value of the peak. I_t is the absorbance value of the corresponding peak. Since the difference in absorbance value is extremely small over time, it is estimated by putting two standard deviations below the averaged

peak value. The degradation rate of the acid black 52 aqueous solution after a 1-day process is represented by R.

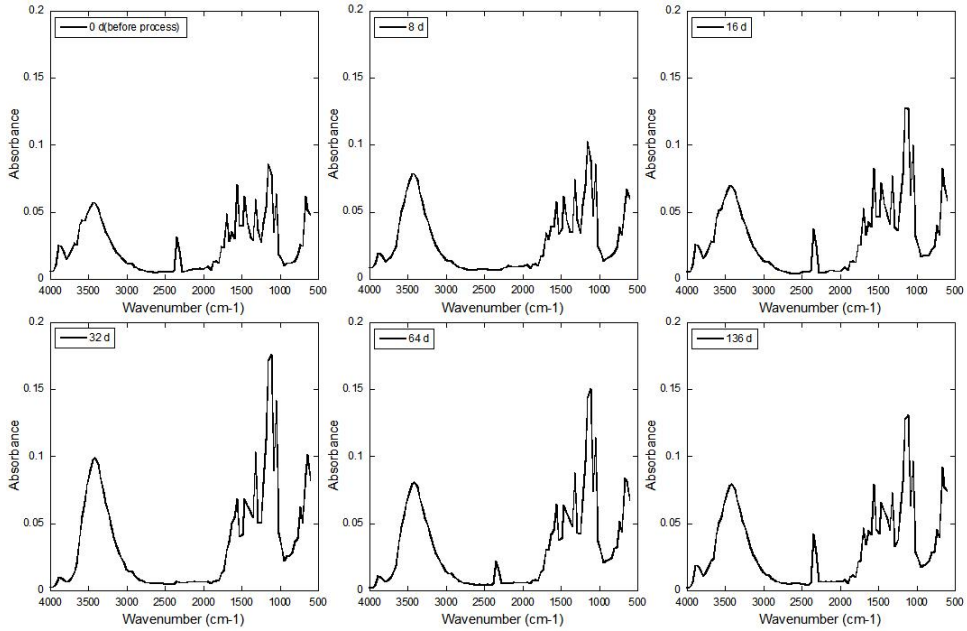

Figure 9-2. Absorbance spectra of the acid black 52 aqueous solution with different processing time in two-phase thermosyphon.

Table 3. Absorbance of characteristic peaks and standard deviation

	Absorbance			
	3450 cm^{-1}	1550 cm^{-1}	1420 cm^{-1}	1200 cm^{-1}
0 d(Before process)	0.05592	0.04212	0.04168	0.05361
8 d	0.07795	0.04204	0.04487	0.07405
16 d	0.06853	0.05160	0.05622	0.07599
32 d	0.09683	0.05897	0.06504	0.11025
64 d	0.07919	0.05152	0.05908	0.09313
136 d	0.07754	0.05376	0.05976	0.07774
Averaged Peak Value	0.07600	0.05002	0.05442	0.08079
Standard Deviation	0.01348	0.00671	0.00916	0.01916

Assuming that the acid black 52 aqueous solution remains usable if more than 50% acid black 52 dye molecules remain unchanged, the expected service life of acid black 52 aqueous solution in a two-phase thermosyphon can be estimated using the following equation:

$$N = lg(1/2)/lg(1 - R), \quad (9)$$

where N is the expected service life (days) of the acid black 52 aqueous solution.

As shown in Table 4, the degradation rate of acid black 52 aqueous solution in a two-phase thermosyphon after a 1-day process is extremely small. Acid black 52 aqueous solution is expected to work continuously for more than 400 days in loop thermosynthetic systems without experiencing notable thermal degradation.

Table 4. Estimated service life of acid black 52 aqueous solution in two-phase thermosyphon

Wave Number	3450 cm^{-1}	1550 cm^{-1}	1420 cm^{-1}	1200 cm^{-1}
Degradation Rate (R)	0.09648%	0.10323%	0.10562%	0.17113%
Expected Service Life (days)	718	671	656	405

9.3 Reliability Prediction With Enhanced Radiation

The absorbance spectra of the acid black 52 aqueous solution were also used to probe the possible change in molecular structure of the acid black 52 dye during the UV resistance test. As seen in Figure 9-3, these characteristic peaks at around 3400 cm^{-1}, 1550 cm^{-1}, 1420 cm^{-1}, and 1200 cm^{-1} remain nearly unchanged after a 128-day UV resistance test. The IR spectra of the acid black 52 aqueous solution with different UV-processing times are also shown in Figure 9-4.

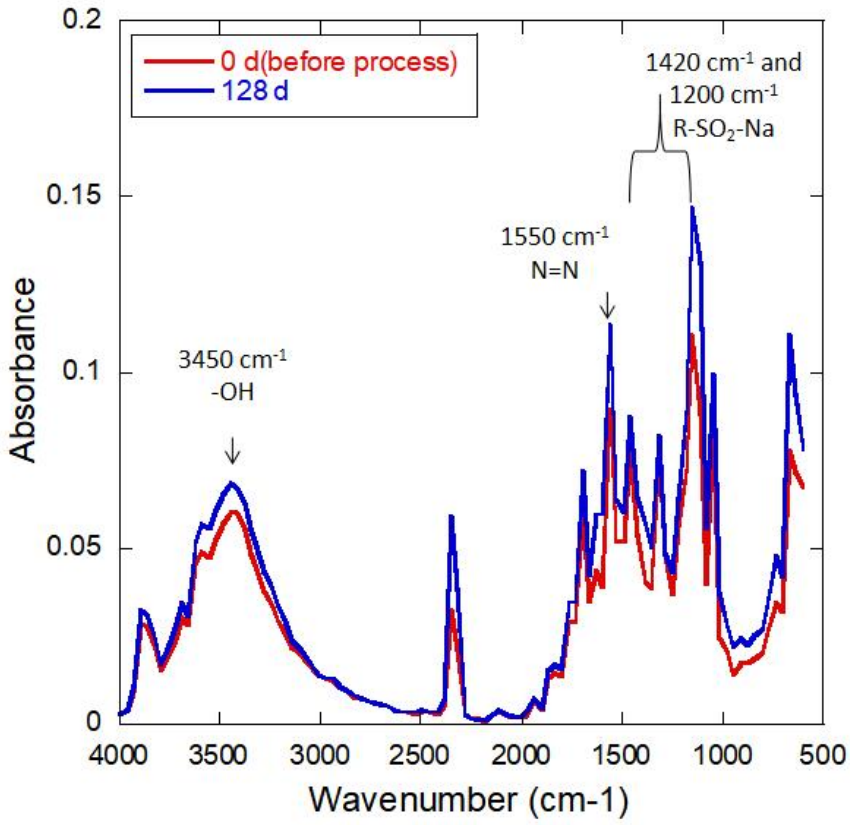

Figure 9-3. Absorbance spectra of the acid black 52 aqueous solution before and after 128-day UV resistance test.

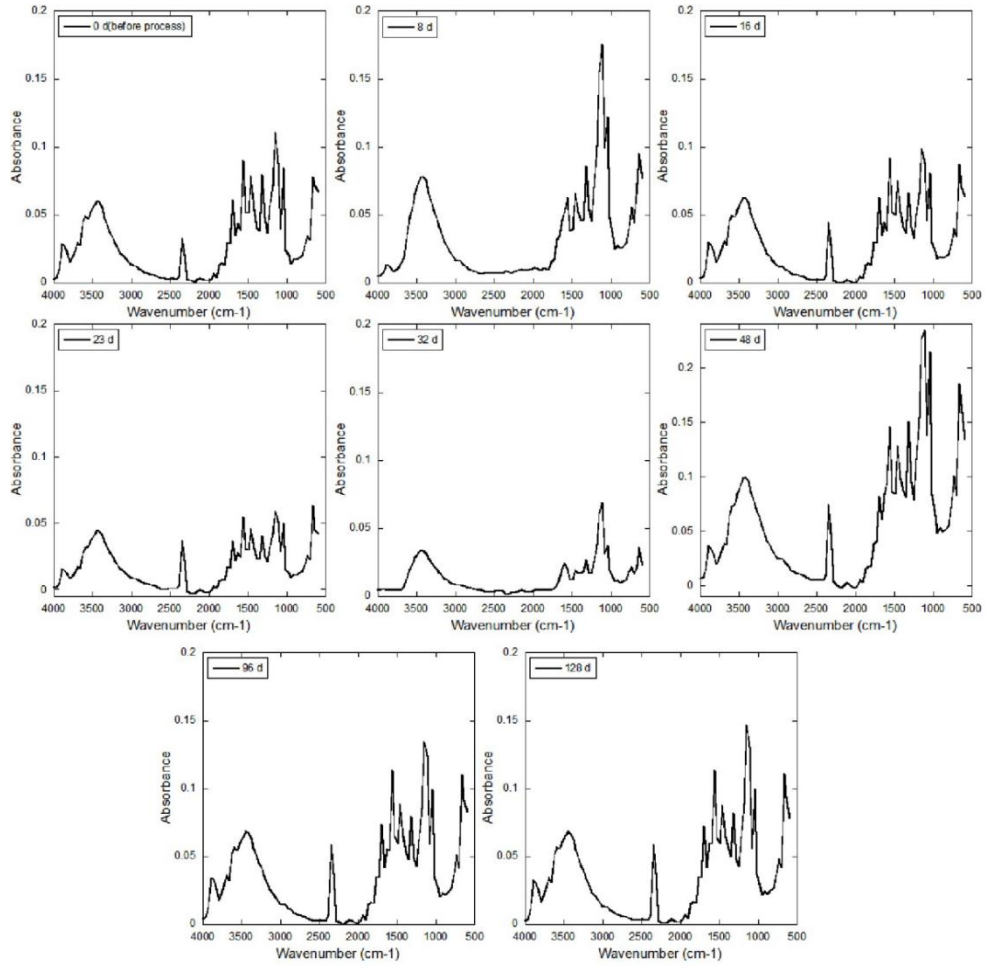

Figure 9-4. Absorbance spectra of the acid black 52 aqueous solution with different UV exposure time.

Table 5 lists the absorbance and standard deviation of each characteristic peak with respect to the corresponding UV-processing time. Equation (8) is also used here to estimate the degradation rate of the acid black 52 aqueous solution. It is assumed that the acid black 52 aqueous solution is still usable if no more than 50% of the dye molecules are degraded, and the expected service life of the acid black 52 aqueous solution under UV exposure can be estimated using Equation (9). As shown in Table 6, acid black 52 aqueous solution is expected to remain stable for more than 100 days, even after being continuously exposed to UV radiation five times the flux of the entire UV spectrum of solar radiation. In addition to the much lower UV radiation intensity posted by the solar light, two-phase thermosyphon solar collectors are also expected

to work with much less daily exposure time due to the day-night cycle on earth. Therefore, a much longer service life in loop thermosyphon can be expected for the acid black 52 aqueous solution from the UV resistance test.

Table 5. Absorbance of characteristic peaks and standard deviation.

	Absorbance			
	3450 cm^{-1}	1550 cm^{-1}	1420 cm^{-1}	1200 cm^{-1}
0 d(Before process)	0.05909	0.05570	0.05349	0.07139
8 d	0.07755	0.05139	0.05414	0.09945
16 d	0.06150	0.05391	0.05188	0.06680
23 d	0.04360	0.03315	0.03162	0.04285
32 d	0.05719	0.03796	0.03965	0.07218
48 d	0.07562	0.08270	0.07826	0.10866
96 d	0.06701	0.07030	0.06453	0.08332
128 d	0.06685	0.07036	0.06423	0.08417
Averaged Peak Value	0.06355	0.05694	0.05473	0.07860
Standard Deviation	0.01087	0.01686	0.01469	0.02036

Table 6. Estimated service life of acid black 52 aqueous solution under enhanced UV radiation

Wave Number	3450 cm^{-1}	1550 cm^{-1}	1420 cm^{-1}	1200 cm^{-1}
Degradation Rate (R)	0.26983%	0.68131%	0.58192%	0.49371%
Expected Service Life (days)	256	102	119	140

9.4 Summary

In this chapter, reliability prediction of acid black 52 aqueous solution was conducted using the FT-IR absorbance spectra. It was found that the acid black 52 aqueous solution was expected to continuously work for more than 400 days inside a two-phase thermosyphon. More than 100 days were required for the acid black 52 aqueous solution to lose half of its main components. Notably, enhanced UV tests post five times the flux of the entire UV spectrum of solar radiation. Finally, the

expected service life of the acid black 52 aqueous solution under solar light could be much longer than 100 days.

Charpter 10. Conclusion

10.1 Conclusions of Experimental and Analytical Work

This dissertation provides comprehensive information for the design, modification, characterization, and application of solar absorbing fluids. Short-term boiling and condensation tests, long-term two-phase thermosynthetic tests, and enhanced radiation tests were developed to evaluate the performance of solar absorption fluids. Multiple types of fluids were evaluated, and the conclusions are summarized below:

1. The solar absorbing fluids based on GO nanofluids were modified and tested under various working conditions, and it was found that GO nanofluids worked well with low-temperature solar applications (e.g., solar steam generation). When the working temperature of the solar apparatus rose above the boiling point, thermal reduction and severe aggregation of GO nanoparticles were then observed. Multiple strategies to mitigate the aggregation issue of GO nanoparticles have been developed and explored, and it was found that traditional methods such as pH control, addition of surfactant, and addition of CNF worked well only below the boiling point.
2. Multiple types of fluids, including rhodamine B, thermal-treated CNF, and pigmented black ink, were prepared and tested under boiling and condensation processes. The rhodamine B aqueous solution showed excellent stability with weak solar absorption capacity. Pigmented black ink was found to slowly "fade" as the processing time increased. The CNF aqueous solution was modified by thermal treatment at 180°C, and it was found that thermally treated CNF retained good solubility in water with significantly enhanced

solar absorption capacity. Thermal treatment temperature and time had much influence on the optical property and solubility of CNF. Thermal treated CNF has potential to serve as volumetric absorbing fluids, and further systematic research is needed before drawing conclusions.

3. The aqueous dye solution drew much of our attention, due to the fluid stability exhibited by rhodamine B and pigmented black ink. After reviewing the degradation mechanisms of multiple dyes, seven types of dye samples were prepared and tested under boiling and condensation processes. Mixture sample 1 showed excellent stability with weak light absorption capacity. Mixture sample 2 showed superb light absorption capacity, while fluid stability was not clear. Acid black 52 aqueous solution showed both excellent stability and superb solar absorption capacity.

4. A two-phase thermosyphon prototype was assembled to further evaluate the performance of mixture sample 2 and the acid black 52 aqueous solution. It was found that only the acid black 52 aqueous solution retained both its original stability and solar absorption capacity during long-term operation. Further degradation investigation with enhanced UV radiation confirmed that the acid black 52 dye molecule was robust against possible degradation caused by UV radiation. Reliability prediction based on the FT-IR absorbance spectra indicated that the acid black 52 aqueous solution could serve for more than 100 days without notable deterioration.

10.2 Academic Contributions

The present work provides systematic study methods on both two ends: the design and modification of solar absorbing fluids, and performance evaluation of

solar absorbing fluids with regarding to different solar apparatus and working conditions. It was found that the performance of solar absorbing fluids were mainly limited by optical properties and stability.

1. Water-based fluid stability was mainly determined by the hydrophilicity of dissolved molecules. And stability could be enchained by multiple methods such as surface modification, pH control and addition of surfactant. By using methods mentioned above, metal oxide nanofluids such as MgO, ZnO, Al_2O_3, TiO_2 and GO nanofluids were reported to remain stable serving as working fluid inside low-temperature solar collectors. However, our research found that methods mentioned above to retain fluid stability were way less effective when the working temperature rose above the boiling point of water. Both metal oxide nanofluids and GO nanofluids encountered severe aggregation issue when fluids went through boiling and condensation processes. It was speculated that the disruption of electric double layer formed around the surface of nanoparticles caused by the boiling and condensation processes should be the main reason for stability deterioration. Metal oxides and GO nanofluids performed better inside low temperature solar applications such as solar steam generation and FPSC.

2. Fluid stability was mostly monitored and reported by other researchers during the operation of solar collectors, and performance evaluation was then limited up to a few days. Few papers discussed the performance of solar absorbing fluids during long-term processes. Our research evaluated the performance of fluids during boiling and condensation processes first within the lab, and the test lasted up to 3 weeks. Fluids showed excellent stability and optical properties were then further tested and evaluated inside two-phase

thermosyphon prototype up to 200 days. Considering possible degradation caused by long-term exposure to solar radiation, enhanced radiation test was also performed in our research. By tracing the change of optical properties of fluids, a quantitative method used to calculate degradation rate and estimate service life of fluids was provided in our research. During our research, acid black 52 aqueous solution was proved to be a good choice to serve as volumetric absorbing fluid inside two-phase thermosyphon.

10.3 Journal Papers

1.Zhou, J., Yang, B., Van Velson, N., Charles, J., & Wang, J. (2023). Stability Study of Graphene Oxide Based Nanofluids for Solar Absorption Application. High temperature, 61(4), 530-535.

2.Zheng, C., Shen, Z., Zhou, J., Pei, Y., & Yang, B. (2022). Influence of The Anions on The Interaction Energy Between Water and Ionic Liquids. Chemical Engineering & Technology, 45(2), 266-274.

3.Zheng, C., Zhou, J., Pei, Y., & Yang, B. (2020). Equilibrium Thermodynamic Properties of Aqueous Solutions of Ionic Liquid 1-Ethyl-3-Methylimidazolium Methanesulfonate [EMIM][$MeSO_3$]. Scientific Reports, 10(1), 3174.

4.Jian Zhou, Ziyang Shen, and Bao Yang, Nathan Van Velson, Josh Charles, and Jianjian Wang, “Volumetric Solar Absorbing Fluids and Their Application in Two-Phase Loop Thermosyphon”, in Sustainable Energy, Power and propulsion, edited by A. De and A. Gupta, 2004, in review.

5.Pei, Y., Shen, Z., Zhou, J.& Yang, B. Experimental and Theoretical Thermal Performance Analysis of Additively Manufactured Polymer Vacuum Insulation Panels. In review.

10.4 Limitation and Future works.

The work presented in this paper is based on the application of volumetric absorbing fluids in two-phase thermosyphons. Although the use of acid black 52 aqueous solution in two-phase thermosyphons has a brilliant future, the optimum working conditions still remains unclear. Thermal-treated CNF also showed potential to work as volumetric absorbing fluids, while further chemical modification are still needed due to relative low solar absorptivity it presented in this work so far. There are several clues indicating that the degradation mechanism of GO, while more research are still needed before drawing further conclusions. Future work can be expanded towards both application and mechanism:

1. Electric resistance heating instead of solar heating was used in this work for the operation of two-phase thermosyphon. The optimum working conditions and apparatus parameters still remain unknown. It is meaningful to combine the solar concentrating parts such as parabolic trough systems with the two-phase thermosyphon, and conduct experiment with acid black 52 aqueous solution directly under solar light.
2. Although acid black 52 aqueous solution is not corrosive towards borosilicate glass. As a novel working fluid in two-phase thermosyphon, long-term corrosion test over other solar collector parts such as metal joints and o-ring are still needed.

3. Thermal-treated CNF showed excellent stability and adjustable solar absorptivity, and both heating temperature and time have great influence on the final product of thermal-treated CNF. Although the solar absorptivity presented in this work is still relative low, more researches can be conducted towards enhancing the solar abosrptivity of thermal-treated CNF.

4. GO nanofluids was found to work well in low-temperature solar apparatus without deterioration. Although de-carboxylation and de-hydroxylation reactions are proved in this work to be the main reasons of GO degradation during boiling and condensation process, and degradation reaction could possibly be triggered by bubble cavitation during such process. Further researches are still needed before revealing the whole degradation processes.

Appendices

Uncertainty analysis

The uncertainties in this work are mainly caused by systematic uncertainties and random uncertainties. Systematic uncertainties arise from uncertainties related to the measurement apparatus. In this work, the deviation of transmittance measurement with UV-Vis spectrometer (Perkin-Elmer Lambda 25) is ±0.01%. Random uncertainties are more complicated and are usually caused by multiple reasons. By repeating most of properties measurement in this work, it is found that random uncertainty of transmittance measurement is up to 0.8%. It can be seen that random uncertainties are much lager than systematic uncertainties in this work. As shown in Table 7. Uncertainty of transmittance measurement for different samples ranged from 1.63% to 7.43%. It is also worth mentioning that mixture sample 2 showed more than 35% transmittance change during both the 9-days boilng and condensation test and 32-days loop thermosyphon test. The large transmittance change is highly like caused by the unstable nature of fluid itself rather than measurement uncertainty.

Table 7. Uncertainty of transmittance measurement for different samples

Sample	Uncertainty of transmittance measurement
GO	2.47%
Rhodamine B	2.19%
Pigment black ink	2.57%
Thermally treated CNF	1.63%
Mixture sample 1	1.81%
Mixture sample 2	7.43%
Acid black 52	3.51%

Bibliography

[1]. Steve Sorrell, Jamie Speirs, Roger Bentley, Adam Brandt, Richard Miller, Global oil depletion: A review of the evidence, Energy Policy, Volume 38, Issue 9, 2010, Pages 5290-5295, ISSN 0301-4215,

[2]. Boden, T. A., Marland, G., & Andres, R. J. (1999). Global, regional, and national fossil-fuel co2 emissions (1751-2014)(v. 2017) (No. osti: 1389331; doi: 10.3334/CDIAC/00001_V2017; cdiac: doi 10.3334/CDIAC/00001_V2017). Environmental System Science Data Infrastructure for a Virtual Ecosystem (ESS-DIVE)(United States).

[3]. Colombo, U. (1992). DEVELOPMENT AND THE GLOBAL ENVIRONMENT. The energy-environment connection, 1.

[4]. Dincer, I. (1999). Environmental impacts of energy. Energy policy, 27(14), 845-854.

[5]. Ibrahim, A., Othman, M. Y., Ruslan, M. H., Mat, S., & Sopian, K. (2011). Recent advances in flat plate photovoltaic/thermal (PV/T) solar collectors. Renewable and sustainable energy reviews, 15(1), 352-365.

[6]. Ahmed, S. F., Khalid, M., Rashmi, W., Chan, A., & Shahbaz, K. (2017). Recent progress in solar thermal energy storage using nanomaterials. Renewable and Sustainable Energy Reviews, 67, 450-460.

[7]. Do Ango, A. M., Médale, M., & Abid, C. (2013). Optimization of the design of a polymer flat plate solar collector. Solar Energy, 87, 64-75.

[8]. Jeon, J., Park, S., & Lee, B. J. (2016). Analysis on the performance of a flat-plate volumetric solar collector using blended plasmonic nanofluid. Solar Energy, 132, 247-256.

[9]. Lenert, A., & Wang, E. N. (2012). Optimization of nanofluid volumetric receivers for solar thermal energy conversion. Solar Energy, 86(1), 253-265.

[10]. Khullar, V., Bhalla, V., & Tyagi, H. (2018). Potential heat transfer fluids (nanofluids) for direct volumetric absorption-based solar thermal systems. Journal of Thermal Science and Engineering Applications, 10(1).Otanicar, T. P., Phelan, P. E., & Golden, J. S. (2009). Optical properties of liquids for direct absorption solar thermal energy systems. Solar Energy, 83(7), 969-977.

[11]. Khullar, V., Tyagi, H., Hordy, N., Otanicar, T. P., Hewakuruppu, Y., Modi, P., & Taylor, R. A. (2014). Harvesting solar thermal energy through nanofluid-based volumetric absorption systems. International Journal of Heat and Mass Transfer, 77, 377-384.

[12]. Otanicar, T. P., Phelan, P. E., Prasher, R. S., Rosengarten, G., & Taylor, R. A. (2010). Nanofluid-based direct absorption solar collector. Journal of renewable and sustainable energy, 2(3), 033102.

[13]. Kumar, A., Hassan, M. A., & Chand, P. (2020). Heat transport in nanofluid coolant car radiator with louvered fins. Powder Technology, 376, 631-642.

[14]. He, Q., Zeng, S., & Wang, S. (2015). Experimental investigation on the efficiency of flat-plate solar collectors with nanofluids. Applied Thermal Engineering, 88, 165-171.

[15]. Jiang, G., Ni, X., Yang, L., Li, W., Li, Y., & Deng, Z. (2020). Synthesis of superamphiphobic nanofluid as a multi-functional additive in oil-based drilling fluid, especially the stabilization performance on the water/oil interface. Colloids and Surfaces A: Physicochemical and Engineering Aspects, 588, 124385.

[16]. Fikri, M. A., Asri, F. F., Faizal, W. M., Adli, H. K., Mamat, R., Azmi, W. H., ... & Yusaf, T. (2020, May). TiO2-SiO2 nanofluid characterization: Towards efficient

with water/ethylene glycol mixture for solar application. In IOP Conference Series: Materials Science and Engineering (Vol. 863, No. 1, p. 012055). IOP Publishing.

[17]. Jafari, D., Franco, A., Filippeschi, S., & Di Marco, P. (2016). Two-phase closed thermosyphons: A review of studies and solar applications. Renewable and Sustainable Energy Reviews, 53, 575-593.

[18]. Di Marco, P., Filippeschi, S., Franco, A., & Jafari, D. (2014, November). Theoretical analysis of screened heat pipes for medium and high temperature solar applications. In Journal of Physics: Conference Series (Vol. 547, No. 1, p. 012010). IOP Publishing.

[19]. Zhang, H., Shao, S., Tian, C., & Zhang, K. (2018). A review on thermosyphon and its integrated system with vapor compression for free cooling of data centers. Renewable and Sustainable Energy Reviews, 81, 789-798.

[20]. M.A. Hakeem, M. Kamil, I. Arman Prediction of temperature profiles using artificial neural networks in a vertical thermosiphon re-boiler Appl Therm Eng, 28 (2008), pp. 1572-1579.

[21]. Lin, M. C., Chun, L. J., Lee, W. S., & Chen, S. L. (2003). Thermal performance of a two-phase thermosyphon energy storage system. Solar energy, 75(4), 295-306.

[22]. S. Tundee, N. Srihajong, S. Charmongkolpradit Electric power generation from solar pond using combination of thermosyphon and thermoelectric modules Energy Proc, 48 (2014), pp. 453-463.

[23]. S.L. Abreu, S. Colle An experimental study of two-phase closed thermosyphons for compact solar domestic hot-water systems Sol Energy, 76 (2004), pp. 141-145

[24]. Xu, K., Du, M., Hao, L., Mi, J., Yu, Q., & Li, S. (2020). A review of high-temperature selective absorbing coatings for solar thermal applications. Journal of Materiomics, 6(1), 167-182.

[25]. S. Esposito, A. D'Angelo, A. Antonaia, A. Castaldo, M. Ferrara, M.L. Addonizio, A. Guglielmo Optimization procedure and fabrication of highly efficient and thermally stable solar coating for receiver operating at high temperature Sol Energy Mater Sol Cells, 157 (2016), pp. 429-437

[26]. A. Al-Rjoub, L. Rebouta, P. Costa, L.G. Vieira Multi-layer solar selective absorber coatings based on W/WSiAlNx/WSiAlOyNx/SiAlOx for high temperature applications Sol Energy Mater Sol Cells, 186 (2018), pp. 300-308

[27]. A. Dan, A. Biswas, P. Sarkar, S. Kashyap, K. Chattopadhyay, H.C. Barshilia, B. Basu Enhancing spectrally selective response of W/WAlN/WAlON/Al2O3–based nanostructured multilayer absorber coating through graded optical constants Sol Energy Mater Sol Cells, 176 (2018), pp. 157-166

[28]. A. Antonaia, A. Castaldo, M.L. Addonizio, S. Esposito Stability of W-Al2O3 cermet based solar coating for receiver tube operating at high temperature Sol Energy Mater Sol Cells, 94 (2010), pp. 1604-1611

[29]. Kennedy, C. E. (2002). Review of mid-to high-temperature solar selective absorber materials (No. NREL/TP-520-31267). National Renewable Energy Lab., Golden, CO.(US).

[30]. Bermel, P., Lee, J., Joannopoulos, J. D., Celanovic, I., & Soljačić, M. (2012). Selective solar absorbers. Annual Review of Heat Transfer, 15.

[31]. Tyagi, H., Phelan, P., & Prasher, R. (2009). Predicted efficiency of a low-temperature nanofluid-based direct absorption solar collector. Journal of solar energy engineering, 131(4).

[32]. Choudhary, S., Sachdeva, A., & Kumar, P. (2021). Time-based analysis of stability and thermal efficiency of flat-plate solar collector using iron oxide nanofluid. Applied Thermal Engineering, 183, 115931.

[33]. Luo, Z., Wang, C., Wei, W., Xiao, G., & Ni, M. (2014). Performance improvement of a nanofluid solar collector based on direct absorption collection (DAC) concepts. International Journal of Heat and Mass Transfer, 75, 262-271.

[34]. Liu, X., Wang, X., Huang, J., Cheng, G., & He, Y. (2018). Volumetric solar steam generation enhanced by reduced graphene oxide nanofluid. Applied Energy, 220, 302-312.

[35]. Wen D, Lin G, Vafaei S, Zhang K (2009) Review of nanofluids for heat transfer applications. Particuology 7:141–150

[36]. Choudhary, S., Sachdeva, A., & Kumar, P. (2020). Investigation of the stability of MgO nanofluid and its effect on the thermal performance of flat-plate solar collector. Renewable Energy, 147, 1801-1814.

[37]. Kaya, H., Arslan, K., & Eltugral, N. (2018). Experimental investigation of thermal performance of an evacuated U-Tube solar collector with ZnO/Etylene glycol-pure water nanofluids. Renewable energy, 122, 329-338.

[38]. Said, Z., Saidur, R., & Rahim, N. A. (2016). Energy and exergy analysis of a flat-plate solar collector using different sizes of aluminium oxide-based nanofluid. Journal of Cleaner Production, 133, 518-530.

[39]. Said, Z., Sabiha, M. A., Saidur, R., Hepbasli, A., Rahim, N. A., Mekhilef, S., & Ward, T. A. (2015). Performance enhancement of a flat plate solar collector using titanium dioxide nanofluid and polyethylene glycol dispersant. Journal of Cleaner Production, 92, 343-353.

[40]. Yu, W., Xie, H., & Bao, D. (2009). Enhanced thermal conductivities of nanofluids containing graphene oxide nanosheets. Nanotechnology, 21(5), 055705.

[41]. Sadeghinezhad, E., Mehrali, M., Saidur, R., Mehrali, M., Latibari, S. T., Akhiani, A. R., & Metselaar, H. S. C. (2016). A comprehensive review on graphene nanofluids:

recent research, development and applications. Energy Conversion and Management, 111, 466-487.

[42]. Nanda, J., Maranville, C., Bollin, S. C., Sawall, D., Ohtani, H., Remillard, J. T., & Ginder, J. M. Thermal conductivity of single-wall carbon nanotube dispersions: role of interfacial effects. The Journal of Physical Chemistry C, 2008, 112(3), 654-658.

[43]. Vakili, M., Hosseinalipour, S. M., Delfani, S., Khosrojerdi, S., & Karami, M. (2016). Experimental investigation of graphene nanoplatelets nanofluid-based volumetric solar collector for domestic hot water systems. Solar Energy, 131, 119-130.

[44]. Li, D., Müller, M. B., Gilje, S., Kaner, R. B., & Wallace, G. G. (2008). Processable aqueous dispersions of graphene nanosheets. Nature nanotechnology, 3(2), 101-105.

[45]. Stankovich, S., Dikin, D. A., Piner, R. D., Kohlhaas, K. A., Kleinhammes, A., Jia, Y., ... & Ruoff, R. S. (2007). Synthesis of graphene-based nanosheets via chemical reduction of exfoliated graphite oxide. carbon, 45(7), 1558-1565.

[46]. McAllister, M. J., Li, J. L., Adamson, D. H., Schniepp, H. C., Abdala, A. A., Liu, J.,... & Aksay, I. A. (2007). Single-sheet functionalized graphene by oxidation and thermal expansion of graphite. Chemistry of Materials, 19(18), 4396-4404.

[47]. Stankovich, S., Piner, R. D., Chen, X., Wu, N., Nguyen, S. T., & Ruoff, R. S. (2006). Stable aqueous dispersions of graphitic nanoplatelets via the reduction of exfoliated graphite oxide in the presence of poly (sodium 4-styrenesulfonate). Journal of Materials Chemistry, 16(2), 155-158.

[48]. Niyogi, S., Bekyarova, E., Itkis, M. E., McWilliams, J. L., Hamon, M. A., & Haddon, R. C. (2006). Solution properties of graphite and graphene. Journal of the American Chemical Society, 128(24), 7720-7721.

[49]. Arshad, A., Jabbal, M., Yan, Y., & Reay, D. (2019). A review on graphene-based nanofluids: Preparation, characterization and applications. Journal of Molecular Liquids, 279, 444-484.

[50]. Missana, T., & Adell, A. (2000). On the applicability of DLVO theory to the prediction of clay colloids stability. Journal of Colloid and Interface Science, 230(1), 150-156.

[51]. Popa, I., Gillies, G., Papastavrou, G., & Borkovec, M. (2010). Attractive and repulsive electrostatic forces between positively charged latex particles in the presence of anionic linear polyelectrolytes. The Journal of Physical Chemistry B, 114(9), 3170-3177.

[52]. Randall, C., & Van Tassel, J. (2001). Electrophoretic deposition. Encyclopedia of Materials: Science and Technology, 2733-2738.

[53]. Kuznetsova, Y. V., Balyakin, I. A., Popov, I. D., Schummer, B., Sochor, B., Rempel, S. V., & Rempel, A. A. (2021). Ag2S interparticle interaction in an aqueous solution: Mechanism of steric and electrostatic stabilization. Journal of Molecular Liquids, 335, 116130.

[54]. Liu, Z., Fu, R., & Yuying, Y. (2022). Preparation and evaluation of stable nanofluids for heat transfer application. Advances in Nanofluid Heat Transfer, 25-57.

[55]. Yu, W., & Xie, H. (2012). A review on nanofluids: preparation, stability mechanisms, and applications. Journal of nanomaterials, 2012, 1-17.

[56]. Peng, X. F., Yu, X. L., & Xia, L. F. (2007). Influence factors on suspension stability of nanofluids. Journal-Zhejiang University Engineering Science, 41(4), 577.

[57]. Choudhary, R., Khurana, D., Kumar, A., & Subudhi, S. (2017). Stability analysis of Al2O3/water nanofluids. Journal of Experimental Nanoscience, 12(1), 140-151.

[58]. Askari, S., Koolivand, H., Pourkhalil, M., Lotfi, R., & Rashidi, A. (2017). Investigation of Fe3O4/Graphene nanohybrid heat transfer properties: Experimental approach. International Communications in Heat and Mass Transfer, 87, 30-39.

[59]. Leong, K. Y., Najwa, Z. A., Ku Ahmad, K. Z., & Ong, H. C. (2017). Investigation on stability and optical properties of titanium dioxide and aluminum oxide water-based nanofluids. International Journal of Thermophysics, 38, 1-15.

[60]. Menbari, A., Alemrajabi, A. A., & Ghayeb, Y. (2016). Investigation on the stability, viscosity and extinction coefficient of CuO–Al2O3/Water binary mixture nanofluid. Experimental Thermal and Fluid Science, 74, 122-129.

[61]. Qu, J., & Wu, H. (2011). Thermal performance comparison of oscillating heat pipes with SiO2/water and Al2O3/water nanofluids. International Journal of Thermal Sciences, 50(10), 1954-1962.

[62]. Chang, M. H., Liu, H. S., & Tai, C. Y. (2011). Preparation of copper oxide nanoparticles and its application in nanofluid. Powder technology, 207(1-3), 378-386.

[63]. Wen, D., & Ding, Y. (2005). Formulation of nanofluids for natural convective heat transfer applications. International Journal of Heat and Fluid Flow, 26(6), 855-864.

[64]. Mahbubul, I. M., Elcioglu, E. B., Saidur, R., & Amalina, M. A. (2017). Optimization of ultrasonication period for better dispersion and stability of TiO2–water nanofluid. Ultrasonics sonochemistry, 37, 360-367.

[65]. Petzold, G., Rojas-Reyna, R., Mende, M., & Schwarz, S. (2009). Application relevant characterization of aqueous silica nanodispersions. Journal of Dispersion Science and Technology, 30(8), 1216-1222.

[66]. Chowdhury, S., Shrivastava, S., Kakati, A., & Sangwai, J. S. (2022). Comprehensive review on the role of surfactants in the chemical enhanced oil recovery process. Industrial & Engineering Chemistry Research, 61(1), 21-64.

[67]. Kralova, I., & Sjöblom, J. (2009). Surfactants used in food industry: a review. Journal of Dispersion Science and Technology, 30(9), 1363-1383.

[68]. Priya, K. R., Suganthi, K. S., & Rajan, K. S. (2012). Transport properties of ultra-low-concentration CuO–water nanofluids containing non-spherical nanoparticles. International Journal of Heat and Mass Transfer, 55(17-18), 4734-4743.

[69]. Fadhillahanafi, N. M., Leong, K. Y., & Risby, M. S. (2013). Stability and thermal conductivity characteristics of carbon nanotube-based nanofluids. International Journal of Automotive and Mechanical Engineering, 8, 1376-1384.

[70]. Neouze, M. A., & Schubert, U. (2008). Surface modification and functionalization of metal and metal oxide nanoparticles by organic ligands. Monatshefte für Chemie-Chemical Monthly, 139, 183-195.

[71]. Khan, M. S., Abid, M., Ali, H. M., Amber, K. P., Bashir, M. A., & Javed, S. (2019). Comparative performance assessment of solar dish-assisted s-CO2 Brayton cycle using nanofluids. Applied Thermal Engineering, 148, 295-306.

[72]. Li, Y., Xie, H. Q., Yu, W., & Li, J. (2011). Investigation on heat transfer performances of nanofluids in solar collector. In Materials Science Forum (Vol. 694, pp. 33-36). Trans Tech Publications Ltd.

[73]. Umar, S., Sulaiman, F., Abdullah, N., & Mohamad, S. N. (2018, November). Investigation of the effect of pH adjustment on the stability of nanofluid. In AIP Conference Proceedings (Vol. 2031, No. 1, p. 020031). AIP Publishing LLC.

[74]. Cassagneau, T., Guérin, F., & Fendler, J. H. (2000). Preparation and characterization of ultrathin films layer-by-layer self-assembled from graphite oxide nanoplatelets and polymers. Langmuir, 16(18), 7318-7324. [15] Kotov, N. A., Dékány, I., & Fendler, J. H. (1996).

[75]. Ultrathin graphite oxide–polyelectrolyte composites prepared by self-assembly: Transition between conductive and non-conductive states. Advanced Materials, 8(8), 637-641.

[76]. Sarsam, W. S., Amiri, A., Kazi, S. N., & Badarudin, A. (2016). Stability and thermophysical properties of non-covalently functionalized graphene nanoplatelets nanofluids. Energy conversion and management, 116, 101-111.

[77]. Cham sa-ard, W., Fawcett, D., Fung, C. C., Chapman, P., Rattan, S., & Poinern, G. E. J. (2021). Synthesis, characterization, and thermo-physical properties of highly stable graphene oxide-based aqueous nanofluids for potential low-temperature direct absorption solar applications. Scientific Reports, 11(1), 1-13.

[78]. Ricci, A., Cataldi, A., Zara, S., & Gallorini, M. (2022). Graphene-oxide-enriched biomaterials: A focus on Osteo and chondroinductive properties and immunomodulation. Materials, 15(6), 2229.

[79]. Meng, Z., Li, Z., Li, Y., Zhang, C., Wang, K., Yu, W., ... & Li, W. (2022). Novel nanofluid based efficient solar vaporization systems with applications in desalination and wastewater treatment. Energy, 247, 123513.

[80]. Chen, L., Liu, J., Fang, X., & Zhang, Z. (2017). Reduced graphene oxide dispersed nanofluids with improved photo-thermal conversion performance for direct absorption solar collectors. Solar Energy Materials and Solar Cells, 163, 125-133.

[81]. Hong, Z., Pei, J., Wang, Y., Cao, B., Mao, M., Liu, H.,... & Hu, X. (2019). Characteristics of the direct absorption solar collectors based on reduced graphene

oxide nanofluids in solar steam evaporation. Energy Conversion and Management, 199, 112019.

[82]. Iqbal, A., Mahmoud, M. S., Sayed, E. T., Elsaid, K., Abdelkareem, M. A., Alawadhi, H., & Olabi, A. G. (2021). Evaluation of the nanofluid-assisted desalination through solar stills in the last decade. Journal of Environmental Management, 277, 111415.

[83]. Yongan Niu, et al., "Reduction and structural evolution of graphene oxide sheets under hydrothermal treatment" Physics Letters A, 380 (2016) 3128-3132.

[84]. Anliker, R., Butler, G. C., Clarke, E. A., Förstner, U., Funke, W., Hyslop, C., ... & Anliker, R. (1980). Organic dyes and pigments. Anthropogenic compounds, 181-215.

[85]. Gupta, V. K. (2009). Application of low-cost adsorbents for dye removal–a review. Journal of Environmental Management, 90(8), 2313-2342.

[86]. Yagub, M. T., Sen, T. K., & Ang, H. M. (2012). Equilibrium, kinetics, and thermodynamics of methylene blue adsorption by pine tree leaves. Water, Air, & Soil Pollution, 223, 5267-5282.

[87]. Franco, A., & Filippeschi, S. (2012). Closed-loop two-phase thermosyphon of small dimensions: a review of the experimental results. Microgravity Science and Technology, 24, 165-179.

[88]. Reay, D., McGlen, R., & Kew, P. (2013). Heat pipes: theory, design, and applications. Butterworth-Heinemann.

[89]. D. Pellicone, Advanced Cooling Technologies, Inc. Loop Thermosyphons: Gravity-Driven Two-Phase Cooling for the 21st Century. Aerospace & Defense Technology, 02/01/2018.

[90]. Sheremet, M. A., Pop, I., & Mahian, O. J. I. J. O. H. (2018). Natural convection in an inclined cavity with time-periodic temperature boundary conditions using nanofluids: application in solar collectors. International Journal of Heat and Mass Transfer, 116, 751-761.

[91]. Sheremet, M. A., Oztop, H. F., Pop, I., & Abu-Hamdeh, N. (2015). Analysis of entropy generation in natural convection of nanofluid inside a square cavity having hot solid block: Tiwari and Das' model. Entropy, 18(1), 9.

[92]. Sheremet, M. A., & Pop, I. (2014). Natural convection in a square porous cavity with sinusoidal temperature distributions on both side walls filled with a nanofluid: Buongiorno's mathematical model. Transport in Porous Media, 105, 411-429.

[93]. Ramezanizadeh, M., Nazari, M. A., Ahmadi, M. H., & Açıkkalp, E. (2018). Application of nanofluids in thermosyphons: a review. Journal of Molecular Liquids, 272, 395-402.

[94]. Liu, Z. H., Yang, X. F., & Guo, G. L. (2007). Effect of nanoparticles in nanofluid on thermal performance in a miniature thermosyphon. Journal of applied physics, 102(1).

[95]. Noie, S. H., Heris, S. Z., Kahani, M., & Nowee, S. M. (2009). Heat transfer enhancement using Al2O3/water nanofluid in a two-phase closed thermosyphon. International Journal of Heat and Fluid Flow, 30(4), 700-705.

[96]. Huminic, G., Huminic, A., Morjan, I., & Dumitrache, F. (2011). Experimental study of the thermal performance of thermosyphon heat pipe using iron oxide nanoparticles. International journal of heat and mass transfer, 54(1-3), 656-661.

[97]. Cao, J., Zheng, Z., Asim, M., Hu, M., Wang, Q., Su, Y.,... & Leung, M. K. (2020). A review on independent and integrated/coupled two-phase loop thermosyphons. Applied Energy, 280, 115885.

[98]. Negm, M. N. A., Abdel-Rehim, A. A., & Attia, A. A. (2016, November). Investigating the effect of Al2O3/water nanofluid on the efficiency of a thermosyphon flat-plate solar collector. In ASME International Mechanical Engineering Congress and Exposition (Vol. 50626, p. V008T10A097). American Society of Mechanical Engineers.

[99]. Chougule, S. S., Sahu, S. K., & Pise, A. T. (2014). Thermal performance of two-phase thermosyphon flat-plate solar collectors using nanofluid. Journal of solar energy engineering, 136(1), 014503.

[100]. Aksu, Z. (2005). Application of biosorption for the removal of organic pollutants: a review. Process biochemistry, 40(3-4), 997-1026.

[101]. Chakraborty, S., & Panigrahi, P. K. (2020). Stability of nanofluid: A review. Applied Thermal Engineering, 174, 115259.

[102]. Oshina, I., & Spigulis, J. (2021). Beer–Lambert law for optical tissue diagnostics: current state of the art and the main limitations. Journal of Biomedical Optics, 26(10), 100901-100901.

[103]. Ghadimi, A., Saidur, R., & Metselaar, H. S. C. (2011). A review of nanofluid stability properties and characterization in stationary conditions. International journal of heat and mass transfer, 54(17-18), 4051-4068.

[104]. Loong, T. T., & Salleh, H. (2017, August). A review on measurement techniques of apparent thermal conductivity of nanofluids. In IOP Conference Series: Materials Science and Engineering (Vol. 226, No. 1, p. 012146). IOP Publishing.

[105]. Lee, J., Lee, H., Baik, Y. J., & Koo, J. (2015). Quantitative analyses of factors affecting thermal conductivity of nanofluids using an improved transient hot-wire method apparatus. International Journal of Heat and Mass Transfer, 89, 116-123.

[106]. Czarnetzki, W., & Roetzel, W. (1995). Temperature oscillation techniques for simultaneous measurement of thermal diffusivity and conductivity. International Journal of Thermophysics, 16, 413-422.

[107]. Cahill, D. G. (1990). Thermal conductivity measurement from 30 to 750 K: the 3ω method. Review of scientific instruments, 61(2), 802-808.

[108]. Han, Z. (2008), "Nanofluids with enhanced thermal transport properties."

[109]. https://www.lightning-enterprises.com/

[110]. Zhou, J., Yang, B., Van Velson, N., Charles, J., & Wang, J. (2023). Stability Study of Graphene Oxide Based Nanofluids for Solar Absorption Application. High temperature, 61(4), 530-535.

[111]. Charles, J., Van Velson, N., Wang, J., & Hoenig, S. (2022). Modeling of a loop thermosyphon supplying solar energy to a desalination boiler. In AIP Conference Proceedings (Vol. 2445, No. 1, p. 140003). AIP Publishing LLC.

[112]. Qu, J., Shang, L., Sun, Q., Han, X., & Zhou, G. (2022). Photo-thermal characteristics of water-based graphene oxide (GO) nanofluids at reverse-irradiation conditions with different irradiation angles for high-efficiency solar thermal energy harvesting. Renewable Energy, 195, 516-527.

[113]. Singh, J., Kumar, R., Kumar, H., & Gupta, M. (2021). Preparation of GO/DW nanofluids for heat transfer applications. Materials Today: Proceedings, 45, 5134-5138.

[114]. J. Liu, Z. Ye, L. Zhang, X. Fang, Z. Zhang. A combined numerical and experimental study on graphene/ionic liquid nanofluid based direct absorption solar collector. Sol. Energy Mater. Sol. Cells, 136 (2015), pp. 177-186

[115]. M. Vakili, S.M. Hosseinalipour, S. Delfani, S. Khosrojerdi. Photothermal properties of graphene nanoplatelets nanofluid for low-temperature direct absorption solar collectors. Sol. Energy Mater. Sol. Cells, 152 (2016), pp. 187-191

[116]. L. Chen, C. Xu, J. Liu, X. Fang, Z. Zhang Optical absorption property and photothermal conversion performance of graphene oxide/water nanofluids with excellent dispersion stability Sol. Energy, 148 (2017), pp. 17-24

[117]. S. Khosrojerdi, A.M. Lavasani, M. Vakili Experimental study of photothermal specifications and stability of graphene oxide nanoplatelets nanofluid as working fluid for low-temperature Direct Absorption Solar Collectors (DASCs) Sol. Energy Mater. Sol. Cells, 164 (2017), pp. 32-39

[118]. X. Xu, C. Xu, J. Liu, X. Fang, Z. Zhang A direct absorption solar collector based on a water-ethylene glycol based nanofluid with anti-freeze property and excellent dispersion stability Renew. Energy, 133 (2019), pp. 760-769

[119]. G. Gao, T. Zhang, S. Jiao, C. Guo Preparation of reduced graphene oxide-modified magnetic phase change microcapsules and their application in direct absorption solar collector Sol. Energy Mater. Sol. Cells, 216 (2020), Article 110695

[120]. Z. Li, H. Lei, A. Kan, H. Xie, W. Yu Photothermal applications based on graphene and its derivatives: a state-of-the-art review Energy, 216 (2021), Article 119262.

[121]. Agarwal, V., & Zetterlund, P. B. (2021). Strategies for reduction of graphene oxide–A comprehensive review. Chemical Engineering Journal, 405, 127018.

[122]. T.B. Gorji, A. Ranjbar A review on optical properties and application of nanofluids in direct absorption solar collectors (DASCs) Renew. Sustain. Energy Rev., 72 (2017), pp. 10-32

[123]. Liang, H., Liao, Q., Chen, N., Liang, Y., Lv, G., Zhang, P.,... & Qu, L. (2019). Thermal efficiency of solar steam generation approaching 100% through capillary water transport. Angewandte Chemie International Edition, 58(52), 19041-19046.

[124]. Shan, X., Lin, Y., Zhao, A., Di, Y., Hu, Y., Guo, Y., & Gan, Z. (2019). Porous reduced graphene oxide/nickel foam for highly efficient solar steam generation. Nanotechnology, 30(42), 425403.

[125]. Wang, G., Fu, Y., Guo, A., Mei, T., Wang, J., Li, J., & Wang, X. (2017). Reduced graphene oxide–polyurethane nanocomposite foam as a reusable photoreceiver for efficient solar steam generation. Chemistry of Materials, 29(13), 5629-5635.

[126]. Cheng, G., Wang, X., Liu, X., He, Y., & Balakin, B. V. (2019). Enhanced interfacial solar steam generation with composite reduced graphene oxide membrane. Solar Energy, 194, 415-430.

[127]. Fu, Y., Mei, T., Wang, G., Guo, A., Dai, G., Wang, S.,... & Wang, X. (2017). Investigation on enhancing effects of Au nanoparticles on solar steam generation in graphene oxide nanofluids. Applied Thermal Engineering, 114, 961-968.

[128]. Ghafurian, M. M., Niazmand, H., Ebrahimnia-Bajestan, E., & Elhami Nik, H. (2019). Localized solar heating via graphene oxide nanofluid for direct steam generation. Journal of Thermal Analysis and Calorimetry, 135, 1443-1449.

[129]. Hong, Z., Pei, J., Wang, Y., Cao, B., Mao, M., Liu, H.,... & Hu, X. (2019). Characteristics of the direct absorption solar collectors based on reduced graphene oxide nanofluids in solar steam evaporation. Energy Conversion and Management, 199, 112019.

[130]. H.C. Schniepp, J.-L. Li, M.J. McAllister, H. Sai, M. Herrera-Alonso, D.H. Adamson, et al. Functionalized single graphene sheets derived from splitting graphite oxide J Phys Chem B, 110 (17) (2006), pp. 8535-8539

[131]. H.A. Becerril, J. Mao, Z. Liu, R.M. Stoltenberg, Z. Bao, Y. Chen Evaluation of solution-processed reduced graphene oxide films as transparent conductors ACS Nano, 2 (3) (2008), pp. 463-470

[132]. C. Mattevi, G. Eda, S. Agnoli, S. Miller, K.A. Mkhoyan, O. Celik, et al. Evolution of electrical, chemical, and structural properties of transparent and conducting chemically derived graphene thin films Adv Funct Mater, 19 (16) (2009), pp. 2577-2583

[133]. X. Wang, L. Zhi, K. Mullen Transparent, conductive graphene electrodes for dye-sensitized solar cells Nano Lett, 8 (1) (2008), pp. 323-327

[134]. D. Pan, J. Zhang, Z. Li, M. Wu Hydrothermal route for cutting graphene sheets into blue-luminescent graphene quantum dots Adv Mater, 22 (6) (2010), pp. 734-738

[135]. Pei, S., & Cheng, H. M. (2012). The reduction of graphene oxide. Carbon, 50(9), 3210-3228.

[136]. S. Park, J. An, J.R. Potts, A. Velamakanni, S. Murali, R.S. Ruoff Hydrazine-reduction of graphite- and graphene oxide Carbon N. Y., 49 (2011), pp. 3019-3023,

[137]. Ren, P. G., Yan, D. X., Ji, X., Chen, T., & Li, Z. M. (2010). Temperature dependence of graphene oxide reduced by hydrazine hydrate. Nanotechnology, 22(5), 055705.

[138]. Q. He, H.G. Sudibya, Z. Yin, S. Wu, H. Li, F. Boey, et al. Centimeter-long and large-scale micropatterns of reduced graphene oxide films: fabrication and sensing applications ACS Nano, 4 (6) (2010), pp. 3201-3208

[139]. H. Shin, K.K. Kim, A. Benayad, S. Yoon, H.K. Park, I. Jung, M.H. Jin, H. Jeong, J.M. Kim, J. Choi, Y.H. Lee Efficient reduction of graphite oxide by sodium borohydride and its effect on electrical conductance Adv. Funct. Mater., 19 (2009), pp. 1987-1992,

[140]. M.R. Muda, M.M. Ramli, S.S.M. Isa, M.F. Jamlos, S.A.Z. Murad, Z. Norhanisah, M.M. Isa, S.R. Kasjoo, N. Ahmad, N.I.M. Nor, N. Khalid Fundamental study of reduction graphene oxide by sodium borohydride for gas sensor application AIP Conf. Proc., American Institute of Physics Inc. (2017), Article 020034.

[141]. Moon, I. K., Lee, J., Ruoff, R. S., & Lee, H. (2010). Reduced graphene oxide by chemical graphitization. Nature Communications, 1(1), 73.

[142]. Chen, Y., Zhang, X., Zhang, D., Yu, P., & Ma, Y. (2011). High performance supercapacitors based on reduced graphene oxide in aqueous and ionic liquid electrolytes. Carbon, 49(2), 573-580.

[143]. L. Guardia, S. Villar-Rodil, J.I. Paredes, R. Rozada, A. Martínez-Alonso, J.M.D. Tascón UV light exposure of aqueous graphene oxide suspensions to promote their direct reduction, formation of graphene-metal nanoparticle hybrids and dye degradation Carbon N. Y., 50 (2012), pp. 1014-1024.

[144]. T. Wu, S. Liu, H. Li, L. Wang, X. Sun Production of reduced graphene oxide by UV irradiation J. Nanosci. Nanotechnol., 11 (2011), pp. 10078-10081,

[145]. R.Y.N. Gengler, D.S. Badali, D. Zhang, K. Dimos, K. Spyrou, D. Gournis, R.J.D. Miller Revealing the ultrafast process behind the photoreduction of graphene oxide Nat. Commun., 4 (2013), pp. 1-5.

[146]. R. Flyunt, W. Knolle, A. Kahnt, C.E. Halbig, A. Lotnyk, T. Häupl, A. Prager, S. Eigler, B. Abel High quality reduced graphene oxide flakes by fast kinetically

controlled and clean indirect UV-induced radical reduction Nanoscale, 8 (2016), pp. 7572-7579.

[147]. Lerf, A., He, H., Forster, M., & Klinowski, J. (1998). Structure of graphite oxide revisited. The Journal of Physical Chemistry B, 102(23), 4477-4482.

[148]. Gao, X., Jang, J., & Nagase, S. (2010). Hydrazine and thermal reduction of graphene oxide: reaction mechanisms, product structures, and reaction design. The Journal of Physical Chemistry C, 114(2), 832-842.

[149]. Escobar, L. A., & Meeker, W. Q. (2006). A review of accelerated test models. Statistical science, 552-577.

[150]. Boyd, C. C., Cheacharoen, R., Leijtens, T., & McGehee, M. D. (2018). Understanding degradation mechanisms and improving stability of perovskite photovoltaics. Chemical reviews, 119(5), 3418-3451.

[151]. Fitzpatrick, S., McCabe, J. F., Petts, C. R., & Booth, S. W. (2002). Effect of moisture on polyvinylpyrrolidone in accelerated stability testing. International Journal of Pharmaceutics, 246(1-2), 143-151.

[152]. Chang, C. W., & Liao, Y. C. (2016). Accelerated sedimentation velocity assessment for nanowires stabilized in a non-Newtonian fluid. Langmuir, 32(51), 13620-13626.

[153]. Y. Li, J. Zhou, S. Tung, E. Schneider, and S. Xi, “A review on development of nanofluid preparation and characterization,” Powder Technology, vol. 196, no. 2, pp. 89–101, 2009.

[154]. H. Zhu, C. Zhang, Y. Tang, J. Wang, B. Ren, and Y. Yin, “Preparation and thermal conductivity of suspensions of graphite nanoparticles,” Carbon, vol. 45, no. 1, pp. 226–228, 2007.

[155]. Lamas, B., Abreu, B., Fonseca, A., Martins, N., & Oliveira, M. (2012). Assessing colloidal stability of long term MWCNT based nanofluids. Journal of colloid and interface science, 381(1), 17-23.

[156]. Sharma, B., Sharma, S. K., Gupta, S. M., & Kumar, A. (2018). Modified two-step method to prepare long-term stable CNT nanofluids for heat transfer applications. Arabian Journal for Science and Engineering, 43, 6155-6163.

[157]. Moharram, M. A., Ereiba, K. M. T., El Hotaby, W., & Bakr, A. M. (2015). Thermal degradation studies of graphene oxide polymer composite. Middle East J. Appl. Sci, 5(05), 23-30.

[158]. Pan, Q., Chung, C. C., He, N., Jones, J. L., & Gao, W. (2016). Accelerated thermal decomposition of graphene oxide films in air via in situ X-ray diffraction analysis. The Journal of Physical Chemistry C, 120(27), 14984-14990.

[159]. Ramezani Farani, M., Khadive Parsi, P., Riazi, G. H., Shafiee Ardestani, M., & Saligeh Rad, H. (2019). Extending the application of a magnetic PEG three-part drug release device on a graphene substrate for the removal of Gram-positive and Gram-negative bacteria and cancerous and pathologic cells. Drug design, development and therapy, 1581-1591.

[160]. RADZI HANIFAH, M. F., Jaafar, J., Aziz, M., Ismail, A. F., Othman, M. H. D., & Rahman, M. A. (2015). Effects of reduction time on the structural, electrical and thermal properties of synthesized reduced graphene oxide nanosheets. Bulletin of Materials Science, 38, 1569-1576.

[161]. Timochenco, L., Costa-Almeida, R., Bogas, D., Silva, F. A., Silva, J., Pereira, A., ... & Pinto, A. M. (2021). High-yield production of nano-lateral size graphene oxide by high-power ultrasonication. Materials, 14(8), 1916.

[162]. L.G. Guex, et al. “Experimental review: chemical reduction of graphene oxide (GO) to reduced graphene oxide (rGO) by aqueous chemistry” Nanoscale 9, 9562 (2017).

[163]. Ramezanizadeh, M., Nazari, M. A., Ahmadi, M. H., & Açıkkalp, E. (2018). Application of nanofluids in thermosyphons: a review. Journal of Molecular Liquids, 272, 395-402.

[164]. Kanti, P. K., Sharma, P., Sharma, K. V., & Maiya, M. P. (2023). The effect of pH on stability and thermal performance of graphene oxide and copper oxide hybrid nanofluids for heat transfer applications: Application of novel machine learning technique. Journal of Energy Chemistry, 82, 359-374.

[165]. Mahbubul, I. M. (2018). Preparation, characterization, properties, and application of nanofluid. William Andrew.

[166]. Júnior, J. A. A., & Baldo, J. B. (2014). The behavior of zeta potential of silica suspensions. New Journal of Glass and Ceramics, 4(02), 29.

[167]. Li, X. F., Zhu, D. S., Wang, X. J., Wang, N., Gao, J. W., & Li, H. (2008). Thermal conductivity enhancement dependent pH and chemical surfactant for Cu-H2O nanofluids. Thermochimica Acta, 469(1-2), 98-103.

[168]. Wang, X. J., Li, X., & Yang, S. (2009). Influence of pH and SDBS on the stability and thermal conductivity of nanofluids. Energy & Fuels, 23(5), 2684-2689.

[169]. Cacua, K., Ordoñez, F., Zapata, C., Herrera, B., Pabón, E., & Buitrago-Sierra, R. (2019). Surfactant concentration and pH effects on the zeta potential values of alumina nanofluids to inspect stability. Colloids and Surfaces A: Physicochemical and Engineering Aspects, 583, 123960.

[170]. Khairul, M. A., Shah, K., Doroodchi, E., Azizian, R., & Moghtaderi, B. (2016). Effects of surfactant on stability and thermo-physical properties of metal oxide nanofluids. International Journal of Heat and Mass Transfer, 98, 778-787.

[171]. Konkena, B., & Vasudevan, S. (2012). Understanding aqueous dispersibility of graphene oxide and reduced graphene oxide through pKa measurements. The journal of physical chemistry letters, 3(7), 867-872.

[172]. Sigma-Aldrich, http://www.sigmaaldrich.com/.

[173]. W. Hwang. Enhancement of Nanofluid Stability and Critical Heat Flux in Pool Boiling with Nanocellulose. Carbohydrate Polymers, 213, (2019) 393-402.

[174]. Zhou, Z., Li, Y., & Zhou, W. (2021, October). The Progress of Nanocellulose in Types and Preparation Methods. In Journal of Physics: Conference Series (Vol. 2021, No. 1, p. 012042). IOP Publishing.

[175]. Liljenzin, E. (2017). TEMPO oxidation of cellulose pulp.

[176]. Trache, D., Tarchoun, A. F., Derradji, M., Hamidon, T. S., Masruchin, N., Brosse, N., & Hussin, M. H. (2020). Nanocellulose: from fundamentals to advanced applications. Frontiers in Chemistry, 8, 392.

[177]. Dimic-Misic, K., Buffiere, J., Imani, M., Nieminen, K., Sixta, H., & Gane, P. (2021). Improved stabilisation of graphite nanoflake dispersions using hydrothermally-produced nanocellulose. Colloids and Surfaces A: Physicochemical and Engineering Aspects, 610, 125668.

[178]. Malho, J. M., Laaksonen, P., Walther, A., Ikkala, O., & Linder, M. B. (2012). Facile method for stiff, tough, and strong nanocomposites by direct exfoliation of multilayered graphene into native nanocellulose matrix. Biomacromolecules, 13(4), 1093-1099.

[179]. Han, D., Yan, L., Chen, W., Li, W., & Bangal, P. R. (2011). Cellulose/graphite oxide composite films with improved mechanical properties over a wide range of temperature. Carbohydrate Polymers, 83(2), 966-972.

[180]. Nie, J.; Liu, D.; Li, S.; Qiu, Z.; Ma, N.; Sui, G. Improved dispersion of the graphene and corrosion resistance of waterborne epoxy–graphene composites by minor cellulose nanowhiskers. J. Appl. Polym. Sci. 2019, 136, 47631.

[181]. Su, W. H., Slaughter, D. C., & Fennimore, S. A. (2020). Non-destructive evaluation of photostability of crop signaling compounds and dose effects on celery vigor for precision plant identification using computer vision. Computers and electronics in agriculture, 168, 105155.

[182]. Hariprasad, N., Anju, S. G., & Yesodharan, E. P. (2013). Sunlight-induced removal of Rhodamine B from water through semiconductor photocatalysis: effects of adsorption, reaction conditions and additives. Res. J. Mater. Sci., 2320, 6055.

[183]. Lichtenstein, K., & Lavoine, N. (2017). Toward a deeper understanding of the thermal degradation mechanism of nanocellulose. Polymer degradation and stability, 146, 53-60.

[184]. Niskanen, I., Zhang, K., Karzarjeddi, M., Liimatainen, H., Shibata, S., Hagen, N., ... & Otani, Y. (2022). Optical Properties of Cellulose Nanofibre Films at High Temperatures. Journal of Polymer Research, 29(5), 187.

[185]. Wang, H., Yang, W., Cheng, L., Guan, C., & Yan, H. (2018). Chinese ink: High performance nanofluids for solar energy. Solar Energy Materials and Solar Cells, 176, 374-380.

[186]. Zuo, X., Yang, W., Shi, M., Yan, H., Guan, C., Wu, S.,... & Li, Z. (2021). Experimental investigation on photothermal conversion properties of lampblack ink nanofluids. Solar Energy, 218, 1-10.

[187]. Zhu, W., Zuo, X., Ding, Y., Yan, H., An, Y., & Yang, W. (2023). Experimental investigation on the photothermal conversion performance of cuttlefish ink nanofluids for direct absorption solar collectors. Applied Thermal Engineering, 221, 119835.

[188]. A. Houas, H. Lachheb, M. Ksibi, E. Elaloui, C. Guillard and J.-M. Herrmann, Applied Catalysis B: Environmental, 2001, 31, 145-157

[189]. H. Zollinger, Color chemistry: syntheses, properties, and applications of organic dyes and pigments, Wiley-Vch, 2003.

[190]. Raman, C. D., & Kanmani, S. (2016). Textile dye degradation using nano-zero-valent iron : a review. Journal of Environmental Management, 177, 341-355.

[191]. Chiu, Y. H., Chang, T. F. M., Chen, C. Y., Sone, M., & Hsu, Y. J. (2019). Mechanistic insights into photodegradation of organic dyes using heterostructure photocatalysts. Catalysts, 9(5), 430.

[192]. Ayodhya, D., & Veerabhadram, G. (2018). A review on recent advances in photodegradation of dyes using doped and heterojunction-based semiconductor metal sulfide nanostructures for environmental protection. Materials Today Energy, 9, 83-113.

[193]. Farag, H. K., Aboelenin, R. M., & Fathy, N. A. (2017). Photodegradation of methyl orange dye by ZnO loaded onto carbon xerogels composites. Asia-Pacific Journal of Chemical Engineering, 12(1), 4-12.

[194]. Siddique, M., Khan, N. & Saeed, M. (2019). Photocatalytic Activity of Bismuth Ferrite Nanoparticles Synthesized via Sol-Gel Route. Zeitschrift für Physikalische Chemie, 233(5), 595-607.

[195]. Picho-Chillan, G., Dante, R. C., Muñoz-Bisesti, F., Martin-Ramos, P., Chamorro-Posada, P., Vargas-Jentzsch, P., ... & Rutto, D. (2019). Photodegradation

of Direct Blue 1 azo dye by polymeric carbon nitride irradiated with accelerated electrons. Materials Chemistry and Physics, 237, 121878.

[196]. Wang, L., Zhai, H., Jin, G., Li, X., Dong, C., Zhang, H., ... & Sun, H. (2017). 3D porous ZnO–SnS p–n heterojunction for visible light driven photocatalysis. Physical Chemistry Chemical Physics, 19(25), 16576-16585.

[197]. Azeez, F., Al-Hetlani, E., Arafa, M., Abdelmonem, Y., Nazeer, A. A., Amin, M. O., & Madkour, M. (2018). The effect of surface charge on photocatalytic degradation of methylene blue dye using chargeable titania nanoparticles. Scientific reports, 8(1), 1-9.

[198]. Umar, A., Akhtar, M. S., Al-Hajry, A., Al-Assiri, M. S., Dar, G. N., & Islam, M. S. (2015). Enhanced photocatalytic degradation of harmful dye and phenyl hydrazine chemical sensing using ZnO nanourchins. Chemical Engineering Journal, 262, 588-596.

[199]. Porter, J. J. (1973). Study of the photodegradation of commercial dyes.

[200]. Ardejani, F. D., Badii, K. H., Limaee, N. Y., Shafaei, S. Z., & Mirhabibi, A. R. (2008). Adsorption of Direct Red 80 dye from aqueous solution onto almond shells: Effect of pH, initial concentration and shell type. Journal of hazardous materials, 151(2-3), 730-737.

[201]. El Nemr, A., Abdelwahab, O., El-Sikaily, A., & Khaled, A. (2009). Removal of direct blue-86 from aqueous solution by new activated carbon developed from orange peel. Journal of hazardous materials, 161(1), 102-110.

[202]. Taqui, S. N., Yahya, R., Hassan, A., Khanum, F., & Syed, A. A. (2019). Valorization of nutraceutical industrial coriander seed spent by the process of sustainable adsorption system of acid black 52 from aqueous solution. International Journal of Environmental Research, 13, 639-659.

[203]. https://www.ossila.com/pages/standard-solar-spectrum.

[204]. Hoon, S. R., Thomas, A. D., & Linton, P. E. (2009). The Design and Development of a Closed Chamber for the in-situ Quantification of Dryland Soil Carbon Dioxide Fluxes. Geographical research, 47(1), 71-82.

[205]. Sánchez, J. V., Segundo, C. T., Palacios, E. M., Díaz, A. G., Romero, P. G. R., & Valencia, H. M. (2017). Degradation of textile dye AB 52 in an aqueous solution by applying a plasma at atmospheric pressure. IEEE Transactions on Plasma Science, 45(3), 479-484.

[206]. Gómez, A., Torres-Arenas, A. J., Vergara-Sánchez, J., Torres, C., Reyes, P. G., Martínez, H., & Saldarriaga-Noreña, H. (2017). Physical-chemical characterization of the textile dye Azo Ab52 degradation by corona plasma. AIP Advances, 7(10).

[207]. Torres Segundo, C., Vergara Sanchez, J., Montiel Palacios, E., Reyes Romero, P. G., GOMEZ DIAZ, A. A. R. O. N., & Martinez Valencia, H. (2019). Comparative study of the degradation process of Azo textile dyes AB52 and AB210 in water using a type-Corona electric discharge.

[208]. Naraginti, S., Li, Y., Wu, Y., Zhang, C., & Upreti, A. R. (2016). Mechanistic study of visible light driven photocatalytic degradation of EDC 17α-ethinyl estradiol and azo dye Acid Black-52: phytotoxicity assessment of intermediates. RSC advances, 6(90), 87246-87257.